FUNDP
61 Rue de Bruxelles
B5000 Namur
http://www.fundp.ac.be

Wave packet dynamical simulation of scanning tunneling microscopy of carbon nanosystems

Faculté des Sciences
Département de physique

Disertation présentée par
Géza Márk
en vue de l'obtention du grade de
Docteur en Sciences

2005-2006

FACULTES UNIVERSITAIRES
NOTRE-DAME DE LA PAIX
Namur

FACULTE DES SCIENCES
Laboratoire de Physique du Solide

Wave packet dynamical simulation of scanning tunneling microscopy of carbon nanosystems

Disertation présentée par
Géza MÁRK
en vue de l'obtention du grade de
Docteur en Sciences

Composition du jury:

Prof. Ph. Lambin (Promoteur)
Dr. L. P. Biró (Co-promoteur)
Prof. Ch. Van Haesendonck
Dr. A. Mayer
Prof. P. Thiry

Janvier 2006.

Resume

Ce travail présente une analyse détaillée des effets quantiques sur l'image de nanotube obtenue par microscopie à effet tunnel (STM). La diffusion dépendant du temps de paquets d'ondes est calculée à partir d'un modèle de potentiel de jellium de la jonction entre le STM et l'échantillon, qui comprend différents arrangements de nanotubes de carbone et de points contacts. Les distributions du courant de probabilité et de densité de probabilité sont déduites de la fonction d'onde dépendant du temps. La théorie permet l'identification des composants d'origine purement géométrique responsables des distorsions caractéristiques de l'image STM des nanosystèmes de carbone.

On considère plusieurs systèmes modèles, chacun consistant d'une pointe STM simulée, d'une surface de support et d'un nanosystème de carbone. On simule l'effet de la convolution de la pointe et de l'échantillon en calculant des coupes de la topographie STM au dessus d'un nanotube. On examine aussi l'effet de possibles points contacts sur le courant tunnel avant de calculer le courant tunnel pour un assemblage de nanotubes en radeau. On compare ensuite la distribution de courant tunnel pour des tubes libres et supportés. La rétrodiffusion des ondes électroniques est étudiée en simulant un nanotube fermé aux deux bouts.

On trouve que le courant qui traverse le(s) nanotube(s) et la jonction tunnel nanotube – support dépend principalement par la jonction pointe – nanotube en vertu de sa grande résistance tunnel. Le processus d'écoulement de la charge électrique est caractérisé par deux échelles de temps: le nanotube se charge d'abord assez rapidement par le paquet d'onde injecté par la pointe avant que cette charge ne s'écoule plus lentement vers le substrat. On compare aussi les distributions de courant tunnel pour deux positions de la pointe STM au dessus d'une jonction de nanotubes en Y: soit au dessus du point à symétrie trigonale, soit position décentrée le long d'un bras. Les deux probabilités tunnel ne diffèrent que peu l'une de l'autre, étant légèrement plus importante le long d'un bras. On trouve que la pointe échantillonne encore la région de la jonction quand elle est éloignée de 1.2 nm le long d'un bras.

Summary

This work contains a detailed analysis of quantum effects which influence the scanning tunneling microscopic (STM) imaging process of carbon nanostructures. Time dependent scattering of electronic wave packets was calculated on a jellium potential model of the STM junction containing different arrangements of carbon nanotubes and point contacts. Distribution of the probability current and the probability density was derived from the time dependent wave function. The theory allowed me to identify components of pure geometrical origin responsible for characteristic distortions of the STM image of carbon nanosystems.

Several model systems were constructed, each model system consisted of a simulated tip, a support surface, and a carbon nanosystem. The tip convolution effect was simulated by calculating line cuts over a nanotube; effect of point contacts was studied on the tunnel current; tunnel current for a nanotube raft was calculated; tunnel current distribution was compared for supported and unsupported nanotubes; electron wave backscattering was studied by simulating a capped tube; tunnel current distributions were calculated for different STM tip positions above a nanotube Y-junction.

The tunnel current flowing through the STM tip – nanotube(s) - support tunnel junction is mainly determined by the tip – nanotube junction owing to its large tunnel resistance. The tunneling event through the STM model is characterized by two time scales, the nanotube is quickly "charged" with the wave packet coming from the tip then this "charge" flows into the support much slower. In case of a nanotube Y-junction two characteristic STM tip positions were studied: the tip is either above the trigonal symmetry point or is displaced along one arm. The tunneling probability at the symmetrical tip position is only slightly increased from its value over an arm but in the off-the-junction case the wave packet still samples the junction region for an 1.2 nm tip displacement.

Contents

Acknowledgements

Many people contributed to this work in some way or other. Especially I would like to thank

my advisor Prof. Philippe Lambin for his continuous support and interest in this work, for many discussions and for the granted freedom. His exceptional knowledge of both the theoretical and experimental field, his deep insight and good ideas always solved even the hardest problems. He always returned the drafts of papers with helpful comments on the next day if not on the very same day. Besides this work as an ideal scientific advisor he was always ready to help in any practical problems of "staying alive" in Namur.

I had the privilege to work with Dr. L. P. Biró for 15 years. Taking his advice to utilize my wave packet dynamical software on the field of STM investigation of carbon nanostructures was a decision I have never regretted. He always delivered to me the interesting experimental problems and working on these problems proved to be always fruitful. His strong physical intuition generally showed the way to the solution. He taught me the ins and outs of publishing and proposal writing. As a head of the Nanostructures Laboratory and later the Nanotechnology Department of MTA MFA he always successfully raised the funds for resources including computers, books, travel, etc. in spite of situations that seemed often unsolvable in the transitory period of Hungarian science during the last decade. Most of the beautiful STM images in this work were measured by him or his students.

Prof. J. Gyulai was the director of MTA MFA during the time when the majority of this work was done. He always provided the possibilities to concentrate on the scientific work for our Laboratory and a quiet and friendly working atmosphere. His continuous encouragement and personal interest in my work gave a very secure feeling.

Dr. I. Bársony, the present director of MTA MFA continues to support the research in carbon nanostructures. Many thanks for possibility to work in this field.

Dr. Zs. E. Horváth, the present head of the Nanostructures Laboratory

always encouraged my work and gave the necessary freedom. I wish to thank him for the TEM images and discussions on electron microscopy of carbon nanostructures.

Dr. E. Balázs, the former head of our Laboratory was the first person who began to work in the field of STM theory in Hungary, this was back in 1985. She introduced me to the workings of this wonderful instrument. I learned from her a lot not only about science but also about human culture and life.

It was a very important seven months in my life when I had the possibility to work in the SPM group of Prof. H.-J. Güntherodt at the University of Basel. This group worked in a close collaboration with IBM Zürich, the birthplace of STM. I had the privilege to see the best experimental instruments and to learn about these from the best researchers. To experience the Swiss way of working made a great impact on my mentality.

Thanks for Levente Tapasztó for the joint work on the analytical model of the jellium nanotubes.

The former and present members of the Nanostructures Laboratory of MTA MFA (Cs. Daróczi, Gy. Dóra, E. Horváth, K. Kertész, A. Koós, P. Nagy, Z. Osváth, L. Tapasztó, and Z. Vértesy) always provided a friendly working environment. Cs. Daróczi solved a numerous computer problems for me and was always ready to teach me about computers. Thanks for A. Koós and Z. Osváth for discussions about experimental aspects of STM and nanotubes. Some of the STM images used in this work were measured by them.

Thanks for the former and present members of the Solid State Laboratory, FUNDP Namur for the nice working atmosphere and for the many practical help in Namur.

Thanks for Prof J. B.Nagy for providing nanotube samples and for his continuous interest in my work.

For Prof. P. Thiry thank for the encouragement and help in Namur.

Thanks for my family for the loving atmosphere and the patience also in tense periods. Thank you for everything, Szilvia, Lilla-Barack, Gyöngyi, Ilona, Géza, Erika, Lajos, and all others.

The system Yoga in Daily Life of Paramhans Swami Maheshwarananda always gave me the necessary health, strength, and concentration without which this work would not have been possible for me to complete. Thanks for the encouragement and good company of Károly Kovács and all other Hungarian and international yoga friends.

List of publications in the topic of the Thesis [1]

Papers

1. **Márk, G., I.**: *Analysis of the spreading Gaussian wave packet*;
   European Journal of Physics **18**, 47(1997).

2. Biró, L., P.; Gyulai, J.; Lambin, Ph.; B.Nagy, J.; Lazarescu, S.; **Márk, G., I.**; Fonseca, A.; Surján, P., R.; Szekeres, Zs.; Thiry, P., A.; Lucas, A., A.: *Scanning tunneling microscopy (STM) imaging of carbon nanotubes*;
   Carbon **36**, 689(1998).

3. **Márk, G., I.**; Biró, L., P.; Gyulai, J.: *Simulation of STM images of 3D surfaces and comparison with experimental data: carbon nanotubes*;
   Phys. Rev. B **58**, 12645(1998).

4. Biró, L., P.; **Márk, G., I.**; Gyulai, J.; Havancsák, K.; Lipp, S.; Lehrer, Ch.; Frey, L.; Ryssel, H.: *AFM and STM investigation of carbon nanotubes produced by high energy ion irradiation of graphite*;
   Nucl. Instr. Meths. B. **147**, 142(1999).

5. Biró, L., P.; Szabó, B.; **Márk, G., I.**; Gyulai, J.; Havancsák, K.; Kürti, J.; Dunlop, A.; Frey, L.; Ryssel, H.: *Carbon nanotubes produced by high energy ($E > 100$ MeV), heavy ion irradiation of graphite*;
   Nucl. Instr. Meths. B. **148**, 1102(1999).

6. Biró, L., P.; **Márk, G., I.**; Gyulai, J.; Rozlosnik, N.; Kürti, J.; Szabó, B.: *Scanning probe method investigation of carbon nanotubes produced*

---

[1] The full publication list is available on-line. For most publications the on-line database contains hotlinks to the reprint of the publication. See:
http://www.mfa.kfki.hu/int/nano/cgi-bin/wps.cgi?
Command=search&DataBaseName=nano&Field=Authors&Pattern=M.rk

by high energy ion irradiation of graphite;
Carbon **37**, 739(1999).

7. Biró, L., P.; Gyulai, J.; **Márk, G., I.**; Daróczi, Cs., S.: *Defects caused by high-energy ion beams, as measured by scanning probe methods*;
Micron **30**, 245(1999).

8. Biró, L., P.; **Márk, G., I.**; Gyulai, J.; Thiry, P., A.: *STM and AFM investigation of carbon nanotubes*;
Materials Structure **6**, 104(1999).

9. **Márk, G., I.**; Biró, L., P.; Gyulai, J.; Thiry, P., A.; Lucas, A., A.; Lambin, Ph.: *Simulation of scanning tunneling spectroscopy of supported carbon nanotubes*;
Phys. Rev. B **62**, 2797(2000).

10. **Márk, G., I.**; Koós, A.; Osváth, Z.; Biró, L., P.; Gyulai, J.; Benito, A., M.; Maser, W.; Thiry, P., A.; Lambin, Ph.: *Calculation of the charge spreading along a carbon nanotube seen in STM*;
Diamond and Related Materials, **11**, 961(2002).

11. Lambin, Ph.; **Márk, G., I.**; Meunier, V.; Biró, L., P.: *Computation of STM images of carbon nanotubes*;
Int. J. Qunatum. Chem. **95**, 495(2003).

12. Biró, L., P.; Horváth, Z.,E.; **Márk, G., I.**; Osváth, Z.; Koós, A., A.; Benito, A., M.; Maser, W.; Lambin, Ph.: *Carbon nanotube Y junctions: growth and properties*;
Diamond and Related Materials **13**, 241(2004).

13. **Márk, G., I.**; Biró, L., P.; Lambin, Ph.: *Calculation of axial charge spreading in carbon nanotubes and nanotube Y-junctions during STM measurement*;
Phys. Rev. B **70**, 115423-1(2004).

14. Tapasztó, L.; **Márk, G., I.**; Koós, A., A.; Lambin, Ph.; Biró, L., P.: *Proximity effects in STM investigation of carbon nanotubes*;
submitted

Book Chapters

1. Biró, L., P.; **Márk, G., I.**; Balázs, E.: *STM "tip changes" - a possible tool for tip characterization*; Nanophase Materials, NATO Science Series E, 260 (Kluwer Academic Publishers,1994), p. 205.

2. Biró, L., P.; **Márk, G., I.**: *STM investigation of carbon nanotubes*; Carbon filaments and nanotubes: Common origins, differing applications, NATO Science Series E, 372 (Kluwer, Dordrecht,2001), p. 219.
3. **Márk, G., I.**; Biró, L., P.; Lambin, Ph.: *Modeling and interpretation of STM images of carbon nanosystems*; Frontiers in Molecular-Scale Science and Technology of Fullerene, Nanotube, Nanosilicon, Biopolymer (DNA, Protein) Multifunctional Nanosystems, NATO Science Series II: Mathematics, Physics and Chemistry, 57 (Kluwer, Dordrecht,2002), p. 43.

Conferences

1. **Márk, G., I.**; Pacher, P.: *The study of time dependent scattering using Fourier transform technique*; in Proceedings, ICOMM'95, International conference on mathematical methods in science and Technology, 3-6 June 1995, Vienna, edited by Kainz,W. (oral, proceedings, 1995), p. 59.
2. Nagy, P.; **Márk, G., I.**; Balázs, E.: *Determination of SPM tip shape using polystyrene latex balls*; in Microbeam and Nanobeam Analysis (Mikrochimica Acta, Suppl.13), (Springer Verlag, 1996) , p. 425.
3. **Márk, G., I.**: *"Good functions" in tunneling calculations*; in Proceedings, Adriatico Research Conference: "Tunneling and Its Implications", 30 July - 2 August 1996, ICTP Trieste, Italy, (World Scientific, Singapore, 1997), p. 443.
4. **Márk, G., I.**; Biró, L., P.; Gyulai, J.: *Computer simulation of the STM imaging of nanometric 3D objects on support: carbon nanotubes*; in Electronic Properties of Novel Materials – Progress in Molecular Nanostructures, 28 February - 3. March 1998, Kirchberg, Austria, Vol. 442, Ser. AIP Conference Proceedings, (American Institute of Physics, Woodbury, New York, 1998) , p. 164.
5. **Márk, G., I.**; Biró, L., P.; Gyulai, J.; Thiry, P., A.; Lambin, Ph.: *The use of computer simulation for the investigation of tip shape and point contact effects during the scanning tunneling microscope investigation of supported nanostructures*; in Electronic Properties of Novel Materials – Science & Technology of Molecular Nanostructures, 27 February - 6. March 1999, Kirchberg, Austria (special poster, 1999).

6. **Márk, G., I.**; Biró, L., P.; Gyulai, J.; Thiry, P., A.; Lambin, Ph.: *Wave packet dynamical simulation of scanning tunneling spectroscopy of supported nanostructures*; in Inter. Symp. on Cluster&Nanostructure Interfaces, October 25-28, 1999, Richmond, VA, USA (2000).

7. **Márk, G., I.**; Biró, L., P.; Gyulai, J.; Thiry, P., A.; Lambin, Ph.: *Computer simulation of scanning tunneling spectroscopy of supported carbon nanotube aggregates*; in Electronic Properties of Novel Materials – Molecular Nanostructures, 4-11 March 2000, Kirchberg, Austria, Vol. 544, AIP Conference Proceedings, (American Institute of Physics,Melville, New York, 2000), p. 303.

8. **Márk, G., I.**; Biró, L., P.; Koós, A.; Osváth, Z.; Gyulai, J.; Benito, A., M.; Thiry, P., A.; Lambin, Ph.: *Charge spreading effects during 3D tunneling through a supported carbon nanotube*; in Electronic Properties of Novel Materials – Molecular Nanostructures, 3-10 March 2001, Kirchberg, Austria, AIP Conference Proceedings, (American Institute of Physics, Melville, New York, 2001), p. 364.

9. **Márk, G., I.**; Biró, L., P.; Gyulai, J.; Kónya, Z.; Lambin, Ph.: *Full three-dimensional wave-packet dynamical calculations of STM images of nanotube Y-junctions*; in Electronic Properties of Novel Materials – Molecular Nanostructures, 2-9 March 2002, Kirchberg, Austria, Vol. 633, Ser. AIP Conference Proceedings, (American Institute of Physics, Melville, New York, 2002), p. 381.

10. Pacher, P.; Biró, L., P.; Lambin, Ph.; **Márk, G., I.**: *Time-dependent scattering in 3D*; in Physics Teaching in Engineering Education, 5-7 June 2002, KU Leuven, Belgium (2002, proceedings published on CD, ISBN 90-5682-359-0), oral

11. Tapasztó, L.; **Márk, G., I.**; Gyulai, J.; Lambin, Ph.; Kónya, Z.; Biró, L., P.: *Geometrical effects of wave functions of carbon nanosystems*; in Electronic Properties of Novel Materials – Molecular Nanostructures, 8 - 15. March 2003, Kirchberg, Austria, Vol. 685, Ser. AIP Conference Proceedings, (American Institute of Physics, Melville, New York, 2003), p. 439.

12. **Márk, G., I.**; Biró, L., P.; Tapasztó, L.; Mayer, A.; Lambin, Ph.: *Atomic pseudopotential model for wave packet tunneling through a carbon nanotube*; in Electronic Properties of Synthetic Nanostructures,

6-13 March 2004, Kirchberg, Austria, Vol. 723, Ser. AIP Conference Proceedings, (American Institute of Physics, Melville, New York, 2004), p. 389.

List of acronyms

1D One Dimensional

2D Two Dimensional

3D Three Dimensional

CNT Carbon Nanotube

DOS Density of States

FFT Fast Fourier Transform

HOPG Highly Oriented Pyrolytic Graphite

MWNT Multiwall Nanotube

NT Nanotube

STM Scanning Tunneling Microscope

STS Scanning Tunneling Spectroscopy

SWNT Single Wall Nanotube

WP Wave Packet

WPD Wave Packet Dynamical Method

Chapter 1

Introduction

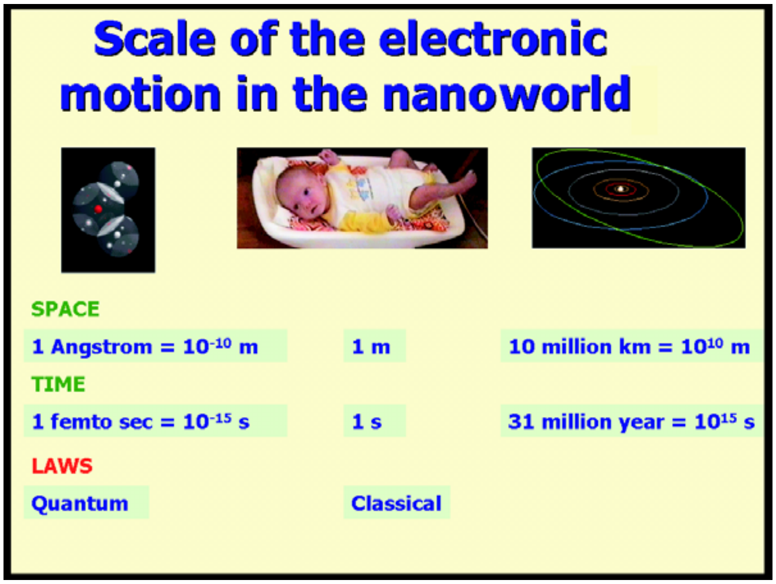

Scale of the electronic motion in the nanoworld

SPACE

1 Angstrom = 10^{-10} m	1 m	10 million km = 10^{10} m

TIME

1 femto sec = 10^{-15} s	1 s	31 million year = 10^{15} s

LAWS

Quantum	Classical

Figure 1.1: (color) Comparison of nano-, human-, and astronomical scales.

Modern science is entering into the nanoworld. The nanoworld is the world of nanostructures, a world where the characteristic length is the nanometer (10^{-9} meter). We are beginning to learn how to study the properties of individual nanostructures, how to build them, and how to assemble complicated networks from them. This rapid development is mostly driven by the need of exponentially increasing miniaturization of electronic devices [1] (`http://public.itrs.net`). If we want to understand the operation of nanoelectronic devices and to plan such devices, we need to study the motion of electrons inside nanostructures. As shown in *Fig. 1.1*, the characteristic dimensions of the electronic motion in nanostructures (10^{-10} m and 10^{-15} s are as far from the characteristic dimensions of our direct sensory experiences (1 meter and 1 second) as the astronomical world is from our human world. The most important difference and difficulty, however, is that electronic motion in the nanoworld is governed by the laws of quantum mechanics. Because of this vast distance from the human world, all measurements of the nanoscopic electron motion are indirect and generally difficult to interpret. These systems are, however, considerably more complex than atoms and simple molecules, hence it is difficult to study them theoretically. This is where computer simulation comes in as an extremely useful tool. Computers, products of today's microtechnology help to realize the nanotechnology of tomorrow.

Carbon nanotubes (CNTs) first observed more than a decade ago [2] are potential building blocks for future nanoelectronics [3] because they can be conducting or semiconducting [4]. The feasibility of CNT transistors [5, 6] and even logic gates [7] with sub-nanometer active regions has already been demonstrated. Electronic structure of a freestanding single wall carbon nanotube (SWNT) is uniquely determined by its atomic structure, these all-carbon molecules can be metallic and semiconducting according to the (n, m) wrapping indices of the graphene sheet. Simple tight-binding theory reproduces this relation remarkably correctly [8], as verified by ab-initio calculations [9], and scanning tunneling microscopy (STM), experiments [10, 11]. Close vicinity of other objects, however, alters the CNT electronic structure. The strongest change is due to the electrostatic doping effect, which is actually utilized in CNT-FETs [12]. As was pointed out, however, the contacts and the support surface may strongly influence the behavior of CNT electronic devices. Three-terminal nanoelectronic devices [13] can also be fabricated from CNT Y-junctions [14, 15]. Y-junctions are shown to have asymmetric I-V characteristics [16] and the current between two ends of the Y is influenced by the potential given to the third end [17]. It is still debated, however, whether the rectifying behavior is an intrinsic property of the junction or rather caused by electronic structure of the interface to the metallic leads [18].

STM is one of the main techniques to investigate individual carbon nanostructures [19] and devices fabricated from them. This is because of its unprecedented spatial resolution: STM is routinely able to achieve atomic resolution and the vertical resolution is better than 0.01 nm. When Binnig and Rohrer first measured [20] the exponential distance dependence in an externally and reproducibly adjustable vacuum gap then combined scanning [21] with the tunneling effect, many scientist though such an instrument should not have worked in principle. Indeed, it took several years to explain why the STM is possible [22] and what an STM instrument is measuring actually. In the simplest approximation [23] the tunneling current is proportional to the surface local density of states at the Fermi energy at the position of the STM tip.

STM is the only tool offering the possibility to study both the atomic and electronic structure of the same nanostructure with sub-nanometer resolution [24]. This unique advantage of the method is also its greatest difficulty: the influence of the geometry (i.e. the spatial positions of the atoms) and the influence of the electronic structure is always intimately mingled in STM images and scanning tunneling spectroscopy (STS) curves. Several other factors, as the STM tip geometry [25] and the properties of the support surface (the conducting substrate on which the nanostructure is deposited for STM study) also affect STM imaging. There are some characteristic differences in the STM imaging of a three dimensional object "floating" over the surface of the support as compared with STM techniques usually applied on flat, homogeneous single crystalline surfaces or adsorbate covered surfaces. First of all, in this case one cannot neglect the convolution effects arising from the geometry at the very end of the STM tip. The second important difference arises from the existence of two tunneling gaps: one between the tip and the NT and the second, between the NT and the surface over which it is floating. The differences in the electronic structure of the nanostructure and that of the support may also have a significant effect on the value of the tunneling current. A further effect which is to be taken into account in the interpretation of STM data is the value of the tunneling gap between the tip and the imaged object. Early work on the dependence of STS spectra on the width of the tunneling gap showed that the STS results are influenced by this value [26, 27]. This gap can be an important parameter in understanding the STS data and the topographic STM images of CNTs. Atomic resolution images of CNTs do not exclude the possibility of point contact imaging [26].

All these factors influencing STM imaging of carbon nanostructures show that the interpretation of experimental STM images and STS spectra is not an easy task. I address all these factors systematically in this work and analyze their specific effect on the STM/STS results.

Experimental STM/STS results analyzed in this work were mainly measured in our Laboratory, the Nanotechnology Department (headed by Dr. L. P. Biró) of MTA MFA, Budapest and in the LASMOS, FUNDP Namur (headed by Prof. P. Thiry). Most of the measurements were done by Dr. L. P. Biró and his students. Majority of the CNT samples measured were prepared at the Laboratory of Nuclear Magnetic Resonance (headed by Prof. J. B.Nagy) by the catalytic decomposition of acetylene [28] over a supported transition metal catalyst.

1.1 Outline

The organization of this thesis is as follows. Chapter 2 gives a brief introduction to STM investigation of carbon nanosystems. In Chapter 3 the theoretical framework, the models, and the algorithms are presented which I used for the simulation of the STM tunneling process. First the potential scattering model of the STM tip – NT(s) – substrate model is constructed, then I introduce the wave packet dynamical method, discuss the choice of initial states and the proper measurables. Chapter 4 gives a detailed analysis of the geometrical factors influencing the STM imaging process. This includes the effect of the tip convolution, influence of point contacts, and that of tip polarity. Chapter 5 is devoted to the study of the STM tunneling process. After the detailed examination of the time development of the tunneling process specific experimental arrangements are analyzed: a semi-infinite capped tube, a quantum dot, and a NT Y-junction.

Hartree atomic units are used in all formulas except where explicit units are given. SI units are used, however, in all the figures and numerical data.

The personal pronoun ”I” is used for my work, ”we” for the work I participated in, and ”they” for the results of others. For all published figures the reference is given as ”From” for papers where I am among the authors and as ”Ref” for other papers.

Chapter 2

STM investigation of carbon nanotubes

2.1 Carbon nanotubes

Carbon is a unique element regarding its electronic orbital versatility and its subsequent polymorphism. One of its electronic hybridizations is sp^2, which is the one that graphite is built with.

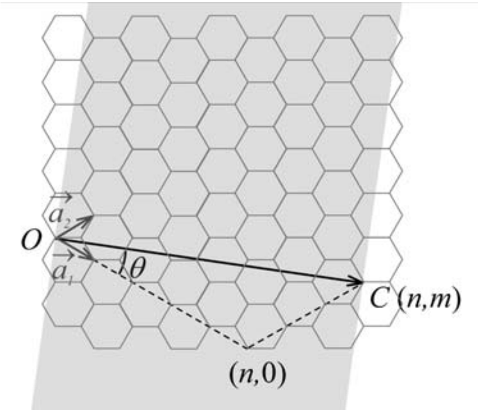

Figure 2.1: Geometrical construction of a carbon nanotube. $\vec{a}_1$ and $\vec{a}_2$ are the unit vectors of the graphene sheet, $\vec{c}$ is the wrapping vector. The shaded region shows the rectangle cut from the graphene sheet. After [29].

Single wall carbon nanotubes (SWNTs) are objects composed of carbon with typical diameters of the order of 1 - 2 nm. The structure of a SWNT is like that resulted after rolling a single sheet of graphene into a cylinder. Along the cylinder axis SWNTs are typically of μm in length. *Fig. 2.1* shows the geometrical construction of a SWNT. The two vectors $\vec{a}_1$ and $\vec{a}_2$ span the graphene unit cell, $|\vec{a}_1| = |\vec{a}_1| = \sqrt{3}a_{CC} = 0.246$ nm, where $a_{CC} = 0.142$ nm is the $C - C$ nearest neighbor distance in the graphene sheet. Graphene has two atoms in the unit cell located at the origin and at $1/3 \cdot (\vec{a}_1 + \vec{a}_2)$. To obtain a NT first a long and narrow rectangle is cut from the graphene sheet (shown in *Fig. 2.1* by shading). The direction and length of the narrower side is given by the *wrapping vector* $\vec{c} = n\vec{a}_1 + m\vec{a}_2$. This rectangle is then rolled up to a cylinder so that $\vec{c}$ becomes the circumference of the tube. The direction of the NT axis is naturally perpendicular to $\vec{c}$. Hence the diameter $d = |\vec{c}|/\pi$ of the CNT is

$$d = \frac{\sqrt{n^2 + m^2 + nm}}{\pi} \cdot \sqrt{3}a_{CC}. \tag{2.1}$$

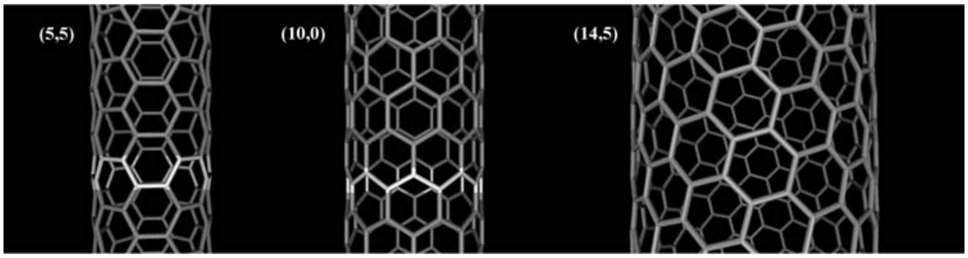

Figure 2.2: Graphene sheet wrapped up in various ways as a model of various SWNTs. An armchair, a zigzag, and a chiral tube is shown. A chain of bonds is highlited along the circumference of the armchair and the zigzag tube.

The structure of an "ideal" SWNT (i.e. an infinite seamless one) is perfectly determined by the wrapping vector $\vec{c}$ which is in turn determined by the tuple (n, m), the wrapping indices (or chiral indices). Several, typical examples are shown in *Fig. 2.2*. Because of the characteristic shape of the chain of $C-C$ bonds along the circumference of the NT (highlited in the figure) (n, n) tubes are called *armchair* tubes and $(n, 0)$ tubes are called *zigzag* tubes. General (n, m) tubes are called *chiral* tubes.

Even the structure of a seamless SWNT, however, is different from that given by the above simple geometrical construction. This is because the c_3 symmetry of the graphene sheet is broken by the rolling operation: $C-C$ bonds along the tube axis and perpendicular to the tube axis become inequivalent. For small diameter tubes *ab-initio* geometry optimization [30] indeed gives noticeable atomic displacements from the positions determined by the simple wrapping of the graphene sheet. The deviation from the ideal behavior increases with increasing curvature. The most prominent change is the increase of the diameter with respect to its geometrical value (eq. 2.1).

Although ideal CNTs consist merely of carbon atoms, their physical properties vary significantly, depending on the details of the atomic arrangement (determined by the (n, m) tuple). The most prominent example of this connection is the dependence of the SWNT electronic structure on its chirality. On the basis of their electronic structure the SWNTs can be divided into two groups [4]: *semiconducting NTs*, these have a vanishing density of states (DOS) at the Fermi energy and *metallic NTs*, with a finite DOS at Fermi energy. The *zone folding* approximation [31, 32] gives a simple unique relation between the (n, m) tuple and the electronic structure of a CNT: if $n - m = 3k$, where k is integer, then the CNT is metallic, all other tubes are semiconductors. The DOS of SWNTs contains *van Hove singularities* (where $dE/dk = 0$), which is a signature of 1D electronic structure. The energy gap ΔE_{11} [33, 34] between the first two van Hove singularities below and above E_F is:

$$\begin{aligned} \Delta E_{11}^{metallic} &= 6\frac{a_{C-C}\gamma_0}{d}, && (2.2) \\ \Delta E_{11}^{semiconductor} &= 2\frac{a_{C-C}\gamma_0}{d}, && (2.3) \end{aligned}$$

where γ_0 is the π electron interaction integral. For typical SWNTs of $d \approx 1$ nm diameter $\Delta E_{11}^{metallic} \approx 1.5$ eV and $\Delta E_{11}^{semiconductor} \approx 0.5$ eV [10]. Calculations taking the $\sigma - \pi$ interaction into account [35, 36] show the opening of a curvature induced minigap on E_F for all CNTs with $n - m = 3k \neq 0$. Hence the $n = m$ armchair CNTs are the only true metallic systems. For SWNTs the above predictions are verified by experiments [10, 11] and *ab-initio* calculations [9].

A multi wall carbon nanotube (MWNT) is built by concentrically placing the smaller diameter SWNTs in the larger diameter ones in a way that the graphene cylinders are separated by a distance of 0.34 nm [37, 38]. This value is between the 0.335 nm interlayer distance of ABAB graphite (HOPG) and the 0.344 nm interlayer distance of turbostratic graphite. This is because the ABAB stacking can not in general be realized in MWNTs and this shifts the interlayer distance towards the value characteristic of turbostratic graphite. The diameter of MWNTs may range up to 100 nm.

Another regular, multi-shell structure frequently found experimentally is the "rope" [39] or "raft" [25] of SWNTs, which is built by placing side by side the SWNTs in a way that their axes are parallel to each other with intertube spacing 0.32 nm characteristic of van der Waals inter-SWNT binding [39].

Real CNTs do contain defects in general and these defects do influence the geometry and also the properties of CNTs. Incorporation of pentagons and heptagons (5- and 7 membered rings) introduces curvature to a perfect graphene sheet. Due to this effect, different arrangements of pentagons and heptagons give a large variety of carbon nanostructures, like metal-semiconductor junctions [40], CNT knees [41], tori [42], coils [43] and Y, T, X [44, 45], etc multiterminal connections [46]. These nanostructures are potential building blocks of future nanoelectronics.

When the ratio of nonhexagonal to hexagonal rings is more than unity, the NT walls become undulated and the interlayer distance increases. These structures can be described by the *Haeckelite* model [47, 48]. We performed an extensive study of the structural and electronic properties of coiled and curled CNTs having a large number of pentagon-heptagon pairs in a co-operation between LPS, FUNDP Namur and our Laboratory [49, 50, 51, 52, 53].

Another kind of defects are the foreign atoms built into the carbon lattice, e.g. from the catalyst used for SWNT production. CNTs can also be *functionalized* chemically [54], i.e. various molecules can be bound to the CNT. Functionalization increases the bond strengh [55] between the CNTs and the matrix in NT composites.

2.1.1 CNT preparation methods and applications

The need for CNTs is steadily increasing, thanks to their extraordinary properties. Practical applications demand a large quantity of CNTs with controllable properties on a low cost. The most important CNT preparation methods existing today are as follows.

Iijima found the NTs in arc discharge prepared samples [2]. The arc is generated between two carbon rods in an inert gas (He, Ar) atmosphere. This method is similar to that used for fullerene synthesis [56]. Arc grown MWNTs are generally well graphitized (contain only a few pentagons and heptagons) and have closed ends, their inner diameter is 1 - 3 nm, outer diameter is 2 - 25 nm, the length is around 1 μm. By co-evaporation of a catalyst SWNTs can also be produced. Arc grown SWNTs are mostly arranged in hexagonal ropes.

In a variation of the arc discharge method an AC arc is generated between two carbon rods submerged in water [58, 57]. There is no product on the electrodes, the deposit peels off the electrodes. A continuous flow of water makes it easy the removal of the product from the system. This cheap and easy to use method produces well graphitized MWNTs. *Fig. 2.3* shows TEM images of MWNTs produced by the underwater arc method in our Laboratory.

Laser ablation of carbon was the first method [59] to produce fullerenes. This method was optimized for the production of SWNTs and MWNTs. The product of this costly technique contains long bundles (5 - 20 μm) of 1 - 2 nm

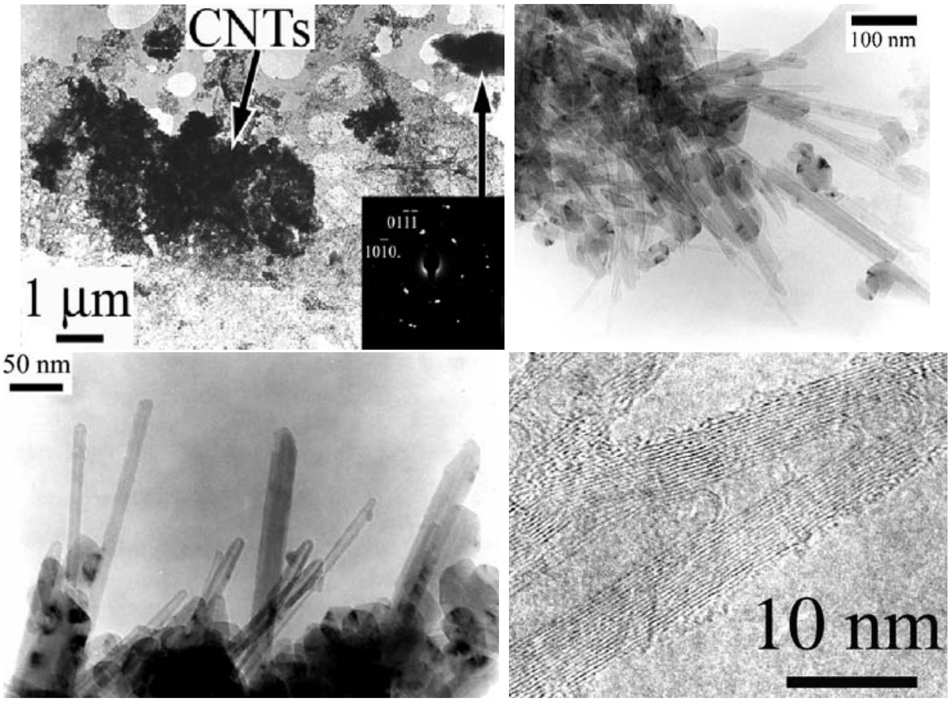

Figure 2.3: TEM images with increasing magnification of carbon nanotubes produced in an underwater electric arc. Electron diffraction is shown on one of the graphitic particles in the upper left subimage. The HRTEM image (lower right) shows MWNTs with well graphitized, straight walls and tapered ends. Ref. [57].

diameter SWNTs with good diameter distribution control.

The CCVD method [60, 28] (Catalytic Chemical Vapour Deposition) has been used since the seventies to produce carbon filaments [61]. This method is based on the catalytic decomposition of hydrocarbons. CNTs grow on the catalyst particles. SWNTs and MWNTs can also be produced. An important advantage of the CCVD method is the possibility of patterned growth by catalyst litography which is important for field emission application in flat displays. CCVD grown CNTs are generally less graphitized because of the low synthesis temperature (700° – 1000°). This method is applied at the RMN Laboratory of FUNDP since 1993. First STM images of CCVD SWNTs were published in 1997 by L. P. Biró et al [25].

A variety of the CCVD method is the spray pyrosylis [62] method. The liquid carbon source and the catalyst is sprayed into a furnace and the CNT containing product is removed in a continuous process. Diameter and morphology dependence on experimental conditions of CNT arrays grown by this method was studied in our Laboratory [63].

The method of high pressure catalytic decomposition of CO (HiPco [64] method), similarly to the spray pyrolysis is also a continuous method. SWNT material of 97% purity can be produced at rates of 450 mg/h.

All these methods produce a statistical mixture of different (n, m) SWNTs or MWNTs composed from them. The with of this statistical distribution can be decreased, but no method exists today for a controlled growth of specific (n, m) tubes. This level of control, or at least the selective growth of semiconducting and metallic CNTs would be important for nanoelectronic applications.

Most of the applications of CNTs, however, are possible without this ultimate control. Excellent field emission properties of CNTs [65, 66] makes it possible to utilize CNTs in high resolution electron microscopes, flat screens, and even in lamps.

According to the experiments [67] and calculations [68, 69] the Young's modulus of SWNTs is around 1 TPa and the CNTs return to their initial state after several cycles of large deformations. These excellent mechanical properties makes it possible to improve the composite materials by incorporating CNTs into a plastic or ceramic matrix.

The strong relation between the atomic structure and the electronic structure makes it necessary to investigate isolated CNTs, to resolve their atomic structure, and to measure the electronic structure of the very same NT. STM is able to achieve these tasks.

2.2 Scanning tunneling microscopy

In principle, the concept of an STM is very simple (see *Fig. 2.4*): an atomically sharp, metallic tip is brought within a distance of a few tenths of a nanometer to a conducting surface; due to their quantum mechanical behavior, electrons may tunnel from the tip to the surface and vice versa.

Unless a bias U_t is applied between the tip and the surface the two electron fluxes: surface - tip, and tip - surface, will be equal, and will cancel out each other in equilibrium. When an external bias is applied, depending on the polarity of the bias, one of the tunneling directions is made preferential, therefore a net electronic current can be measured in the circuit. Usually the bias is of the order of 1 V, which yields currents in the 1 nA range. *Fig. 2.5* shows the one dimensional (1D) band structure model of the tunneling mechanism from left electrode to the right one.

In practical STM instruments, the positioning and scanning of the STM

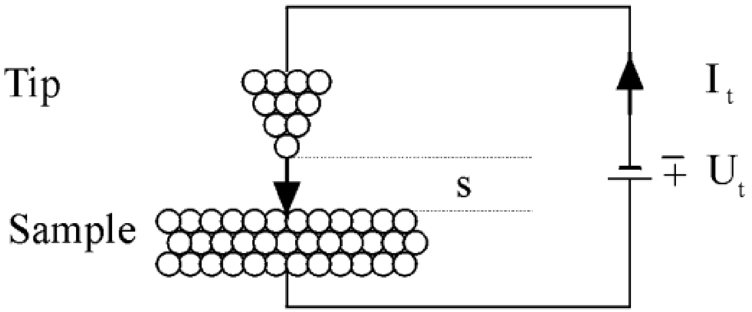

Figure 2.4: Concept of the STM. Small circles symbolize the atoms. s is the tip-sample tunnel gap. From [70].

tip is achieved by piezoelectric actuators in most cases. The width of the STM gap is controlled by a feedback loop which keeps the value of the tunneling current at a setpoint value $I_{setpoint}$ selected by the operator. An STM can operate in several operating modes, the two most important ones are as follows:

- Topographic (constant current) imaging: the feedback loop is on, the image is generated from the values of the voltage applied to the "z" piezo-actuator to maintain a constant value of the tunneling current. Provided the electronic structure at the sample surface is homogeneous, the topographic profile of the surface will be generated. Foreign atoms are seen as a dip or a hill, depending on their electronic structure.
- Current-voltage spectroscopy, frequently called scanning tunneling spectroscopy (STS). The scanning, and the feedback loop are switched off, the value of the tunneling gap is fixed, and the bias voltage is ramped from $-U$ to $+U$, and the corresponding current variations are recorded. The function dI/dV gives information about the local DOS (Density Of States) of the sample.

The explanation of the unprecedented lateral resolution of the STM lies in the exponential distance dependence of the tunneling probability: the tunnel current flows in a narrow channel between the closest point of the tip and sample.

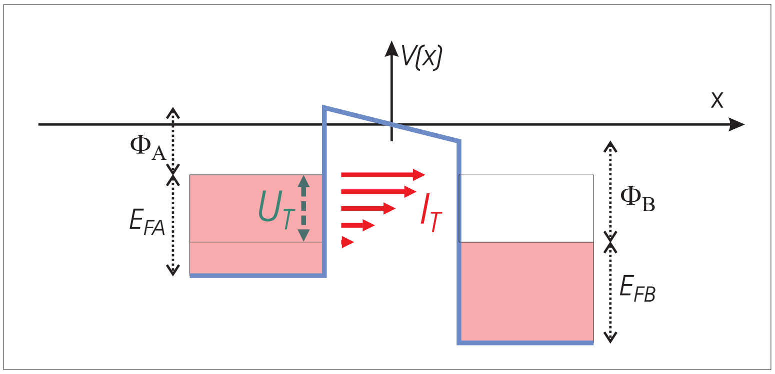

Figure 2.5: (color) Band structure model of STM tunneling. The I_t tunnel current is constituted from contributions of states in the energy window U_t. Red arrows symbolize that the contribution is increasing with increasing energy because the states with higher energy "see" a shallower potential gap.

2.3 STM investigation of carbon nanotubes

The first STM experiment proving that atomic resolution is possible on a CNT was reported in 1993 [71]. The authors of that publication investigated MWNTs produced in-situ by the condensation of evaporated carbon on a highly oriented pyrolytic graphite (HOPG) substrate.

The earliest STS measurement on CNTs was reported in 1994 [72]. These measurements were carried out in air on MWNTs grown by the electric arc method transferred onto an Au substrate by ultrasonication in ethanol. Both semiconductor and metallic CNTs were found.

There are two distinct classes of NTs on which atomic resolution was achieved: *i)* MWNTs with diameters of several tens of nanometers [71, 73] like in *Fig. 2.6* and *ii)* SWNTs with diameters in the 1 nm range [10, 11] like in *Fig. 2.7*. These images were measured by L. P. Biró [70]. While the MWNTs show a similar structure to HOPG, i.e. a threefold symmetrical lattice composed of tunneling current maxima (light features) and sometimes Moiré superstructures [71]; the SWNTs show a threefold symmetrical lattice of minima (dark features) corresponding to the empty centers of the hexagons building up the graphene sheet.

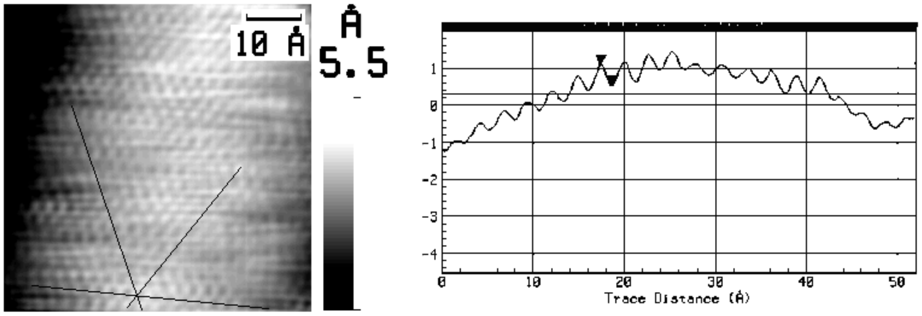

Figure 2.6: Atomic resolution, constant current, topographic image of a MWNT. $I_t = 1.0$ nA, $U_t = 100$ mV. Note the three lines oriented along the directions in which the β sites (visible in the STM images of graphite) are aligned. The line cut clearly shows the curvature of the nanotube and the atomic corrugation. Some blurring is present in the image due to the mechanical contact of the tip with the nanotube. From [74].

2.4 Perturbative theory of STM imaging

The tunneling into a supported NT is a complex problem due to the two junctions (STM tip – CNT and CNT – support) the STM current must go through. As I will show later in Section 5.6, my wave packet dynamical results clearly indicate that this process proceeds in two, quasi sequential processes. In the first process, when the electrons tunnel from the tip into the NT, the support plays little role. In the second process, the STM tip itself plays little role. One could reasonably well reproduce the first process by ignoring the support and by assuming that the NT is contacted by two electrodes at both ends through which the spreading charges can be evacuated into the external STM circuit. Compared with the floating NT, this electrical setup would certainly affect the absolute value of the transmission coefficient of the STM problem, but should have little influence on the imaging process itself. *Ab-initio* calculations of the STM image of a NT on Au using the Tersoff-Hamann formalism (see Section 2.4.1) has shown that this is actually the case [9].

Treating the tip-sample coupling as a first-order perturbation the total tip-sample current is given as

$$I_t = \frac{2\pi e}{\hbar} \int_{-\infty}^{+\infty} dE \, [f_t(E) - f_s(E)] \sum_{\alpha,\beta} |\langle \alpha | v | \beta \rangle|^2 \delta(E - E_\alpha) \delta(E - E_\beta) \ . \quad (2.4)$$

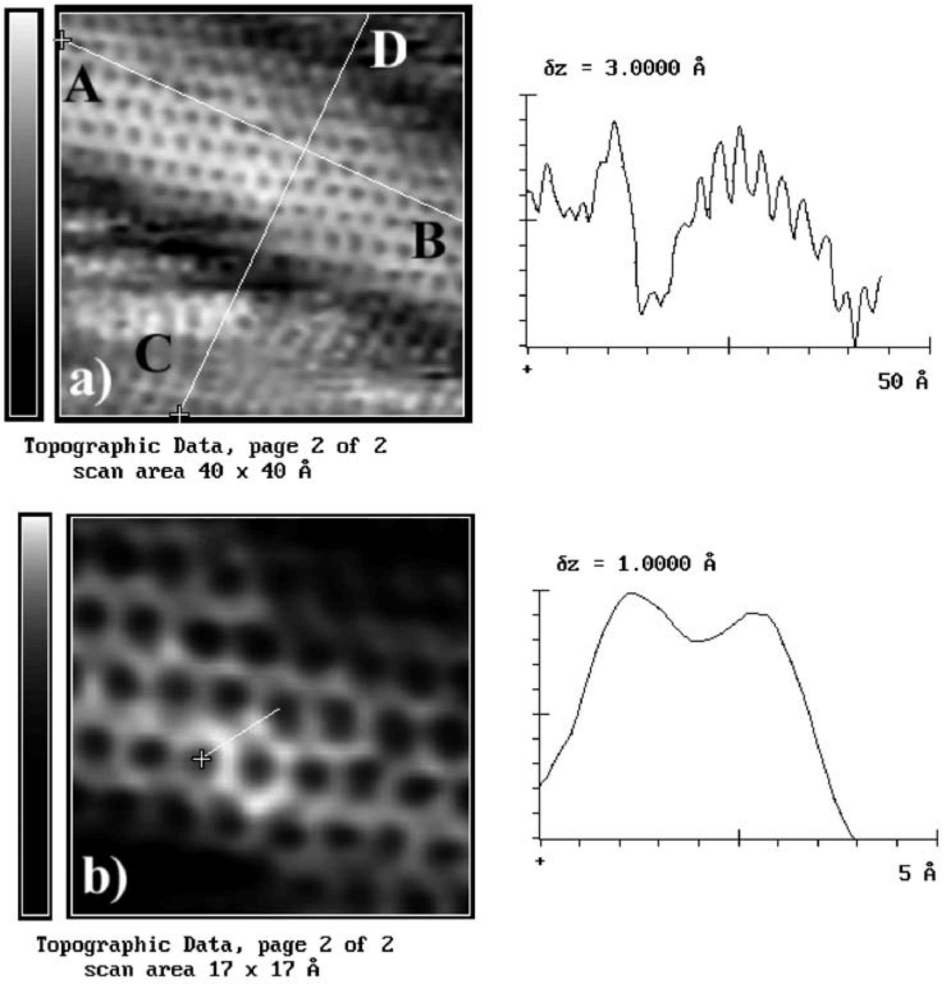

Figure 2.7: Atomic resolution topographic STM image of a SWNT. a) Gray scale at left corresponds to 0.35 nm; AB is parallel with the tube axis, the line cut along CD is shown at right hand side. b) Detail of the tube seen in a), gray scale at left correspond to 0.26 nm; as seen in the line cut (shown on right hand side of the image) taken along the marked line in b), the measured distance of the carbon atoms in the hexagon is 0.148 nm, while the amplitude of the corrugation from the empty center of the hexagon to the tunneling current maximum corresponding to the carbon atom is 0.8 nm. From [70].

where $f_t(E)$ and $f_s(E)$ are the occupation numbers of the tip and sample, respectively and $\langle\alpha|v|\beta\rangle$ is the coupling matrix element of an $|\alpha\rangle$ tip state to a $|\beta\rangle$ sample state. This equation is the well-known starting expression of the perturbative theories of elastic tunneling processes.

2.4.1 Tersoff-Hamann theory

In this simplified model [23] only one atom at the tip apex is taken into account, with an s-wave orbital. Both the tunneling matrix elements and the tip DOS are taken to be constant in the eU_t energy window. With these assumptions the tunnel current is directly proportional to the LDOS integrated between the Fermi level of the tip and sample, that is

$$I_t(\vec{r}, U_t) \propto \int_{E_F^s - eU_t}^{E_F^s} dE\ \rho_{LDOS}(\vec{r}, E)\ , \tag{2.5}$$

with

$$\rho_{LDOS}(\vec{r}, E) = \sum_{\beta} \mid \psi_\beta(\vec{r}) \mid^2 \delta(E_\beta - E)\ , \tag{2.6}$$

where ψ_β and E_β are the electron wavefunction and eigenvalue of state β, respectively. We then approximate the constant current images as iso-surfaces of $I_t(\vec{r}, U_t)$. Using this approximation Rubio et al. simulated [9] STM images of SWNTs by determining the $\rho_{LDOS}(\vec{r}, E)$ values from *ab-initio* calculations.

For an infinitesimally small bias eq. 2.5. becomes even simpler:

$$I_t(\vec{r}, U_t) \propto \rho_{LDOS}(\vec{r}, E_F^s)\ , \tag{2.7}$$

which means that the tunnel current at tip position $\vec{r}$ is simply proportional to the sample LDOS on the Fermi level at the center of the tip.

2.4.2 Tight-binding STM theory

To go beyond the simple Tersoff-Hamann result one has to make some justificated assumptions for the $\langle\alpha|v|\beta\rangle$ tunneling matrix elements and for the tip DOS. A simplest formalism to accomplish this is the *tight-binding* theory of STM imaging [75].

By treating the coupling interaction v between the STM tip and the isolated NT in first order perturbation theory, the tunnel current between them is given by eq. 2.4. In tight-binding, assuming one orbital per atom for the sake of simplicity, the electronic states of the tip and sample are linear combinations of atomic orbitals located on the corresponding sites i and j:

$$|\alpha\rangle = \sum_{i\in t} \chi_i^\alpha |\eta_i\rangle \ , \ |\beta\rangle = \sum_{j\in s} \psi_j^\beta |\theta_j\rangle \ . \tag{2.8}$$

Inserting these LCAO expressions in eq. 2.4 yields the following expression of the current at zero Kelvin [76]

$$I = (2\pi)^2 \ \frac{e}{h} \int_{E_F^s - eV}^{E_F^s} dE \sum_{i,i'\in t} \sum_{j,j'\in s} v_{ij} v_{i'j'}^* n_{ii'}^t (E_F^t - E_F^s + eV + E) n_{jj'}^s(E) \tag{2.9}$$

where the E_F's are the Fermi levels of the unperturbed systems, and $v_{ij} = \langle \eta_i | v | \theta_j \rangle$ is a tip–sample coupling element. The energy levels of the tip sites have been shifted to accommodate the bias and contact potential of the junction. In eq. 2.9,

$$n_{jj'}^s(E) = (-1/\pi) \ \mathrm{Im} \ G_{jj'}^s(E + i0) \tag{2.10}$$

with $G_{jj'}^s(z)$ a Green function element of the sample for the complex energy z. A similar expression is defined on the tip side. The diagonal elements $n_{ii}^t(E)$ and $n_{jj}^s(E)$ are the local densities of states on sites i and j of the tip and sample, respectively. These elements were computed by recursion [77]. This technique, originally designed for the calculation of diagonal elements of the Green function, also gives access to non-diagonal elements [78]. For a real symmetric Hamiltonian matrix with one orbital per atom, non-diagonal elements can be obtained as follows

$$\begin{aligned} G_{jj'}(z) = G_{j'j}(z) \ &= \ \langle \frac{\theta_j + \theta_{j'}}{\sqrt{2}} | (z - H)^{-1} | \frac{\theta_j + \theta_{j'}}{\sqrt{2}} \rangle \\ &\quad - \frac{1}{2} [G_{jj}(z) + G_{j'j'}(z)] \end{aligned} \tag{2.11}$$

The NT Green function was computed with C π orbitals only, assuming a constant hopping interaction of -2.9 eV between first-neighbor atoms.

In applications for CNTs, the STM current was calculated with eq. 2.9 by considering just one atom i at the tip apex with an s atomic orbital, like in Tersoff-Hamann theory. A Gaussian function of 6 eV full width at half maximum was chosen to represent the tip density of states at the apex $n_{ii}^t(E)$. On the sample side, the CNTs were described with one π orbital per atom. The tip–sample coupling interactions were *sp* Slater-Koster hopping terms having the following expression [75]:

$$v_{ij} = v_0\, w_{ij}\, e^{-d_{ij}/\lambda} \cos\theta_{ij} \tag{2.12}$$
$$w_{ij} = e^{-ad_{ij}^2} / \sum_{j'} e^{-ad_{ij'}^2} \tag{2.13}$$

where d_{ij} is the distance between the tip atom i and the sample atom j, θ_{ij} is the angle between the orientation of the π orbital on site j and the ij direction. The Gaussian weight factor w_{ij} was introduced for convergence reasons. The parameters used are $\lambda = 0.085$ nm and $a = 60$ nm^{-2}. The prefactor v_0 does not matter as long as absolute values of the current are not required.

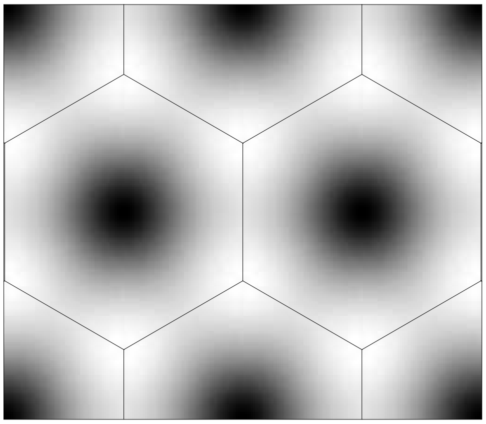

Figure 2.8: Calculated gray scale STM current map at constant height (0.5 nm) above a graphene sheet. The tip potential is 0.25 V. Thin black lines show the graphene hexagonal lattice, with atoms at the vortices of the hexagons. See the text for details. From [79].

As a first application of the tight-binding formalism STM image of a single graphene sheet was calculated, see *Fig. 2.8.* We can see corrugation valleys that correspond to the center of the hexagons of the honeycomb structure (overlaid on the image by black lines). Around the hexagonal holes, there is a network of protruding C-C bonds. The hexagonal atomic lattice does not show up in the image, instead a triangular lattice made of the valleys is seen.

When coupling two or more graphene layers with the Bernal graphite stacking, the two atoms per unit cell become unequivalent: atom A has a neighbor directly beneath whereas atom B does not. In a small interval around the Fermi level, the LDOS on site A is much smaller than that on B [80]. As a result, the STM current at small bias is larger when the tip is above an atom B, which therefore appears as a protrusion in the constant-current image. This interpretation is considered as the ad-hoc explanation of the fact that only every other two atoms are seen in the experimental STM images of graphite [81]. As can be seen in *Fig. 2.9* there are no marked local maxima of the current at the locations of the A atoms, only the B atoms are seen (as white features). By increasing the bias, the differences

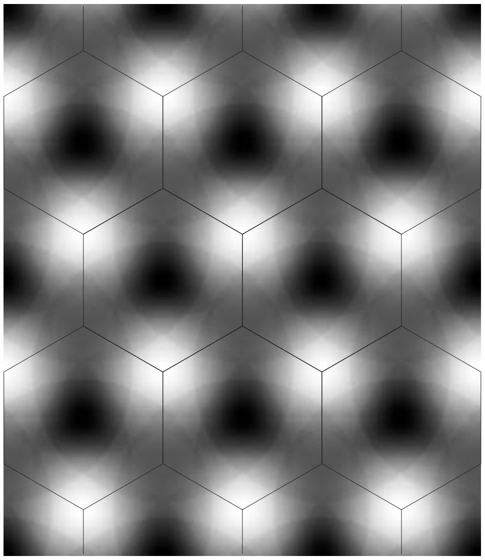

Figure 2.9: Calculated gray scale STM current map at constant height (0.5 nm) above a multilayer graphite surface. The tip potential is 0.25 V, which corresponds to a current ratio $I_B/I_A = 2$. The B atoms are clearly resolved, whereas the A atoms do not come out. Thin black lines show the graphene hexagonal lattice, with atoms at the vortices of the hexagons. See the text for details. From [79].

between the densities of states on A and B sites become less important and the asymmetry washes out gradually.

Fig. 2.10 shows the STM images computed by the tight-binding formalism for four single-wall nanotubes with diameter around 1.4 nm. In agreement with the interpretation of graphene images summarized above, the centers of the honeycomb hexagons correspond to sharp dips of corrugation. In these 2D maps of the radial distance of the tip, the nanotube axis is along the horizontal, x direction. Only the topmost parts of the nanotubes have been imaged. The curvature of the nanotube causes a distortion of the images in the form of an inflation of the y (see Section 4.1.2) as discussed in [75], here by a factor of 1.7. This distortion is clearly visible on the honeycomb lattice that was superimposed on the images. It is also responsible for the elongate shape of the corrugation dips at the center of the hexagons.

In the (18,0) (metallic) zig-zag CNT illustrated in *Fig. 2.10*, the largest protrusions are found on the bonds parallel to the axis. These protruding bonds form a triangular lattice of oblate humps. This resembles the triangular lattice formed by every other two atoms in multilayered graphite. In the (10,10) (metallic) armchair NT, the largest protrusions are realized on the atoms. Here all the bonds look the same and the image has the honeycomb symmetry.

In the case of chiral (11,9) and (12,8) NTs (both semiconductors), one third of the bonds protrudes more than the others, like with the zig-zag geometry, but not always the ones closest to the axial direction. This bond anisotropy again destroys the hexagonal symmetry, as often observed experimentally [82]. In chiral NTs, the protruding bonds form stripes that spiral

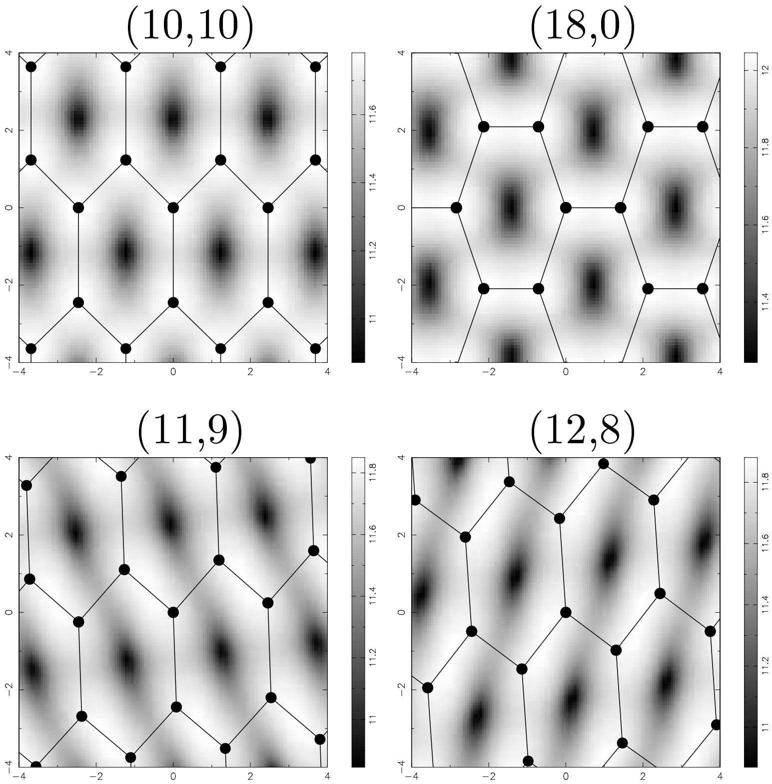

Figure 2.10: Calculated gray scale representation of the axial distance at constant current of the STM tip apex at the topmost part of four single-wall carbon nanotubes. The tube axis is parallel to the horizontal direction. The vertical distance of the tip to the atom located at the center of each image was set to 0.5 nm. For the two metallic, non-chiral (10,10) and (18,0) nanotubes, the tip potential was 0.3 V. The chiral (11,9) and (12,8) nanotubes are semiconductors, with a band gap of $\sim$ 0.6 eV. For both of them, the tip potential was 0.5 V. All coordinates in the figure are in Å. From [79].

around the NT [83]. The elongate holes at the center of the hexagons are no longer aligned with the circumference, as indeed often observed in the experimental images [10, 11], even at room temperature [84].

The images of a semiconducting NT depend on the sign of the bias potential. Neglecting any contact potential that would shift the Fermi level of the semiconductor, the tip potential must exceed half the band gap of the NT to produce a tunneling current. The values +0.4 and -0.4 V were selected for the calculations. With a negative tip, the unoccupied states of the NT are probed. Inversely, a positive tip explores the occupied states.

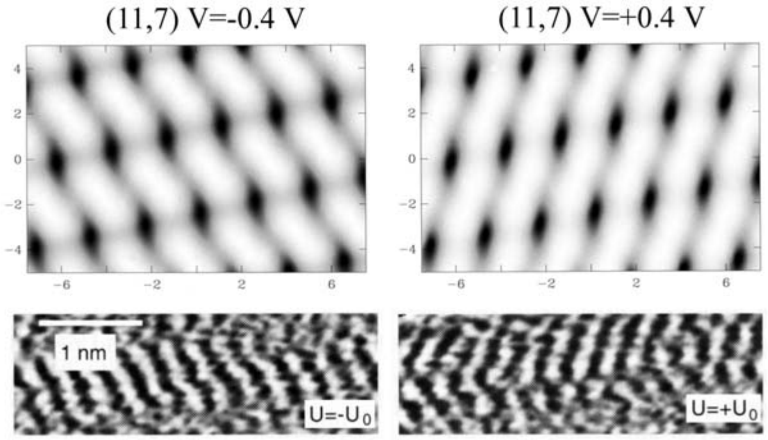

Figure 2.11: Effect of the sign of the bias potential on STM images of semiconducting nanotubes. The two upper images are calculated gray scale topographic STM images for the tip negative and tip positive case. The coordinates are in Å. From [8]. The two lower images are atomic resolution images measured on the same tube with tip negative and positive bias. Ref. [85].

Fig. 2.11(upper) shows the calculated STM images of the (11,7) NT for the tip negative and tip positive case. Increasing the chiral angle of the NT produces a rotation of the strongest bonds [8], which progressively join together and form stripes that spiral around the NT. With reversing the STM bias, the handedness of the spiral stripes are reversed. This complementarity of the STM images upon reversing the bias has been indeed observed experimentally [85]. Interestingly, the image of a semiconducting (n, m) NT not only depends on the sign of the bias potential but it does also depend on whether $n - m$ is a multiple of three plus one or minus one [83].

To summarize, as verified by ab-initio calculations [9], essential features of atomic resolution STM images of SWNTs can be successfully and effectively calculated [75, 83] with the tight-binding method. We calculated an "atlas" of simulated STM images for a series of 27 SWNTs representing all main characteristic variations [8] by this method. The calculations show that the honeycomb symmetry of the graphitic network is almost always broken by electronic effects and the STM images of armchair NTs [8] are the only ones to exhibit the full symmetry of the geometrical structure.

2.5 Effect of the substrate

CNTs have to be deposited on a conducting substrate for STM study, to support the CNTs mechanically and to maintain a closed electrical circuit. Metals (Au, Pd, Pt, etc) and HOPG graphite are used in experiments. In the case of metal support surfaces the most important effect of the substrate on the STM image is caused by the doping of the CNT by the substrate. As seen on the experimental STS curves (see e.g. [10]) and proved by *ab-initio* calculations [9], this charge transfer effect can shift the STS curves of SWNTs by several tenth's of eV. However according to the *ab-initio* calculations [9], for the Au(111)/CNT system, the shape of the wave functions at the Fermi level show still a good resemblance with the wave functions of the free tube, thus the STS curves are unchanged except for the above mentioned shift. For a HOPG substrate, however, charge transfer is minimal.

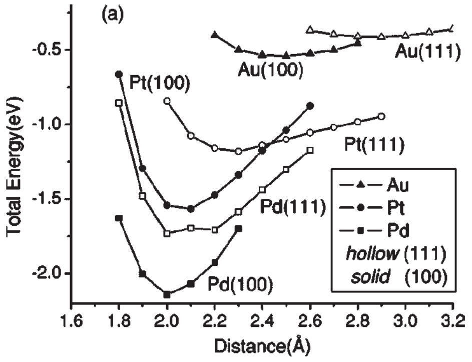

Figure 2.12: Total energy of metal/CNT as a function of interfacial distance. The reference energy is taken as metal/CNT separated by infinite distance. Pt(100) curve is shifted up 0.2 eV for clarity. Ref. [86].

Fig. 2.12 shows the results of *ab-initio* total energy calculations [86] for the metal/CNT system for several metal surfaces. For all metal surfaces considered by that authors, the metal/CNT interface is a Schottky type barrier. The tunnel barrier between the metal surface and the CNT is "punched" for each interface except for the Au(111)/CNT interface, where a shallow and narrow tunnel barrier does exist, with 2.5 eV height (above E_F) and 0.065 nm width. When placed on HOPG, the CNT will "float" on the van der Waals potential [87]. The interlayer spacing of graphene sheets in HOPG and the distance of SWNTs in bundles are roughly similar, 0.34 nm, therefore it is justified to expect the same distance between the CNT and the HOPG substrate. Because of this relatively large distance the barrier between the CNT and the HOPG support surface is a tunnel barrier. Mechanical pressure of the STM tip can, however, lower or even "punch" this tunnel barrier (see Chapter 4).

Chapter 3

Simulation of the STM tunneling phenomenon

3.1 Introduction

To go beyond the simple 1D picture of STM tunneling mechanism (see Section 2.2, *Fig. 2.5*) we has to consider, that

- the edges of the trapezoidal potential are rounded because of long range correlations mimicked by the classical image potential. Hence the effective potential barrier [88] for tunneling is lowered and this effect becomes important for small (< 0.5 nm) tunnel gap values.
- In an STM instrument the electrodes are not flat but one of the electrodes is a tip with an atomically sharp apex. When imaging nanostructures, the local radius of curvature of the sample (curvature on the point below the tip apex) can also be small. Therefore it is necessary to go beyond the 1D approximation.
- When imaging CNTs, the CNT is not an integral part of the support but is "floating" above the support surface [73] at the van der Waals distance. This means that there are two tunnel gaps: one between the STM tip and the CNT and the other between the CNT and its support.

Some of the features of the STM imaging mechanism are of purely geometrical origin. Most important among these is the apparent lateral broadening [25] of the CNTs in STM images caused by the curvature of the tip comparable to (or larger than) the curvature of the CNT. In order to concentrate only on these geometrical effects without the effect of the specific atomic structure, I constructed a three dimensional (3D) jellium potential model of the STM tip – CNT – support tunnel junction. Due to the characteristic lengths of this model, comparable to the λ_F Fermi wavelength of the electrons and to the micrometer electronic coherence lengths [89] in SWNTs quantum interferences [90] and multiple scattering are important ingredients to account for in a realistic model of tunneling through SWNTs.

The basic ideas and restrictions of the method I developed are as follows.

- The tunneling problem is regarded as a problem in potential scattering theory [91]. The current density is determined by calculating the scattering of wave packets (WPs) incident on the barrier potential.
- The method applies to localized barriers. By localized, I mean situations in which nonperiodic spatial variations of the potential occur only over a finite *interface region* of nanoscopic size.
- The initial WPs are constructed from the stationary states of the reservoir from which the WPs are arriving. The initial WP is formed in such a way that its envelope function will have a constant plateau of larger size than the spatial dimension of the interface region.
- The total tunnel current at a given STM bias is a statistical average of the tunnel currents for WPs of different allowed incident energies and directions ($\vec{k}$ vectors) weighted according to the band structure of the two reservoirs.

Because of the limited computational facilities my earlier calculations were done on a two dimensional (2D) model. 2D calculations, presented in Chapter 4, describe important features of STM tunneling that 1D models can not account for, e.g. tip convolution, the effect of point contacts, and the geometric asymmetries in $I(V)$ curves.

The electrostatic potential of the rotationally symmetric tip and the spread of the charge along the tube during tunneling which may be important for metallic tubes can not be accounted for in the 2D model. The net effect is that the 2D model overestimates the tip - tube conductance as compared to the tube - support conductance because it does not take into account that the tip - tube tunnel junction is zero dimensional but the tube - support tunnel junction is one dimensional. Recent advances in computer power permitted me to address the full 3D geometry of the problem and thus to handle the WP spreading phenomenon. 3D calculations are presented in Chapter 5.

3.2 Jellium potential model

My potential model of the STM tip – NT – support system is a generalization of the 1D potential model shown in *Fig. 2.5.*

The geometry of the model system is shown in *Fig. 3.1.* The support is assumed to be a flat surface. The NT is modeled by a cylinder of 0.5 nm radius floating above the support at a distance of 0.335 nm as measured from the surface of the support to the wall of the NT. This is the distance of the graphene sheets in HOPG and similar distances have been found between the elements of the SWNT ropes [39]. The STM tip is taken as a rotational hyperboloid of 0.5 nm apex radius and 15° aperture angle. The particular, arbitrary choice of a hyperbolic tip shape does not influence the qualitative character and the main numerical trends obtained from the calculation. The hyperbolic shape, however, makes it easy to calculate the electric field analytically for rotationally symmetric arrangements.

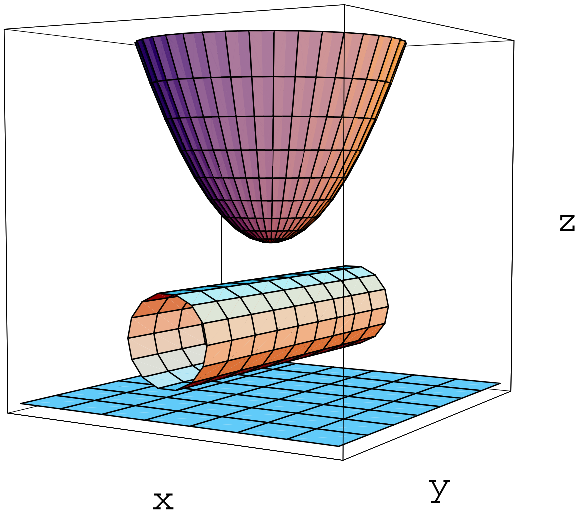

Figure 3.1: (color) Model system with STM tip, nanotube, and support surface. Size of the box is 4 nm.

In the case of the 2D calculations I used the cross section of the 3D potential, i.e. $V_{2D}(x,z) = V_{3D}(x, y = 0, z)$. Hence in this case the system is made translation symmetric in the y direction, i.e. the tip is a hyperbolic cylinder in the 2D model and the tip–tube tunnel junction is infinitely long in the y direction.

The potential $V(\vec{r}) = V_{jell}(\vec{r}) + V_{elst}(\vec{r})$ of this system consist of the jellium potential $V_{jell}(\vec{r})$ and the electrostatic potential $V_{elst}(\vec{r})$. The jellium potential describes the binding of the electrons inside the electrodes the same way as used in the 1D model of *Fig. 2.5.*

The decrease of the tunnel barrier due to the finite jellium radius (see Section 3.1) is accounted for by assuming the effective surface of the electrodes to be 0.071 nm outside the geometric surface. This is the half nearest neighbor distance in HOPG. My model potential is *zero* outside the effective surfaces of the electrodes and -9.81 eV inside. This is calculated from the HOPG $E_F = 5$ eV Fermi energy [92] and $W = 4.81$ eV work function [93]. This model potential does not account for the different material properties of the tip, NT, and support, it allows the calculation of the influence of the geometry on the tunneling current only.

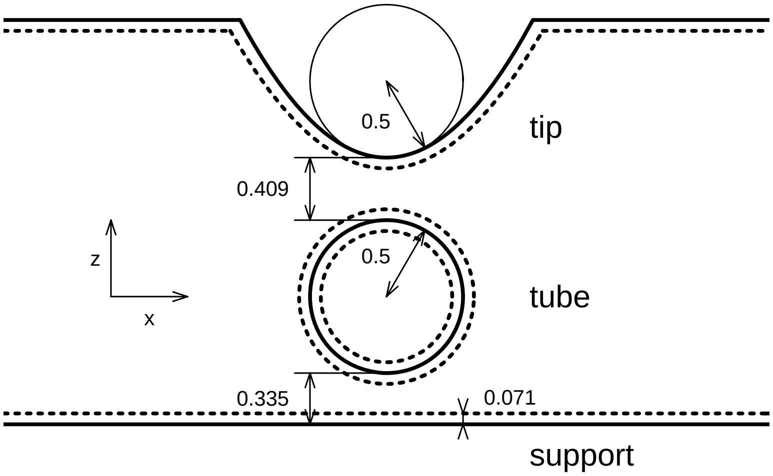

Figure 3.2: Geometric surfaces (full line) and effective surfaces (broken line) of the tip, nanotube, and support. All dimensions are in nm. From [74].

As was shown [94] the self-consistent electronic structure of NTs represented by the jellium model compares favorably with parametrized LCAO calculations that take atomic structure into account. The absence of atomic structure in the jellium tubes is equivalent to averaging over all chiral angles.

3.2.1 The electrostatic potential

Electrostatic potential in the STM tip – NT – support tunnel junction is arising from several sources: *i)* external bias U_t, *ii)* contact potential due to the different Fermi levels, and *iii)* image potential. In this work focussing on geometric effects all objects are assumed to have the same material parameters, hence the contact potential is zero. The lowering of the tunnel barrier due to the image potential [88] is partly accounted for by assuming the effective jellium surfaces to be 0.071 nm outside the geometric surface, as explained in Section 3.1

Electrostatic potential V_{elst} due to the U_t STM bias is calculated in the following way.

All the three objects (tip, CNT, and support) are assumed to be perfect conductors for the electrostatic field calculation. For metallic CNTs this is a plausible assumption because of their small screening length [95, 96]. The $U_{support}$ and U_{tip} potentials are fixed by the STM setup: $U_{support} = 0$, $U_{tip} = U_t$. The CNT is considered to be isolated, hence its charge $Q_{tube} = 0$. Next I calculated the charge density distribution $\sigma_i(\eta, \xi)$ on the surface of each of the electrodes $i\epsilon\{tip, tube, support\}$, where η and ξ are the parametric coordinates (inner coordinates) on the surface of the electrodes. This was done using the capacitance matrix method [97], see Appendix A for details. $V_{elst}(\vec{r})$ is then calculated from $\sigma_i(\eta, \xi)$ by direct integration.

Fig. 3.3 shows the electrostatic potential of the 2D STM model. From the $U_{support} = 0$ V, $U_{tip} = 1$ V, and $Q_{tube} = 0$ C conditions the capacitance matrix method gives $U_{tube} = 0.376$ V.

In non-metallic tubes the electrons cannot move freely along the tube axis. Thus my perfectly conducting ring model is valid for the semiconducting tubes if only the electrons can move freely along the circumference of the tube.

3.2.2 The drain potential

In the wave packed dynamical method (see Section 3.3) the time dependent Schrödinger equation is solved on a finite spatial region. This finite region includes the localized part of the potential, the potential is zero (or constant, or at least translation symmetric) outside this region. We have to solve the time dependent Schrödinger equation for the finite region in such a way that the solution should be the same as if we solved the time dependent Schrödinger equation for the whole space and then we cutted the part corresponding to the finite region from the total wave function. In other words the finite region is a window (I call it presentation window) to the whole solution. This can be achieved by the so called absorbing boundary condition.

I solve the time dependent Schrödinger equation using the split-operator FFT method (see Section 3.3.1). This method introduces an artificial periodic boundary condition into the solution. To prevent unphysical interference effects among the neighboring cells, the edge of the presentation window is closed by an absorbing layer.

The absorbing layer should be such that for the WP arriving into this layer

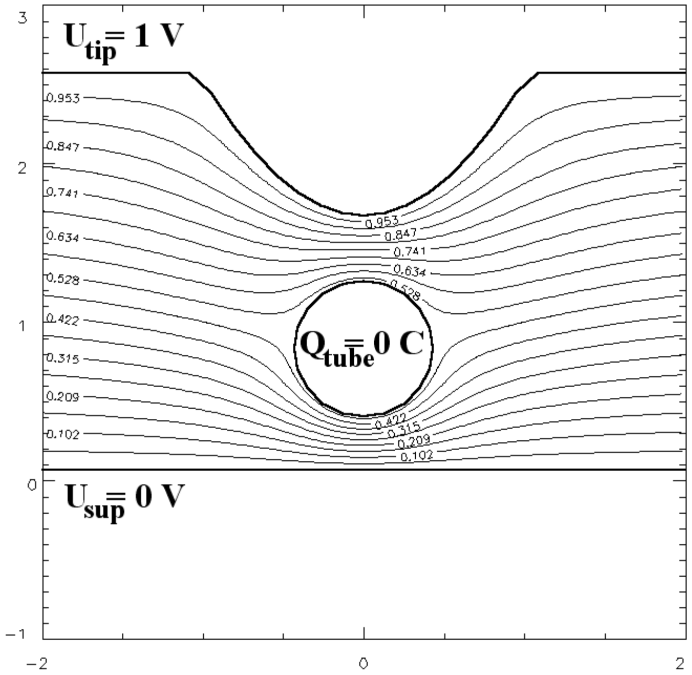

Figure 3.3: Equipotential lines of a 2D STM model with a CNT of 1 nm diameter. All dimensions are in nm.

there should be no reflection and no transmission, the WP has to "disappear" simply – be absorbed in the layer. Numerically this means that both the reflection and the absorption has to be negligibly small and also the width of the absorbing layer has to be as small as possible, in order to minimize computing time and memory requirements.

For the Schrödinger equation the absorbing layer can be realized by a region of negative imaginary potential. Thus the total potential is complex, with:

$$V(\vec{r}) = V_{jell}(\vec{r}) - iV_{drain}(\vec{r}) \tag{3.1}$$

where $V_{jell}(\vec{r})$ is the jellium potential and $V_{drain}(\vec{r})$ is the absorbing potential.

The norm of the wave function is not conserved for an imaginary potential, the magnitude of the WP is exponentially decreasing in a region of a constant negative imaginary potential. Hence, if the absorbing region is thick enough, the transmission can be made arbitrarily small. Not only the transmission, but also the reflection has to be negligibly small, however. This can be accomplished by a non constant imaginary potential. In order to find the best absorber I performed numerical experiments for different absorbing potentials. A WP was "shot" into the absorbing potential and the reflection and transmission probability was "measured" inside the computer. These experiments revealed that the absorbing potential has to increase gradually to prevent reflection. Gradual refractive index is also used in broadband optical antireflection coatings [98]. According to the numerical experiments I choose the following absorbing potential:

$$V_{drain}(\vec{r}) = \frac{V_{drain\,max}}{d_{drain}^3} \begin{cases} (|\vec{r}| - r_0)^3, & \text{if } |\vec{r}| > r_0; \\ 0, & \text{otherwise} \end{cases}, \tag{3.2}$$

which means that the absorbing potential is zero inside a sphere of radius r_0 and is slowly "switched on" outside this sphere. Here d_{drain} is the width of the absorbing potential and $V_{drain\,max}$ is its maxium value, i.e.

$$V_{drain}(r_0 + d_{drain}) = V_{drain\,max}\,. \tag{3.3}$$

For the 2D calculation the width of the absorbing potential was 3.84 nm and the maximum value 4.35 eV. For the 3D calculation a smaller, 3.044 nm wide absorber was chosen to speed up computation with maximum value 8.71 eV. For these parameters both the reflection and the transmission is less than 10^{-6} for an $E = 5$ eV WP. According to the numerical experiments, optimized drain potentials [99] give similar R and T values for these parameters.

3.3 The wave packet dynamical method

Erwin Schrödinger introduced the concept of wave packets [100] to bridge the gap between classical and quantum descriptions of nature. The wave packet dynamical (WPD) method [101, 102] is a scattering experiment inside the computer: an incoming WP is "shot" into the localized potential under investigation and the time development of the WP is calculated by solving the time dependent Schrödinger equation. The "result" of the wave packed dynamical calculation is the time development of the WP itself – it gives insight into the details of the time dependent process – and also allows that selected measurables be calculated from the outgoing (scattered) WP. These measurables are those quantities measured in a real scattering experiment.

In the case of an STM model the WP is approaching the STM tunnel junction from inside of the tip bulk (or from the support bulk) and we study the tunneling of this WP into the other electrode, the support (or into the tip). Given the initial state $\psi_0(\vec{r};t)$ and the localized potential $V(\vec{r})$, the $\psi(\vec{r};t)$ wave function is calculated from the time dependent Schrödinger equation.

This conceptionally simple and easy to implement method contains no perturbative approximation but includes all interference [90] and multiple scattering effects and thus it is capable of providing results comparable with advanced tunneling theories [103] when applying a properly chosen model potential. Inclusion of multiple scattering and interference effects is important for modeling the resonant tunneling process arising because of the existence of two tunnel gaps.

In free space the time evolution of a WP is quite simple: it is a translational movement with constant $\vec{v}_0$ velocity and a spreading with a doubling time $\tau_2 = 2\sqrt{3}\,(\Delta x)^2$. See Appendix B for a brief summary of the most important properties of WPs. For a complicated potential, however, wave packet dynamics reveals a whole lot of interesting phenomena, e.g. the WP is split into several parts in space and time, periodic or quasi periodic motion occurs (so called quantum revivals [104]), etc. In Chapter 4 I mostly focus on the final state and the measurables calculated from the final state. In Chapter 5 I study the time evolution itself in the STM model.

3.3.1 The split-operator FFT method

Time evolution of the wave function is governed by the time dependent Schrödinger equation:

$$i\frac{\partial\psi(\vec{r};t)}{\partial t} = \mathbf{H}\psi(t). \tag{3.4}$$

Formal solution can be written using the time development operator:

$$\psi(\vec{r};t) = \mathbf{U}\psi_0(\vec{r};t) \qquad \mathbf{U} = e^{-i\mathbf{H}(t-t_0)} \tag{3.5}$$

If the potential is conservative, then $\mathbf{H} = \mathbf{K} + \mathbf{V}$ where the kinetic and potential energy operators do not commute in general, hence the exponential in eq. 3.5 can not be factored. Note, however, that we can decompose [105, 106] the exponential by the symmetrical unitary product

$$e^{-i(\mathbf{K}+\mathbf{V})\delta t} = e^{-i\mathbf{K}\delta t/2} e^{-i\mathbf{V}\delta t} e^{-i\mathbf{K}\delta t/2} \tag{3.6}$$

The error of this approximation is $O\left[(\delta t)^3\right]$.

According to eq. 3.6 the action of the evolution operator is split into three consecutive steps: a free propagation for time $\delta t/2$, a potential only propagation for time δt and again a free propagation for time $\delta t/2$. If the potential

V is local, then its effect is a simple multiplication with $V(\vec{r})$, hence the effect of the potential energy propagator $\exp\left(-i\mathbf{V}\delta t\right)$ is a multiplication with $\exp\left(-iV(\vec{r})\delta t\right)$. The effect of the kinetic energy propagator $\exp\left(-i\mathbf{K}\delta t/2\right)$ is given in k space by multiplicating the $\varphi(\vec{k};t)$ momentum space wave function by $\exp\left(i|\vec{k}|^2\delta t/4\right)$ To utilize this formula it is necessary to calculate the $\varphi(\vec{k};t)$ momentum space wave function by fast Fourier transform (FFT) of $\psi(\vec{r};t)$. Finally we have to return back to real space by inverse FFT, i.e.:

$$e^{-i\mathbf{K}\delta t/2}\psi(\vec{r};t) = \mathcal{F}^{-1}\left[e^{i|\vec{k}|^2\delta t/4}\mathcal{F}\left[\psi(\vec{r};t)\right]\right] \tag{3.7}$$

The evolution of the wave function over a time step δt is calculated in a straightforward way: first eq. 3.7 is applied, then the result is multiplied by $\exp\left(-iV(\vec{r})\delta t\right)$, and finally eq. 3.7 is applied again. Convergence towards the exact result is obtained by using a small δt.

3.3.2 Construction of the initial state

For infinitesimally small bias calculation the WP is launched with the Fermi momentum $\vec{k}_F$ from inside the tip bulk towards the apex of the tip or from inside of the support bulk towards the NT.

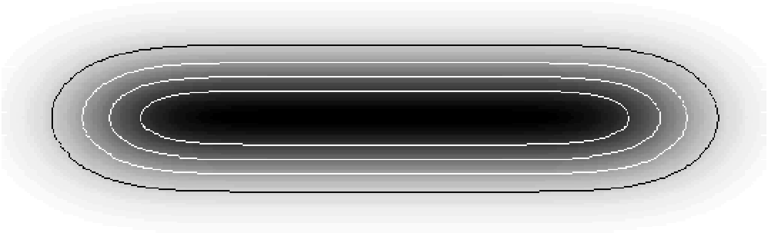

Figure 3.4: A truncated plain wave wave packet. White shows the zero density and black the maximal density.

To eliminate the effect of the particular WP shape on the resulting tunneling probability the width of the WP has to be larger than the largest half width of the tunneling channel: $\Delta x >> HW_T$. In atomic resolution STM measurements HW_T is around 0.1 - 0.2 nm [91]. I used $\Delta x = \Delta y = \Delta z =$ 0.37 nm. For the special case of the NT raft, when the WP is coming from the support (see Section 4.2), the total lateral size of the interface region is more than 1 nm, see. *Fig. 4.14.* This would require the use of a Gaussian WP with fairly large Δx which would subsequently require a fairly large spatial mesh. To avoid this difficulty I constructed a WP called *truncated plane wave* which has a plateau of constant probability density larger than the interface region. Such WP can be constructed as a convolution of a Gaussian with a square window function. To compensate for the effect of the distortion of the plateau during the time development of the WP a backward time propagator is used to construct the initial state:

$$\psi_0(x,z) = N\cdot\hat{P}_{t_0}\left[\int_{d_1}^{d_2} \exp\left(-\frac{(x'-x)^2}{a^2} + ik_x x\right) dx'\right]\cdot\exp\left(-\frac{(z-z_0)^2}{a^2} + ik_z z\right) \tag{3.8}$$

where $d_1 = -1.52$ nm, $d_2 = 1.52$ nm, $a = 0.529$ nm, and N is a normalization constant. (Eq. 3.8 is a 2D expression, as used in Chapter 4.) By the free space propagator $\hat{P}_{t_0}$ the truncated plane wave is backward propagated in time by an amount of $t_0 = (z_0 - z_{interf})/v_z$ where z_0 is the initial z position of the center of the WP, z_{interf} is the z position of the first tunneling interface, and $v_z = k_z$ is the z component of the group velocity. The z_0 initial position was chosen to make the probability density of the initial WP negligible in the interface region. *Fig. 3.4* shows a grayscale plot of a truncated plane wave WP.

3.3.3 Choice of the measurables

The method of analyzing the resulting large wave function dataset basically relies on calculation of integrals of certain quantum mechanical observables derived from the wave function on carefully chosen subspaces. As a first step two important observables are calculated from the wave function: the $\varrho(\vec{r};t) = |\psi(x,y,z;t)|^2$ probability density and the $\vec{j}(\vec{r};t)$ probability current density.

$j(\eta,\xi;t)$, the perpendicular component of the $\vec{j}(\vec{r};t)$ probability current density flowing across selected $\mathcal{S}$ *measurement planes*, gives the 2D map of the probability current crossing those planes as the function of time, where η and ξ are the parametric coordinates (inner coordinates) of the plane. $\int j(\eta,\xi;t)d\eta\, d\xi$ gives the $I(t)$ probability current crossing the particular measurement plane as the function of time. By calculating the indefinite integral $T(t) = \int_0^t I(t')dt'$, we determine the transmission vs. time, i.e. the portion of the WP that has crossed the measurement plane until time t. The $T(t=\infty)$ asymptotic value gives the total transmission for that plane.

Volume integral of $\varrho(\vec{r};t)$ for selected $\mathcal{V}$ *measurement volumes* gives the probability of finding the particle in those volumes at the instant t, $P(t) = \int \varrho(\vec{r};t)dV$. Integration for the whole space gives $P(t) \equiv 1$.

Integrating $P(t)$ in time [107] gives the *dwell time* [108, 109], the average time spent by the particle in $\mathcal{V}$:

$$t_{spent} = \int_0^\infty \left(\int_{\mathcal{V}} \varrho(\vec{r};t) dV \right) dt \,. \tag{3.9}$$

By exchanging the integrals in eq. 3.9 the dwell time can be written as a volume integral:

$$t_{spent} = \int_{\mathcal{V}} \tau(\vec{r}) dV \tag{3.10}$$

where

$$\tau(\vec{r}) = \int_0^\infty \varrho(\vec{r};t) dt \tag{3.11}$$

is the *dwell time density.*

Estimates for the WP transmission time (tunneling time) and reflection time based on the WPD results will be made in Section 5.6.1.

3.4 Summary

Throughout this chapter, I have introduced the methods I use in the thesis for the simulation of tunneling in STM tip – CNT – support systems. These methods go beyond the simple 1D picture of STM tunneling mechanism and take into account the specific shape of the potential barrier. The STM tip, the CNT, and the support are modeled by constant potential jellia. Electrostatic field distribution due to the applied STM bias is calculated utilizing the capacitance matrix method. Open boundary conditions for the wave function are realized by an absorbing potential. The tunneling probability of the STM model is calculated from the time dependent wave function by solving the time dependent Schrödinger equation with the split-operator FFT method. Specifically designed initial states were applied to eliminate the effects of wave packet shape on the results. The $\varrho(\vec{r};t)$ time dependent probability density and the $\vec{j}(\vec{r};t)$ time dependent probability current density is calculated from the wave function. Measurables, as transmission probabilities and characteristic times were calculated from these quantities.

Chapter 4

Geometrical factors influencing the STM imaging process

4.1 Tip convolution

As a general rule, it can be formulated that in scanning probe microscopy, independently of which object was chosen as tip, always the sharper object (with the smaller radius of curvature) will generate the image (see *Fig. 4.1*). The effect of the comparable characteristic radii of the sample and the tip is generally called *tip convolution effect.* This denomination comes from the concept that the sharp features of the sample surface are smeared in the STM image because of the finite width of the STM tip – sample tunneling channel. This smearing can be calculated approximately as a mathematical convolution of the "real" sample topography with the window function describing the cross section of the tunneling channel.

Figure 4.1: Illustration of the distortion arising due to tip-sample convolution effects for objects with different shapes. When the object becomes sharper than the tip, the object will generate the image of the tip. From [70].

Carbon nanostructures are 3D objects with characteristic radii of curvature in the nm range. This value is comparable on the one hand to the characteristic value of the tip-sample tunnel gap (which is between 0.2 -

0.5 nm in typical STM experiments) and on the other hand to the apex radius of the STM tip. This makes the interpretation of STM images of carbon nanostructures different from that of flat surfaces. Atomic resolution can be achieved when the STM tip presents a nanoprotrusion effectively terminated with a single atom. Even with this ideal tip, only the topmost part of a NT can be imaged. With a blunt tip, no atomic resolution can be achieved on a NT and the STM provides only a geometric information [110]. Furthermore, tip-shape convolution effect makes the width D of a cross-sectional profile along a NT appear typically much larger than the actual tube diameter. This broadening is very well seen in the line cuts of *Fig. 2.6* and *Fig. 2.7*.

4.1.1 Geometrical line cut

Because of its exponential distance dependence the tunneling current tends to follow the shortest path between the tip and tube and the corresponding "off-z" component of the current increases as the tip moves aside to the tube [111]. Assuming a uniform local density of states (LDOS) on the sample and tip surfaces the effect of the feedback loop can be taken into account approximately by keeping the length of the tunneling path at a constant value. The curve drawn by the apex point of the tip when using this simple approximation is called a *geometric line cut.* I have calculated the geometric line cut by moving the tip along a line in a way that the distance of the nearest point of the sample and of the tip remain a (pre-selected) constant value, see *Fig. 4.2.* This constant distance is chosen to be 0.4093 nm to allow a direct comparison with the quantum line cut (see Section 4.1.3) at $X_{apex} = 0$. The geometry of the system is the same as described in Section 3.2.

We have used a similar method earlier in simulating larger scale (micrometer) AFM images [112, 113]. In this method the AFM image is simulated by moving the tip along a line in a way that it constantly touches the sample surface. If the sample surface is not flat the contact point of the tip is changing and if the curvature radius of the tip is not negligibly smaller than the curvature of the features of the sample this will cause the apparent broadening of these features on the AFM image. The novelty of my approach is to enhance this method for the case of STM investigation of nanostructures. In this case the tip apex radius and the characteristic radius of curvature of the features of the sample surface are not in the μm range as in case of AFM but in the nm range. Therefore the tip-sample tunnel gap, beeing in the very same nm range, can not be neglected in case of STM.

As it is demonstrated in *Fig. 4.2*, when the tip follows the curvature of the NT, the tunneling point moves away gradually from the tip apex to its side.

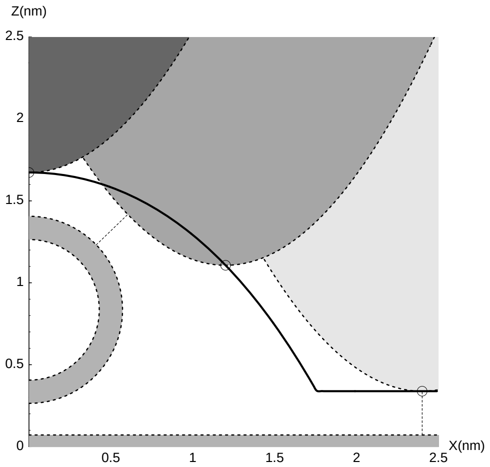

Figure 4.2: The thick line is the geometric line cut drawn by the apex of the tip (marked by open circle). The shaded lower half plane, middle ring and upper hyperbolas show the vertical cross sections of the sample, nanotube, and tip, respectively. The electrodes are bounded by their jellium effective surfaces (broken lines). Several, typical tip positions are shown, with different shades of grey. For each tip position shown, the nearest tip and sample points are joined by a thin dashed line. From [79].

However, when the tip apex approaches the support surface the tunneling is switched back from the side of the tip to the apex, but now the tunneling current is flowing already directly into the support. After this switching the tip follows a line parallel to the support surface. As demonstrated in Section 4.1.3 this simple geometric model is justified by WPD calculations.

4.1.2 Asymmetric stretching of the SWNT image

The effect of the comparable values of the characteristic radius of the sample and the tunnel gap is explained in *Fig. 4.3.* It causes a stretching of the image of the atomic lattice in the direction parallel to the sample curvature. To study this effect the tip radius was assumed to be zero throughout this Subsection.

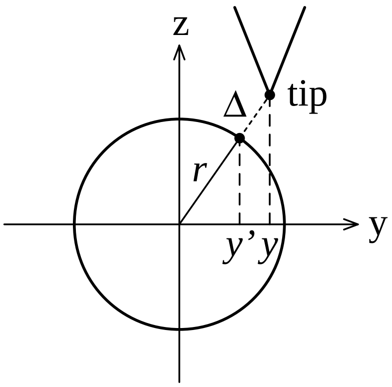

Figure 4.3: Relation between the position of the STM tip (y) and that of an imaged atom (y') of the nanotube when the tunneling current follows the shortest path between tip and nanotube (dashed line). Ref. [75].

Using the geometric approximation discussed above we assume the tip-sample gap to be a constant Δ value. (The effect of the atomic lattice causes only a small variation on the order of 0.1 nm to this constant gap.) Hence when the tip scans above a nano object with radius of curvature r its apex moves on a circle of radius $r + \Delta$. As a consequence the features on surface of the radius r are projected onto the radius $r + \Delta$ surface and are therefore stretched by a factor of $(r + \Delta)/r$. In the special case of a CNT, the radius of curvature is small only in the direction perpendicular to the tube axis (say, y direction) but it is infinite in the direction parallel to the tube axis (x direction). This causes an asymmetric stretching in the atomic resolution STM images of small diameter NTs: the atomic lattice is inflated in the y direction. This stretching is reproduced in tight-binding calculated atomic resolution STM images of CNTs [8]. It is also seen in experimental STM images taken on SWNTs [114, 115]. Due to the asymmetric distortion, the angles between the C-C nearest neighbor bonds measured on the STM image also deviate from $\pi/3$.

4.1.3 Quantum line cut

My first application [116, 117] of the WPD method in the field of STM investigation of carbon nanostructures was to check the validity of the simple geometric line cut method presented in Section 4.1.1. I have performed quantum mechanical probability current calculations through a simple 2D jellium potential modeling the STM tip – NT – support system. The geometry of the system is the same as used Section 4.1.1. The STM constant current loop was simulated by finding for each X_{apex} lateral tip displacement that Z_{apex} vertical tip displacement which yielded a constant tunneling probability. The result of this approach hereafter is referred as *quantum line cut*.

The quantum mechanical tunneling probability is calculated from the time dependent scattering of a WP on the effective potential model of the system (see Section 3.2). An infinitesimally small bias approximation was used, this is justified by the fact that in the experiments analyzed [116, 117] here (see Section 4.1.4) small bias values were used. The initial WP was a Gaussian approaching the apex of the tip from inside of the tip bulk with kinetic energy $E = E_F = 5$ eV and $\Delta x = \Delta z = 0.37$ nm.

The probability density of the scattered WP is shown in *Fig. 4.4* for selected time instants and X_{apex} lateral tip displacements. Complete time evolution is shown on the Web as an animation, see

`www.nanotechnology.hu/pub/kirchberg98`.

(The corresponding Z_{apex} vertical tip displacements are calculated using the method described below.)

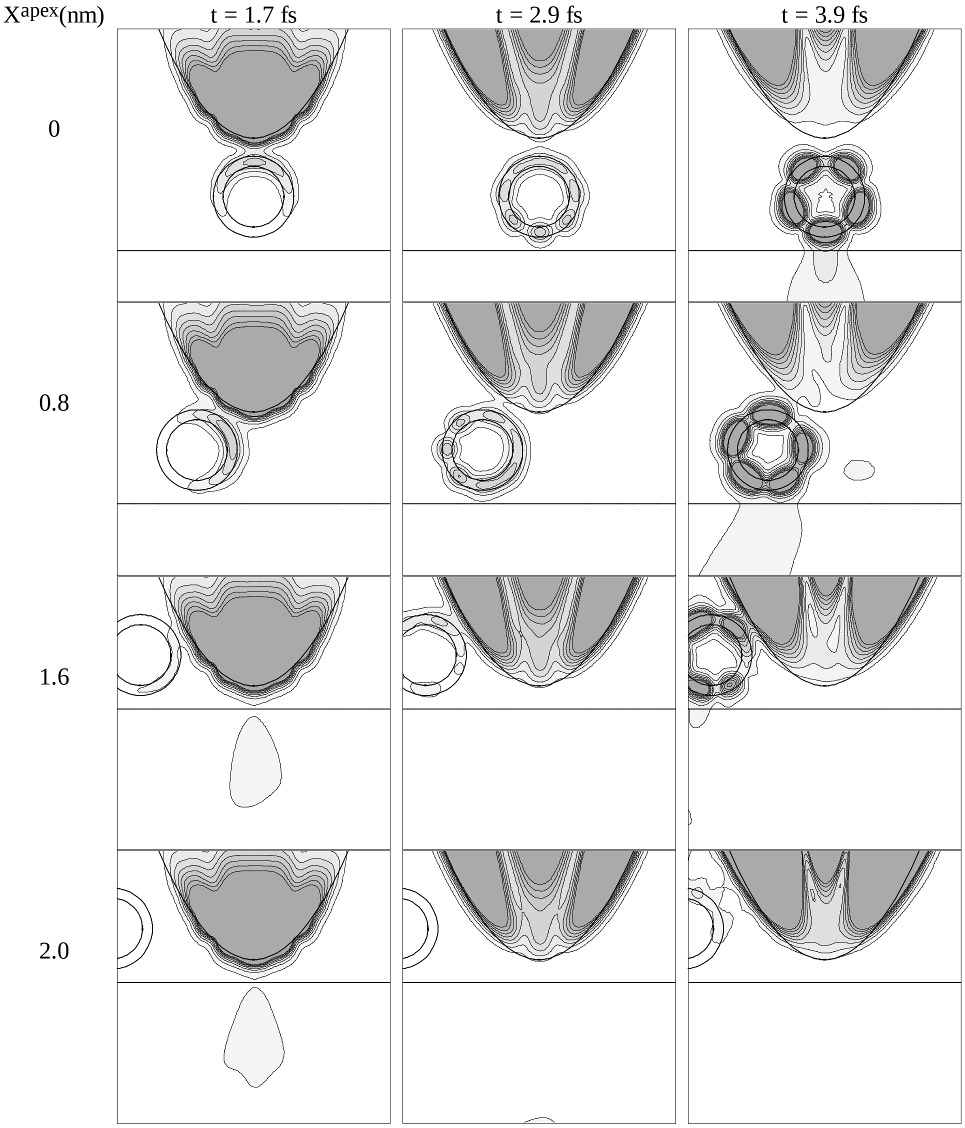

Figure 4.4: Probability density of the scattered wave packet for selected time instants and X_{apex} lateral tip displacements (0.0, 0.8, 1.6, and 2.0 nm). Size of the presentation window is 3.84 nm. Contour lines are drawn on a square root scale. Each frame is normalized to its maximum density. Maximum density values are 4.2, 0.6, and 0.07 nm^{-2} for 1.7, 2.9, and 3.9 fs, respectively. Density in the tube region becomes appreciable on the lower right frame because of the renormalization (see the text for explanation). From [116].

$X_{apex}(nm)$	Forbidden	Tube	Total Interface
0.0	0.071	0.084	0.155
0.8	0.079	0.123	0.202
1.6	0.060	0.020	0.080
2.0	0.057	0.0001	0.057

Table 4.1: Average time t_{spent} (in *fs*) the quantum particle spends in the different regions. "Forbidden" region is the region of zero potential. "Total interface" region is the union of the "forbidden" and "tube" regions.

The average time the quantum particle spends [109] (see 3.3.3) in the different regions of space,

$$t_{spent} = \int_0^{t_{max}} \left(\int_{region} |\psi(x,z;t)|^2 \, dz \, dx \right) dt \,, \tag{4.1}$$

are given in *Table 4.1.*

The time development of the tunneling WP for different characteristic X_{apex} tip displacement values is as follows.

- For $X_{apex} = 2$ nm tip displacement the tip is far from the NT. The WP is tunneling simply from the tip apex into the plane support. The very small t_{spent} value for the tube region (Cf. *Table 4.1*, last row) corresponds to the negligibly small probability of entering of the quantum particle into the tube region.

- For $X_{apex} = 0$ nm the tip is above the uppermost point of the NT. The tunneling process is more complex in this case than for the previous case. t_{spent} is much longer than for $X_{apex} = 2$ nm. The WP has to tunnel through two tunnel resistances [73] in series, which is characteristic to resonant tunneling. The WP first flows around the NT ($t = 1.7$ fs) then penetrates into the support ($t = 2.9$ fs). At later times the main mass of the probability is scattered back into the tip bulk. The probability which remained in the tube region forms standing wave patterns along the tube circumference and it is leaking into the tip and into the support in distinct impulses [73].

- For $X_{apex} = 0.8$ nm (oblique incidence) the situation is similar to the previous one but the majority of the probability flows out of the tip at its side around the nearest points of the sample and tip (denoted by dashed line in *Fig. 4.2*). Note that the standing wave patterns are rotating around the tube symmetry axis because the initial WP has an angular momentum relative to the tube axis. The t_{spent} values for the tube region (Cf. *Table 4.1*, second column) are the largest for this tip displacement, larger than for $X_{apex} = 0.0$ nm. This is because the initial momentum is not perpendicular to the support surface, the WP needs more time to proceed into the support.

- For $X_{apex} = 1.6$ nm we can observe the switching of the tunneling point from the side to the apex of the tip. First a part of the probability flows from the tip apex directly into the support and later another part flows from a side point of the tip into the tube.

Fig. 4.4 shows the probability density for $t = 1.7$, 2.9, and 3.9 fs time instants. The $t = 0$ fs initial state – not shown – is a Gaussian inside the tip bulk with a circularly symmetric probability density distribution. As time advances, less and less probability remains in the presentation window but the gray scale is renormalized to the maximum density for each subfigure of *Fig. 4.4* for better display. This renormalization causes the otherwise small density in the tube region become visible on the lower right frame. The standing wave patterns that appear on the tip are caused by interferences of the eigenmodes of the tube (see Section 5.3 for a detailed discussion).

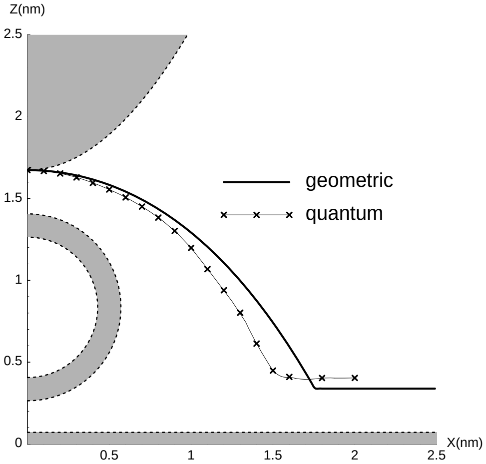

Figure 4.5: Comparison of geometric and quantum line cut. Thick solid line is the geometric line cut. Crosses show calculated points of the quantum line cut. A thin solid line connecting the crosses was drawn to guide the eye. From [116].

Fig. 4.4 shows that the majority of the tunnel current is indeed flowing in a narrow channel around the line section connecting the closest points of the tip and sample, as was assumed intuitively in Section 4.1.1. The STM constant current loop was simulated by finding for each X_{apex} lateral tip displacement that Z_{apex} vertical tip displacement which yielded a constant tunneling probability. This setpoint probability was chosen to be $3 \cdot 10^{-3}$ and it gave a 0.4093 nm separation between the tip and NT geometrical surfaces (at $X_{apex} = 0$ nm). The (X_{apex} , Z_{apex}) tip displacement values resulting from this procedure give the quantum line cut which is shown in *Fig. 4.5* by crosses. The $P_{Gaussian}(E_F)$ tunneling probability of the Gaussian WP at energy E_F is calculated according to the procedure described in Section 3.3.3. The $\vec{j}(x, z; t)$ probability current density is calculated along a horizontal line inside the support bulk (at $z_j = -0.5$ nm) from $\psi(x, z; t)$ for all time instants. Line integration of $\vec{j}(x, z; t)$ along this line gives the $I(t)$ probability current and the tunneling probability is $P_{Gaussian}(E_F) = \int_0^{t_{max}} I(t)dt$. Calculation is performed until the further change of $P_{Gaussian}$ becomes negligible.

The good matching of the geometric and quantum line cut justifies the constant tip-sample separation approximation. The differences of the geometric and quantum line cut are as follows

- According to the quantum mechanical calculation the tip-sample separation is larger above the support plane than over the NT. This is because when tunneling through the NT, the WP has to tunnel two tunnel gaps (tip–NT and NT–support) but it has to cross only one tunnel gap when the tip is over the support plane. This causes a larger tunnel resistance above the NT than above the support plane which makes the feedback loop to retract the tip somewhat when the tunneling point is switched from the NT to the support plane.

- The tunnel gap is decreasing when tunneling into the side of the tube as compared when tunneling into the top of the tube. This is a calculation artefact caused by the normal incidence of the WP: the momentum component in the direction of the tunneling channel is decreasing with increasing angle of the channel with the momentum of the incoming WP. This effect is further discussed in Section 4.2. When integrating for all incidence angles this artefact should vanish.

4.1.4 Discussion of experiments

In this subsection I analyse the tip convolution effect on selected images [73] measured in our Laboratory.

The CNTs used to acquire the experimental data were produced by the catalytic decomposition of acetylene at $700°C$ over a supported transition metal catalyst [28, 118, 119]. The STM samples have been prepared [25] by ultrasonication in toluene of a NT containing material purified from the catalyst. The suspension resulted in this way was drop-dried on freshly cleaved HOPG and the toluene was left to evaporate at room temperature. The STM images were acquired in constant-current mode, using tunneling currents in the range of 0.2 - 1 nA, bias voltages in the range of 0.1 - 1 V, and scan frequencies of 1 - 2 Hz. Mechanically prepared Pt tips were used, the radius of curvature of which were checked with respect to the HOPG surface [73].

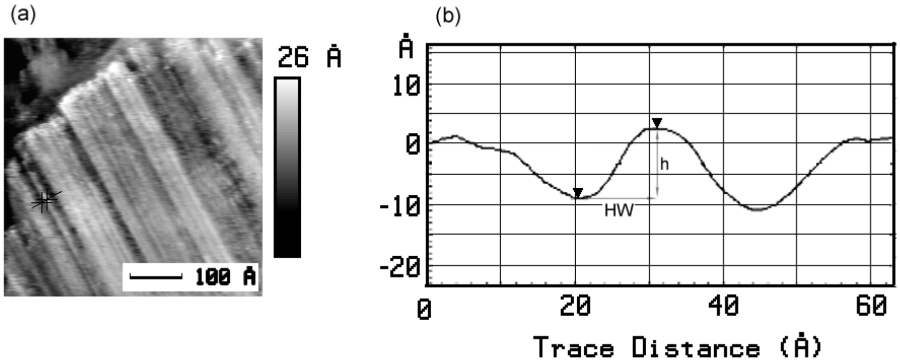

Figure 4.6: STM measurement on a carbon nanotube placed on other nanotubes: *a)* constant current image of a "raft" of carbon nanotubes, $I_t = 0.19$ nA, $U_t = 302$ mV; *b)* the line cut marked in the image by a black line is taken through a tube well separated from other tubes. Note the HW/h ratio close to unity. Ref. [25].

In *Fig. 4.6* the topographic STM image and the corresponding line cut are shown for the case of a CNT placed over other CNTs stacked in a regular way, i. e. on a "raft". One can observe that the ratio of the measured half width, HW, to the measured height, h, is close to unity (1.09). This means that an apparent broadening, (defined as $B = 2HW/h$), by a factor of 2.18 is present in the image.

In *Fig. 4.7* I show an STM image acquired over a NT which is situated on HOPG. The apparent broadening found from the comparison of HW with h is $B = 3.24$. The broadening B was calculated in the assumption that the measured height values, h, are correct. If one takes in account that the NT floats over the support at a height of 0.335 nm, and a similar distance is found between the NTs in a raft, then the corrected broadening B_C will be: $B_C = 2.85$ for the NT over the raft, and $B_C = 4.29$ for the NT over HOPG, respectively.

The comparison of simulated line cuts with the experimental line cuts shows that when the NT is placed on a support with a similar electronic structure (the NT placed on the top of the raft, *Fig. 4.6*), the geometric line cut does not differ significantly from the quantum line cut (see *Fig. 4.5*). The

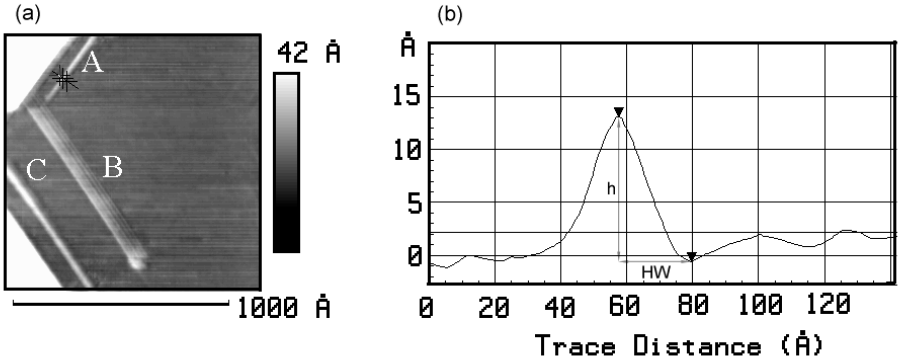

Figure 4.7: STM measurement on a carbon nanotube placed on graphite: *a)* constant current image of individual nanotubes (A and C) and of a "raft" (B) composed of four nanotubes, $I_t = 0.22$ nA, $U_t = 410$ mV; *b)* the line cut marked in the image by a black line is taken through object A. Note the HW/h ratio of 1.62. From [73].

major distortion that influences the apparent tube diameter is the geometric convolution of the tip shape with the tube shape. When the NT is on a support with different electronic properties, i.e., when the NTs are measured on HOPG, gold, or other substrate, the simplification used in the quantum line cut calculation: the penetration and propagation parameters (E_F and W) of the WP in the NT and in the support are identical, is not any more valid. In the case of the geometric line cut this can be taken in account in the first approximation by increasing the value of the tunneling gap over the support as compared to the value over the NT. This is justified because the graphite support used in the experiments is semimetalic. Increasing the width of the tunneling gap over the HOPG as compared to the width over the tube will result in a continuous increase of the distortion found in the apparent diameter of the NT with the increase of the difference in the electronic structure of the NT as compared to graphite.

The ratio of HW to h versus the increase of the width of the tunneling gap over the support is shown in *Fig. 4.8.* Comparing the case of the NT over the raft, i.e. identical electronic structure, with *Fig. 4.8*, one may conclude that in the experimental case the distortion agrees within the experimental error with the value corresponding to zero tunnel gap increase in the figure.

Another consequence of the fact that the NT is not an integral part of the support, but it is floating on the van der Waals potential over it is that when performing $I(V)$ spectroscopy, one has the response of a complex system

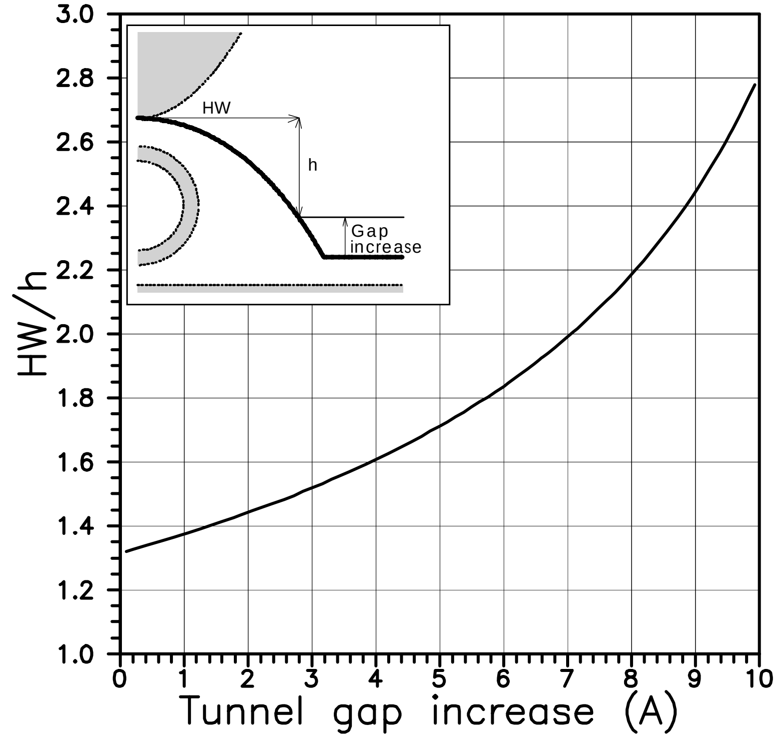

Figure 4.8: HW/h versus the increase of the tunneling gap above the support. Definition of HW, h, and gap increase is given on the geometric line cut shown on the inset. From [116].

to the changes of the voltage applied to the tunneling gap. This is shown by the differences in the average times (see *Table 4.1*) spent in the different regions. t_{spent} is three times greater when the WP tunnels through the tube as compared to the case of tunneling directly into the support. The quantum particle spends more time in the tube region than in the forbidden region in this case.

4.2 Point contacts

A CNT is not an integral part of its support; the consequences of this can not be neglected in the interpretation of STM data [73]. When placed on HOPG, passivated Si, or other substrate, the CNT will "float" on the van der Waals potential [87]. The interlayer spacing of graphene sheets in HOPG and the distance of SWNTs in bundles are roughly similar, 0.34 nm, therefore it is justified to expect the same distance between the CNT and the HOPG substrate, or other, underlying NTs. During STM measurements, when the STM tip scans across the NT, depending on the value of the tunneling current flowing through the substrate-NT-tip system as compared with the direct tunneling (in the absence of the NT), the tip comes closer to the NT than the usual tunneling gap. The actual tube-tip distance can be estimated from the lateral distortion [75] of the atomic corrugation of the NT.

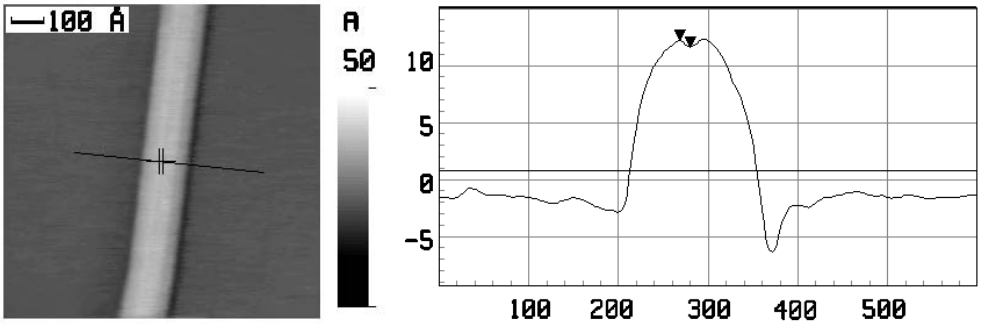

Figure 4.9: Constant current topographic STM image of a MWNT on HOPG, $I_t = 1.02$ nA, $U_g = 100$ mV. The line cut shown runs along the black line in the image, the two crosses label the positions of the markers shown in the line cut. From [74].

The tip may even come into mechanical contact with the CNT, as seen in *Fig. 4.9*, where the depression in the topmost part of the cross section through the NT clearly shows the deformation of the NT by the STM tip. The contact resistance measured at the Au/CNTs interface when no special treatment is done is of the order of $10 M\Omega$ [120], i.e., of similar magnitude as the resistance of the tunneling gap between HOPG and a Pt tip. This resistance may drop to $k\Omega$, if e-beam is used to modify the contact [120]. This suggests transition from tunneling to contact regime. During the compression of the NT by the STM tip similar phenomena may occur, the tunneling contact of the free tube may switch to (point)contact. It is reasonable to admit that in this case there are two simultaneous point contacts due to the fact that the STM tip is pressing the NT towards the support.

To explore the effect of point contacts on the STM tunneling phenomenon I performed detailed calculations [74] for the angle-, energy- and polarity dependence of the WP transmission probabilities. I have analyzed the following systems:

- an empty STM junction,

- one nanotube in the STM junction, and
- a nanotube raft.
- Effect of point contacts were investigated for a tip-tube and a tube-support point contact.

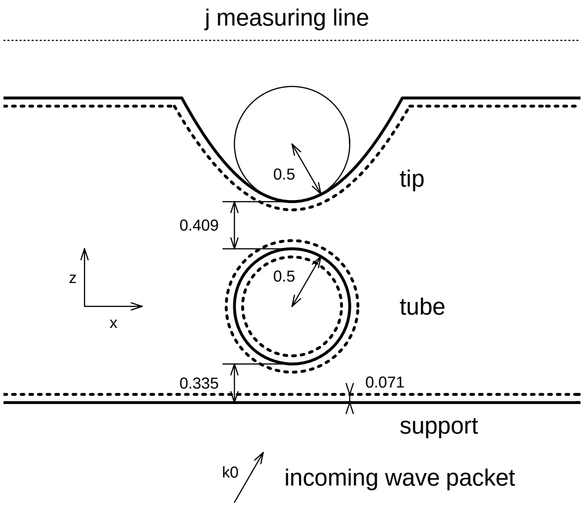

Figure 4.10: Model system. The lower half plane, middle ring and the hyperbolic protrusion on the upper half plane show the vertical cross sections of the support, nanotube, and tip, respectively. The effective surface (broken line) is 0.071 nm outside of the geometric surface (full line). The arrow labeled by k_0 shows the incidence direction of the incoming wave packet. $\vec{j}_{prob}$ is measured along the dotted line in the tip bulk. The particular wave packet and measuring line position is for a tip positive situation. In tip negative case the wave packet is approaching the tunnel junction from the tip bulk and $\vec{j}_{prob}$ is measured in the support bulk. All dimensions are in nm. From [74].

WP tunneling probabilities were calculated for a 2D jellium potential. *Fig. 4.10* shows the geometry of the model system. I used the same model parameters as described in Section 4.1.1 and 4.1.3. The tip-NT and NT-support point contacts when considered are represented by 0.2 nm wide conducting channels. Because of the large lateral size of the raft I used a truncated plain wave initial WP (see Section 3.3.2).

4.2.1 Angle dependent transmission for zero bias

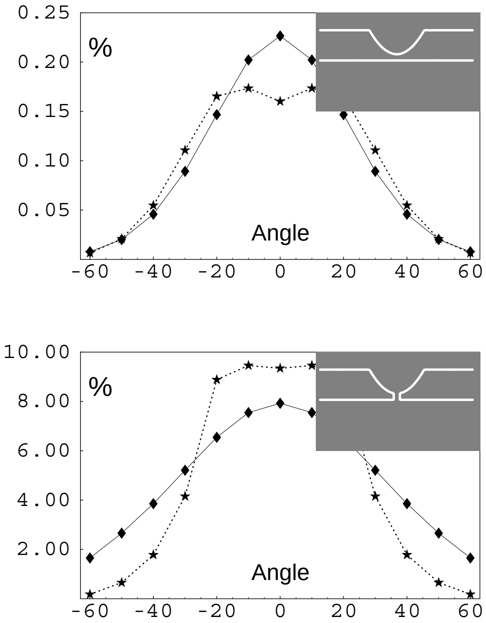

Figure 4.11: Transmission probability for the *a)* STM tunnel junction with no nanotube present and *b)* the same STM junction shortcutted by a point contact. Full (broken) line is for tip positive (negative) case. Model barrier geometry (effective surfaces) is shown in the inset. Note that the vertical scale of the two graphs is different by a factor of 40. From [74].

Fig. 4.11 shows angular dependent transmission probabilities $P(\theta)$ as the function of the incidence angle θ which is defined as the angle of the wave vector $\vec{k}_0 = (k_{x0}, k_{z0})$ of the incoming WP measured relative to the normal direction (”z”, see *Fig. 4.10*). For each model barrier the angular dependent transmission was calculated for WPs incident from the support ($P_+(\theta)$, tip positive, solid curves) and for those incident from the tip ($P_-(\theta)$, tip negative, dashed curves). For these vanishingly small bias calculations the incident WP energy was fixed to $E = E_F = 5$ eV. To check the consistency of the results the angular integral of the transmission probability was calculated for each curve. The integral values for tip positive and tip negative infinitesimal biases were found to agree within 5 percent, as they should. Because the $P(\theta)$ curves were calculated for only 13 equidistant angle values, we should not expect a better consistency.

4.2.2 Tunneling vs. point contact

Fig. 4.11(a) shows the $P_+^{tunnel}(\theta)$ and $P_-^{tunnel}(\theta)$ functions for an STM tunnel junction with no CNT present. $P_+^{tunnel}(\theta)$ will be my reference curve in the following discussion.

As we will see in Section 4.2.4, this curve is very similar to the angular dependence of the tunneling probability for a plane-plane barrier. For increasing angle the tunneling probability is decreasing because of the decreasing normal momentum of the WP. By contrast $P_{-}^{tunnel}(\theta)$ shows a plateau with a shallow minimum around normal incidence. This plateau is caused by the curls of the probability current density for waves incident from the bulk of the tip [121, 122]. According to stationary scattering theory calculations [122] (see *Fig. 4.12*), the wave reflected from the curved surface of the tip interferes with the incoming wave and thus loops appear in the probability current on the side of the barrier. These curls also strongly influence the probability density. *Fig. 4.13* shows the time averaged probability density for a WP coming from the tip. Dark spots in the tip apex region show places where the quasiparticle is found with largest probability which corresponds to places of large dwell time density (see Section 3.3.3).

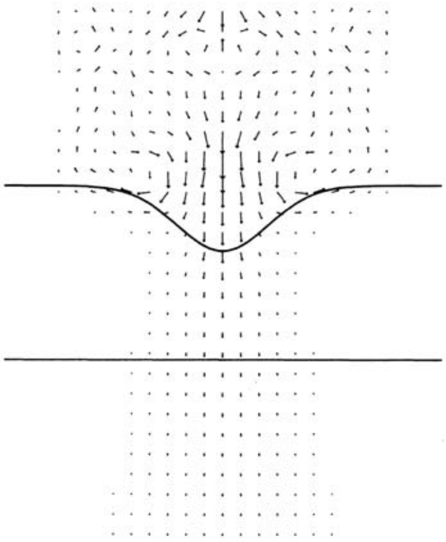

Figure 4.12: Map of the probability current density between a Gaussian shape tip with a 0.3 nm height and a 0.2 nm standard deviation and a flat sample located 0.5 nm from the tip. The applied bias is 10 mV, the inner potentials are 14 eV below the vacuum level, and the work functions are 4.5 eV. Ref. [122].

Fig. 4.11(b) shows the influence of a point contact (0.2 nm wide conducting channel) which connects the tip apex to the support. The most obvious effect is the increase of the transmission probability by a factor of about 40. The $P_{+}(\theta)$ angular dependence is also modified. This is the consequence of switching from tunneling to ballistic flow through the narrow conducting channel. The angular dependence of $P_{-}^{pointcontact}(\theta)$, however, is very similar to the tunneling case apart from the overall increased magnitude. There is a drop of the transmission probability at around 25° which can be attributed to the narrow aperture angle of the tip. This is simply because WPs incident at large angles from the tip bulk can not enter the apex. This wave guide effect can be even more pronounced in real experimental situations where the end of the tip has a needle like shape in nm scale. The functional form of the

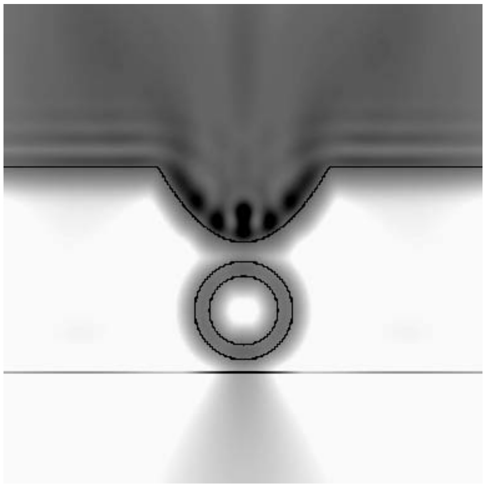

Figure 4.13: Influence of probability current curls inside the tip bulk on the time averaged probability density. The solid dark line shows the effective surfaces of the objects. Width of the presentation window is 5.76 nm. Darker grey shades correspond to larger probability density. A nonlinear grey scale was chosen to facilitate clearer presentation of both the curls inside the tip (high probability places) and the small density in the support region due to the tunneled-through part of the wave packet. From [74].

plateau in $P_-^{pointcontact}(\theta)$ is still influenced by the probability curls inside the tip apex. For small θ values $P_-^{pointcontact} > P_+^{pointcontact}$ because the tip apex collects the probability waves like a funnel. In the tunneling case this effect is suppressed because these collected waves have a wide angular distribution due to the multiple internal reflections inside the tip apex and the tunnel effect strongly selects only the normal momentum components as contrast to the point contact where no such self-selection occurs (Cf. the $P_+(\theta)$ curves for the two cases).

4.2.3 Nanotubes in the tunnel gap

In *Fig. 4.14* angular resolved transmission probabilities are shown for one CNT (left graphs) and a CNT raft (right graphs) placed in the STM gap. The raft is modeled by three tubes. In the upper row there is no point contact, in the middle row there is a point contact between the tip and the tube(s), and the lower row shows a situation with point contacts between both the tip and tube(s), and between the tube(s) and its (their) support.

The main functional form of the tip negative curves, $P_-(\theta)$ is similar in each case. This is so because P_- is mainly determined by the details of the tip apex shape. I have also performed calculations for a point contact only between the tube(s) and the support, a situation not likely to be found experimentally but needed in separating the effects in the case of two point contacts. These results are not shown here because it was found that the shape of $P_+(\theta)$ is similar to the two point contact case and only the absolute magnitude is smaller.

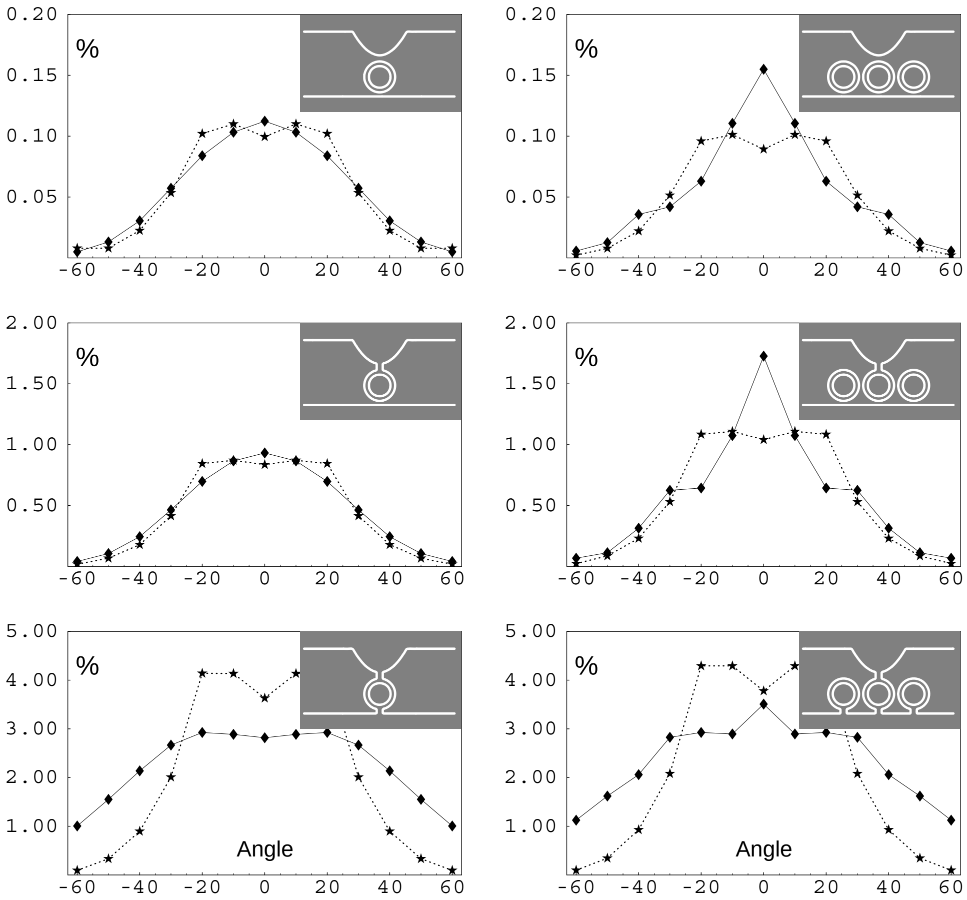

Figure 4.14: Transmission probabilities for different number of nanotubes and different point contact configurations. Full (broken) line is for tip positive (negative) case. Model barrier geometries (effective surfaces) are shown in the insets. Note the different vertical scale of the graphs facilitating clearer presentation. From [74].

The functional forms of the upper (no point contact) and middle (tip-tube point contact) tip positive P_+ graphs are also similar apart from a multiplicative factor. This is because the WP travels through two constrictions and the angular dependence of the transmission is mainly determined by the first gap it passes through. Indeed, the CNT which the WP propagates through widens the angular wave vector distribution of the WP. We can say that the wave barely remembers its original incidence angle by the time it reaches the second junction. This reasoning explains why the point contact specific angular dependence (see Section 4.2.2) shows up only in case of tube(s)-support point contact but not for the tip-tube(s) point contact where a tunneling specific angular dependence remains in spite of that one of the constrictions is an actual point contact.

The $P_+(\theta)$ functions for the raft model (*Fig. 4.14* right panels) have a diffraction grating like characteristic shape for all point contact arrangements. We can observe a strong peak around the normal incidence and smaller shoulders around $30 - 40°$. This diffraction grating like behavior is caused by the interference between the resonant states on the individual tubes. In the real 3D case this behavior is probably less significant for metallic CNTs than for semiconducting CNTs because the charge can spread along the metallic CNT easily and it reduces the resonant character of the states on the CNT.

4.2.4 Effective tunnel distances

To gain better insight into the results presented in the previous subsections it is instructive to compare my 2D transmission probabilities with those for a simple plane-plane (1D) case. With the help of the plane-plane model an *effective tunnel distance* d_{eff} will be defined.

The plane-plane tunneling can be solved as a 1D problem [109]. The tunneling probability for a 1D WP with $k_0 > 0$ is

$$P_{1D} = \int_0^\infty |\varphi_0(k, k_0, a)T(k)|^2 dk \tag{4.2}$$

where k_0 and a are the mean wave number and width of the initial WP, $\varphi_0(k, k_0, a)$ is the momentum representation of the initial WP and $T(k)$ is the transmission coefficient of the 1D barrier. A step potential (see Section 3.2) is defined by its height V_0 and width d. This means that P_{1D} is uniquely characterized by the variable set $\{k_0, a, V_0, d\}$ for this type of barrier.

If the WP is incident on a plane-plane barrier not from the normal but from an oblique direction then its transmission probability is determined by the normal component k_{z0} of its wave vector $\vec{k}_0 = (k_{x0}, k_{z0}) = (k_0 \sin\theta,\ k_0 \cos\theta)$. Due to the constant potential in the region where the WP is launched from, we may write the translational kinetic energy of the WP as

$$E_0 = |\vec{k}_0|^2/2 = k_{x0}^2/2 + k_{z0}^2/2. \tag{4.3}$$

So we can define its transversal and normal translational kinetic energy components by

$$E_0 = E_{x0} + E_{z0} = E_0 \sin^2\theta + E_0 \cos^2\theta. \tag{4.4}$$

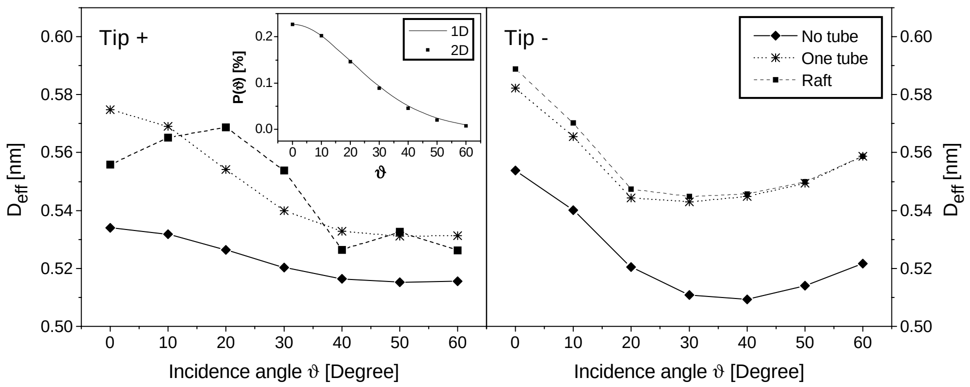

Figure 4.15: Effective tunnel distances for different number of nanotubes and for *a)* tip positive and *b)* tip negative case. Inset: the points are the calculated $P_+(\theta)$ values for different angles (same curve as on *Fig. 4.11(a)*). The solid line is the transmission for a wave packet incident from the *normal direction* with $E_0 = 5\cos^2\theta$ [eV] energy. See the text for details. From [74].

The transmission probability of the plane-plane barrier depends only on the E_{z0} normal energy component of the WP:

$$P_{plane-plane}(E_0, \theta, a, V_0, d) = P_{1D}(E_{z0}, a, V_0, d). \tag{4.5}$$

Using this formulation we can associate with any transmission function $P_{2D}(E_0, \theta)$ a (generally energy and angle dependent) effective tunnel distance $d_{eff}(E_0, \theta)$ by the equation

$$P_{2D}(E_0, \theta) = P_{1D}(E_0 \cos^2\theta, a, V_0, d_{eff}). \tag{4.6}$$

Fig. 4.15 shows the $d_{eff}(\theta)$ functions for different STM situations. d_{eff} is nearly a constant 0.52 nm for the STM tunnel junction with no CNT present (solid line) at an infinitesimal tip positive bias. This tells us that the barrier consisting of a plane and a hyperbolic tip with 0.5 nm radius at 0.409 nm distance is approximately equivalent for WPs defined in Section 3.3.2 to a plane-plane barrier with $d_{eff} = 0.52$ nm spacing. This constant value of the effective tunnel distance is a justification of using a 1D model for describing the operation of the STM in front of a flat surface. The reason behind this is the negligible mixing of the normal and transversal momentum components.

This separability of the momentum components is further demonstrated in the inset of *Fig. 4.15.* The points are the calculated $P_+(\theta)$ values for different angles (same curve as on *Fig. 4.11(a).* The solid line is the transmission for a WP incident from the *normal direction* with $E_0 = 5\cos^2\theta$ [eV] energy. The good match of these two curves shows that tunneling through this barrier is only negligibly influenced by the transversal momentum.

All other d_{eff} curves of *Fig. 4.15* show a considerable angle dependence which is the effect of the larger normal - transversal momentum mixing. In case of the $P_-(\theta)$ curves this mixing is largely dominated by the curls inside the tip apex. Hence functional forms of $P_-(\theta)$ curves are very similar to each other independently of the presence and number of CNTs in the junction. The presence of CNT(s) only introduce a constant shift in d_{eff} by about 0.027 nm although the tip-support distance is increased by 1.335 nm by inserting the CNTs.

For tip positive infinitesimal bias, however, the transmission of the raft is markedly different from that of the single tube: the diffraction grating like behavior which was already discussed in Section 4.2.3 is clearly visible.

4.2.5 Tunneling with non vanishing bias

To model the non vanishing bias an electrostatic potential calculated by the capacitance matrix method (see Section 3.2.1 and Appendix A) was added to the jellium potential. The sign of the potential was always set in agreement with the WP incidence direction, i.e. the WP was always launched opposite to the electric field, $\vec{E} \cdot \vec{k}_0 < 0$. For a positive (negative) tip the WP was always launched from the support (tip). Thus different potentials are seen by the WPs coming from the two directions, hence the angular integrals of $P_+(\theta)$ and $P_-(\theta)$ need no longer be equal and this causes an asymmetry in the calculated $I(V)$ curves.

4.2.6 Energy dependence of transmission

Fig. 4.16 shows the incidence energy dependence of the transmission probability of WPs with normal incidence through an STM tunnel junction with no CNT present and through a CNT for tip positive and tip negative 1 V biases. The zero of the energy scale is always fixed at the bottom band of the *launching side* of the WP. On this energy scale always the states between $E = 4$ eV and $E = 5$ eV (shaded region on the figure) contribute to the tunnel current at zero temperature.

The transmission for the STM tunnel junction with no CNT present follows an exponential like energy dependence characteristic of plane - plane tunneling (see Section 4.2.4). The presence of CNT, however, causes a plateau to appear between 3.8 and 5 eV. This plateau is a sign of resonant tunneling caused by the two tunnel interfaces [73]. The plateau is caused by

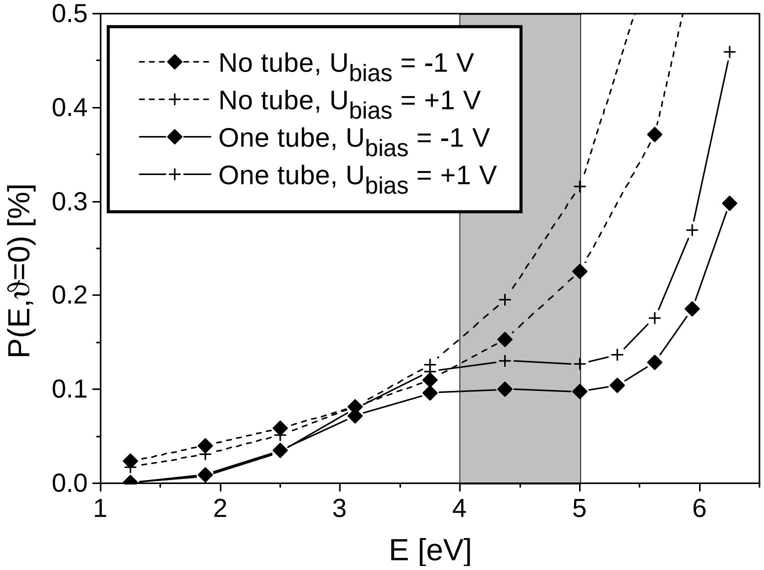

Figure 4.16: Energy dependent transmission of a wave packet incident from the normal direction for tip positive and tip negative 1 V bias potential. Full (broken) lines are for one (zero) nanotube. The zero of the energy scale is always fixed to the band bottom of the *launching side* of the wave packet. On this energy scale always the states between $E = 4$ eV and $E = 5$ eV (shaded region on the figure) contribute to the tunnel current at zero temperature. From [74].

quasibound states (see Section 5.3.1) of the tube which are in this energy region.

4.2.7 Tunnel current calculation

To estimate the tunnel current flowing through the real 3D junction we have to make some assumptions about the behavior of the system in the direction perpendicular (y direction) to my 2D calculation plane (xz plane). To this end, I have used the following simple approximations.

- The y diameter of the tunneling channel at the tip apex is assumed to be a constant 0.2 nm.

- The transmission is assumed to depend on the in-plane and perpendicular-to-the-plane angles independently and

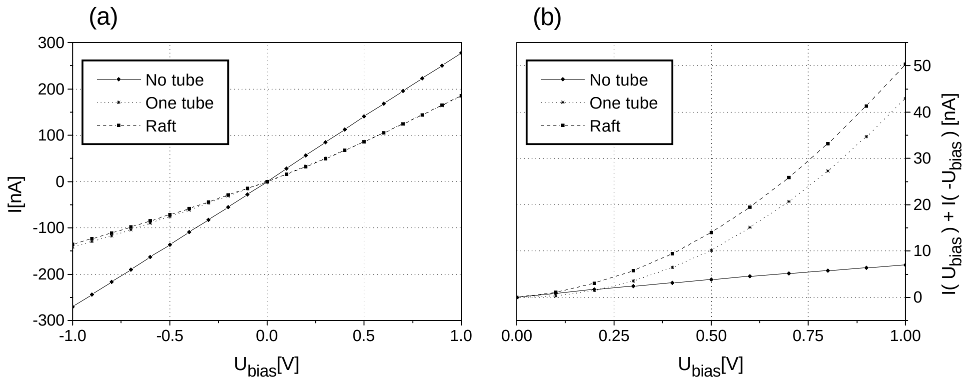

Figure 4.17: *a)* Tunnel current as function of applied bias for an STM tunnel junction with no nanotube present, for one nanotube, and for a nanotube raft. *b)* Tunnel current asymmetries for the curves in Fig. *(a)*. From [74].

- the perpendicular-to-the-plane angle dependence is taken to be the same as of a plane-plane system (see Section 4.2.4).

After calculating the total 3D $P(U_t, \vec{k})$ transmission probability in the above approximation the tunnel current is

$$I(U_t) = \frac{1}{4\pi^3} A_{WP}^{eff} \int_{\text{allowed}} P\left(U_t, \vec{k}\right) k_z d\vec{k} \tag{4.7}$$

where A_{WP}^{eff} is the effective lateral (xy) area of the WP defined as

$$A_{WP}^{eff} = \frac{1}{\left(\int_{-\infty}^{+\infty} \rho_{WP}\left(x_0, z, t=0\right) dz\right)^2} \tag{4.8}$$

and x_0 is the initial x position of the center of the WP.

Assuming a free electron like $E(\vec{k})$ relation and DOS, the allowed $\vec{k}$ space region is the region between the $E = E_F$ and $E = E_F - U_t$ hemispheres. $I(U_t)$ curves for the STM tunnel junction with no CNT present, for one CNT, and for three CNTs are shown in *Fig. 4.17(a)*.

The absolute value of the calculated current is higher than those measured in typical STS experiments. This is partly an artefact of the WP dynamical method attributed to the amplification effect [123] of the higher momentum components in the tunneling process. Further, experimental aspects of this higher than usual tunnel current are given in Section 4.3 below.

4.3 Tip polarity

All $I(U_t)$ curves of *Fig. 4.17(a)* show some degree of asymmetry. These asymmetries are better displayed in the $I(U_t)+I(-U_t)$ graphs of *Fig. 4.17(b)*. Note that while the asymmetry of the STM tunnel junction with no CNT present shows a linear U_t dependence and its magnitude is only 2.5%, the asymmetry of the tunnel gaps with CNTs are increasing with U_t and reach a value of more than 20% at 1 V bias. It should be emphasized that these asymmetries are of pure geometrical origin because of the free electron like DOS assumption.

The experimental STS curves [10, 11, 124, 84, 125] of CNTs frequently show some degree of asymmetry with respect to bias voltage polarity. In some cases this asymmetry was attributed to charge transfer between the Au substrate and the CNT [10]. Asymmetry was observed in STS measurements of CNTs on HOPG [124, 125], too, where charge transfer should be very limited. According to the simulation results presented above, two possible reasons which could lead to asymmetry in the STS data are as follows:

- effects arising from the particular tip geometry,
- effects arising from point contact during imaging and/or during STS measurements.

The very end of an STM tip may have a shape that deviates drastically from the idealized geometry used in my model. However, a more complex tip may be generated by considering the tip as being composed of several idealized tips. This kind of approach was used earlier for analyzing multiple tip effects [126, 127] in atomic resolution STM images. In the framework of my model it follows from this approach that the particular tip shape will influence the structure of the curls produced in the tip and by this can modify the particular shape of the $P_{-}(\theta)$ function. This kind of effect is expected to influence the negative side of the STS curve when positive polarity means tunneling from sample to tip. Due to the fact that the tip acts like a "wave-guide", the width/length ratio of the active microtip, i.e., of the tip which is really responsible for the tunneling may also have a role in deciding the characteristic vortex structure.

The second kind of asymmetry source is the point contact between the CNT and its support; in fact this means that there are two point contacts: one at the STM tip/CNT interface – this will influence the magnitude of the tunneling current – and the second one at the CNT/support interface. This later one is produced by pressure exerted by the STM tip on the top of the CNT. Theoretical arguments point into the direction that differences in the electronic structure of the CNT and of the metal which is within tunneling distance, may introduce an additional energy barrier of 10 eV [128]. This may lead to the reduction of the tunneling gap over the CNT and to compression of the CNT between the STM tip and the support. The second point contact (CNT/support) will introduce the asymmetry in the STS spectra. In this case unusual features are expected on the positive side of the STS spectrum when tunneling takes place from sample to tip, while the negative side will not differ in shape from symmetric spectra but the magnitude of the tunneling current will increase significantly.

These expectations are fulfilled by the experimental data reported by L. P. Biró et al [125]. This second kind of asymmetry is expected to show up in those STS measurements for which larger tunneling current values were used during establishing the position of the STM tip before the feedback loop is switched off. If the transmission through the system STM tip/CNT/support is low, then during the constant current imaging operation (when the width of the tunneling gap used during the STS measurement is determined, too) the tip can come into mechanical contact with the topmost part of the CNT. When this occurs, the topographic image will not be drastically altered. The compression effects may be visible in transversal line cuts taken across the CNT like the one shown in *Fig. 4.9*. Although it may affect the image quality, the point contact will not impede achieving atomic resolution imaging, like in 2.7, taken at a slightly smaller tunneling current as compared with *Fig. 4.9*. This is in agreement with earlier point contact atomic resolution achieved on HOPG [26].

These findings show that it is strongly recommended that topographic STM images and STS curves be accompanied by line-cuts taken across the investigated CNT.

Frequently, current imaging tunneling spectroscopy (CITS) is used to acquire spectroscopic data in several or every pixel point which compose an STM image. When performing CITS the feedback loop is switched on and off for every pixel, but again, the value of the STM gap is selected during the acquisition of the topographic information. It may happen that for different points of the image the width of the tunneling gap will be different, like in the case of rafts of CNTs [125]. If this happens symmetric and asymmetric STS curves may be measured over the same CNT. Beyond the effects arising from point contact, it follows from *Fig. 4.15* that the particular arrangement of the CNTs in a raft or a bundle will have its fingerprint on the shape of the STS curves.

As we noticed in Section 4.2.7, the absolute values of our calculated currents are higher than those in STS measurements. In STM experiments the tunneling gap is determined in topographic mode. This means that the 1 nA current is expected at say 0.1 V bias at gap of 0.4 nm. Now, when U_t is increased without modifying the gap value – which does not happen during normal, topographic imaging, because the feedback loop would correct it automatically – it results a strong increase of the tunneling current. This is the reason, why when doing spectroscopy, one has to choose a "starting gap" large enough that at the edges of the voltage range the allowable current limit of the electronics are not exceeded. Furthermore, if a certain energy density is exceeded in the tunneling channel, then permanent modifications may happen in the sample and/or tip structure, which will alter the shape of the spectroscopic curve.

4.4 Summary

In this chapter I have identified and investigated in detail the geometrical factors influencing the STM image and STS spectrum of carbon NTs and NT rafts.

- Most important geometrical factor is the shape of the apex of the STM tip. Since the radius of curvature of the tip apex is comparable on one hand with the radius of SWNTs and with the size of the tunneling gap on the other, the lateral size of the NT is much larger than its height in STM images. I developed a simple geometrical model to account for these factors and verified the findings with WPD calculations. As long as the electronic structure of the NT and of its support is similar, the major distortion arises from the geometric convolution. This is found experimentally in the case of NTs placed on the top of rafts of similar NTs. When the electronic structure of the support is different from that of the NT, i. e., when HOPG, gold, or other support is used, further distortions arise from the modification of the width of the tunnel gap over the NT if compared to the value found over the support.

- I have calculated incidence angle and energy dependent WP transmission coefficients through the STM junction model containing various configurations of CNTs and point contacts. From the 2D scattering calculated from the time dependent Schrödinger equation 3D transmission coefficients are derived by assuming no mixing of the WP momentum components along the tube axis and perpendicular to the tube axis. The total tunnel current at a given bias is calculated by the statistical average of probability currents for all WPs assuming a free electron dispersion relation.

It was found that for tip negative bias (WP approaching the tunnel junction from the tip) the angular dependence of the transmission is mainly determined by the tip shape. The particular tip shape determines the probability current curls inside the tip and this effect introduces an asymmetry on the negative side of the STS spectrum.

For tip positive bias (WP approaching the tunnel junction from the support), however, the angular dependence of the transmission depends strongly on the nature of the nanosystem placed into the STM gap. The tip positive transmission of an STM tunnel junction with no NT present can be well represented by a plane-plane model while all other configurations studied show a considerable amount of normal-transversal momentum mixing. The angular dependence of the transmission of the NT raft shows a diffraction grating like behavior.

- Point contacts between the NT and its support caused by mechanical pressure exerted by the STM tip cause an asymmetry to appear in the positive side of the STS spectrum.

- While for an STM tunnel junction with no NT present the calculated STS spectrum shows only a small, and linear in U_t asymmetry, for NTs there is a considerable degree of asymmetry present in the $I(V)$ curves. Because of the free electron DOS assumption these asymmetries are of purely geometrical origin.

Chapter 5

3D simulation of the STM tunneling process

Recent advances in computer power permitted me to perform three dimensional (3D) WPD calculations on the NT-in-STM system within the framework of the jellium model. A detailed analysis of the distribution of the probability current and of the probability density is given in this Chapter.

Four systems were investigated:

- an infinite SWNT on an atomically flat support as reference case,
- a capped SWNT protruding a step of the support surface,
- a quantum dot (short finite tube), and
- a SWNT Y-junction.

WPD calculations on the 2D jellium model (see Chapter 4) were successful in explaining several factors of geometrical origin influencing the STM images of carbon nanosystems. These include the tip caused apparent broadening, and the displacement of the tunneling point on the surface of the tip during scanning of the CNT which causes an apparent asymmetric distortion [75] of the atomic lattice. STS spectra were also computed [74] by the same technique. The calculations revealed asymmetric I-V curves — found frequently in STS experiments [124] even when using HOPG substrate — of pure geometrical origin. The asymmetry was found [74] to depend on the nature of the contact between the tip and the CNT. There is a greater asymmetry if this contact is not a tunneling contact but an electronic point contact [26], as the result of a mechanical deformation of the NT exerted by the STM tip – as is often the case in experiments [74].

The main new phenomenon in 3D calculations is the axial spreading of the WP along the CNT during tunneling. This WP spreading is caused by the different dimensionality of the two tunnel junctions. Indeed, the tip – CNT tunnel junction is zero dimensional but the CNT – support tunnel junction is one dimensional. After the WP goes through the narrow tip – CNT tunnel junction, its lateral "size" is small, around 0.1 nm (see Section 5.2) This spatial confinement of the WP causes a spreading along the tube axis. By calculating the WP spreading during tunneling we can calculate how far the influence of a local perturbation (e.g. the different electronic structure of the center of the Y-junction) is extended along the NT. Recent advances in computer power permit us to address the full 3D geometry of the problem and thus to handle the WP spreading phenomenon. This kind of calculation is exposed in the present Chapter.

5.1 Model systems

The four model systems are shown in *Fig. 5.5*, *Fig. 5.9*, and *Fig. 5.23.* The geometrical and material parameters of the CNT, the tip, and the support are the same as described in Section 3.2 and applied also in 2D calculations of Chapter 4.

The STM bias is chosen to be zero throughout this Chapter, because the computationally intensive 3D calculations did not permit to repeat the calculation many times what would be necessary to calculate momentum space integrals as was done for the 2D case in Chapter 4. The vanishingly small bias approximation is, however, suitable for small bias experiments, or when the imaging process is not bias dependent.

The high aspect ratio of the NT made it necessary to calculate for a long cuboid (rectangular box). The axial (longitudinal) length of this cuboid was chosen in such a way that the majority of the tunnel current flows from the tube into the support surface within this length. The calculation- and presentation boxes (see Section 3.2.2) are shown in *Fig. 5.1* and *Fig. 5.2*

Fig. 5.2 shows the calculation box and the absorbing potential (see Section 3.2.2). The total complex potential (real part: jellium potential, imaginary part: absorbing potential) is shown by color coding. Because the y (axial) length of the calculation box is longer than the x and z length, the absorbing region is cylindrical closed by two hemispheres.

After the WP has tunneled into the NT, it partly tunnels into the support within the -7.68 nm $< y <$ 7.68 nm axial interval of the presentation box and partly flows outside the box at the tube end(s), see *Fig. 5.3.* (As shown later (Section 5.5), the probability of tunneling back from the NT to the tip

Figure 5.1: (color) *(left)* Presentation box used in the 3D calculation with the STM tip, nanotube, and support. *(right)* yz and xz cross sections of the 3D jellium potential. All dimensions are in nm. Axial length of the presentation box is 15.36 nm.

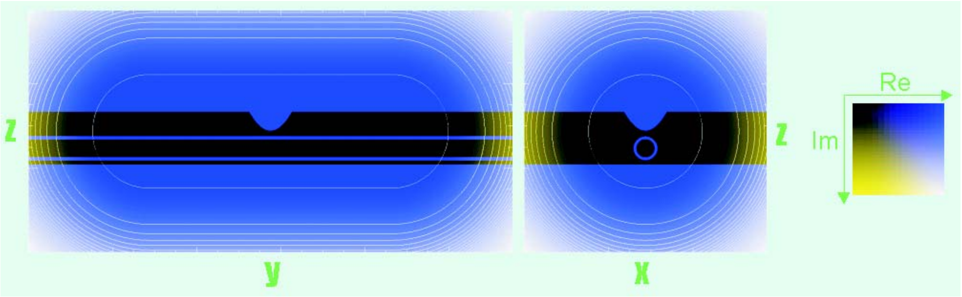

Figure 5.2: (color) yz and xz cross sections of the 3D potential in the calculation box. Blue color shows the jellium potential (real part), yellow shows the absorbing potential (imaginary part). Axial length of the calculation box is 23.04 nm.

is negligible.) These $I_{tubeend}$ current components, however, would eventually also tunnel into the support surface when the axial length of the presentation box went to infinity (see Section 5.6).

An infinite tube on a flat support is our reference system.

For the case of the capped NT hanging outside a step an 1 nm high step is considered with a hemisphere-capped cylinder protruding to a length of 3 nm. The STM tip is displaced 1.8 nm along the tube from the step edge above the lower terrace.

To identify the contributions of the tip – NT and NT – support tunnel junctions, a special, hypothetical ”quantum dot” system was also considered: a 5.1 nm long tube closed at both ends. This system is hypothetical because the nanostructure is free standing, i.e. it has no support surface in this model.

The Y-junction is modeled by joining symmetrically three 1 nm diameter semi-infinite cylinders. Two tip positions were analyzed: the tip is either

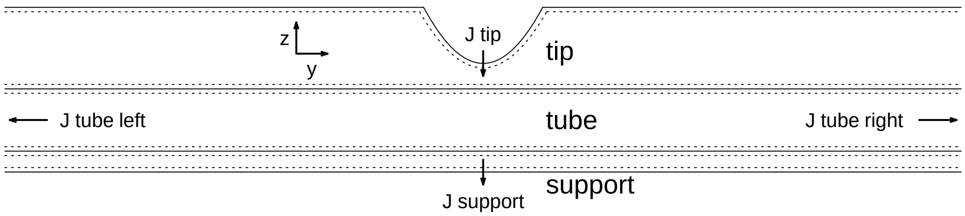

Figure 5.3: Probability currents analyzed in this Chapter are shown by arrows. Cross section of the geometric (effective) surface of the STM tip, nanotube, and support are shown by full (broken) line. From [129].

above the trigonal symmetry point or displaced 1.2 nm along one arm.

5.2 Calculation method

The calculation is done as described in Chapter 3. A Gaussian WP is launched with the Fermi momentum $\vec{k} = (0, 0, -k_F)$ from inside the tip bulk towards the apex of the tip. The real space width of the WP is chosen to be $\Delta x, y, z = 0.37$ nm which is significantly larger than the $\Delta x, y = 0.108$ nm value for the tip – sample tunneling channel obtained from my calculation (see Section 5.3).

The method of analyzing the resulting large four dimensional wave function dataset is described in Section 3.3.3.

First I calculated the probability density $\varrho(\vec{r}; t) = |\psi(x, y, z; t)|^2$ and the probability current density $\vec{j}(\vec{r}; t)$ from the time dependent wave function. Time evolution of $\varrho(\vec{r}; t)$ is shown by snapshots of an iso-density surface for two model geometries in *Fig. 5.5.* To analyze the probability density distribution along the NT, the 3D probability density is integrated on the tube cross section:

$$\varrho_{tube}(y; t) = \int_{tube} \varrho(x, y, z; t)\, dxdz \tag{5.1}$$

where $\int_{tube}$ means integrating between the effective surfaces of the tube. $\varrho_{tube}(y; t)$ axial probability density distributions are shown in *Fig. 5.6* by 2D filled-contour graphics. Integrating $\varrho_{tube}(y; t)$ again for the length of the tube gives the total probability $P_{tube}(t)$ of finding the electron on the tube as the function of time which is shown in *Fig. 5.7.*

Next I calculated the $j_{support}(x, y; t)$ probability current density flowing into the support surface and integrated it along the coordinate x perpen-

Table 5.1: Summary of observables calculated from $\psi(x, y, z; t)$.

Quantity	Definition	Explanation
$\varrho_{tube}(y; t)$	$\int_{tube} \varrho(x, y, z; t)\, dxdz$	Time dependent linear probability density on the tube
$P_{tube}(t)$	$\int_{y_{min}}^{y_{max}} \varrho_{tube}(y; t)\, dy$	Total probability on the tube as the function of time
$j_{support}(y; t)$	$\int j_{support}(x, y; t)\, dx$	Linear probability current density flowing into the support surface
$I_{support}(t)$	$\int j_{support}(x, y; t)\, dxdy$	Probability current flowing into the support
$T_{support}(y)$	$\int j_{support}(x, y; t)\, dxdt$	Total transmission into the dy slice below the tube

dicular to the NT, this gives the $j_{support}(y; t)$ function – the current density flowing into a dy slice on the support surface – shown in *Fig. 5.6.*

Integrating this quantity for the length of the tube gives the $I_{support}(t)$ total probability current flowing into the support at the given time and integrating from $t = 0$ to $t = \infty$ gives the $T_{support}(y)$ axial dependent transmission. In the same way the $I_{tubeend}(t)$ and $T_{tubeend}(y)$ as well as the $I_{tip}(t)$ and $T_{tip}(y)$ quantities are calculated, which are the current and transmission for a plane perpendicular to the tube at the end of the presentation box and for a plane below the tip apex. See *Fig. 5.3* for the definition of these current components.

Time development is followed until $P_{tube}(t)$ becomes negligibly small.

Table 5.1 gives a brief dictionary of the notation used throughout this Chapter.

5.3 Infinite tube on atomically flat support

Fig. 5.4 shows the initial stages of the time evolution of the probability density. I performed this calculation earlier [130] for a smaller calculation box (3.84 nm) and shorter time (4.2 fs).

- In the panel $t = 0.0$ fs of *Fig. 5.4* the initial WP is shown. It is a spherically symmetric Gaussian, hence the isodensity surface is a sphere. The sphere surface is clipped at the upper boundary of the presentation box.

- At $t = 1.4$ fs the WP has already penetrated into the tip apex region. The part reflected back into the tip bulk forms interference patterns

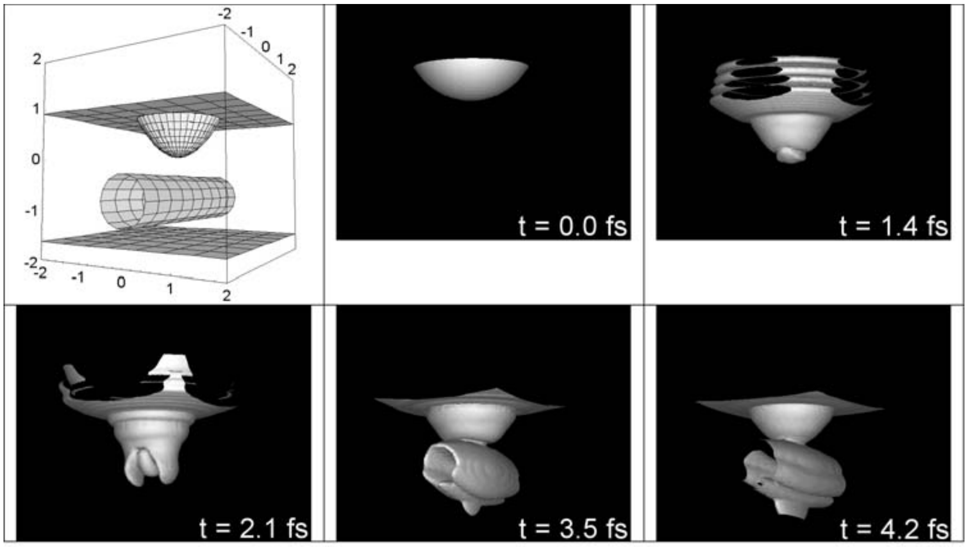

Figure 5.4: Time evolution of the probability density of the WP approaching the STM junction from the tip bulk and tunneling through the nanotube into the support. The upper left image is the model system used in the calculation. The labeled box is the presentation box. All dimensions are in nm. The subsequent images show snapshots of a constant probability density surface. This surface is clipped at the six faces of the presentation cube. From [130].

with the incoming wave. A fraction of the WP just begins to enter into the tip-CNT interface.

- At $t = 2.1$ fs the WP flows around the tube and simultaneously tunnels through it. The incoming and outgoing waves form interference patterns in the tip apex region. When the two WP parts (one moving on the left side and another on the right side of the tube) meet at the lowest point, standing wave patterns begin to form along the tube circumference.

- Subsequently the WP tunnels through the CNT-support junction and enters into the support surface (at $t = 3.5$ fs). In the meantime the probability density is gradually spreading along the tube axis.

- At $t = 4.2$ fs the CNT-support tunnel channel begins to open along the tube axis. The isosurface is clipped at the front- and rear faces of the presentation cube.

Later I had the possibility to extend the simulation [129] for a long enough time (150 fs) and large enough calculation box (15.36 nm) to study the complete dynamics of the process. This numerical work was done on the 180 GFlops SMP supercomputer of the Hungarian NIIF.

The left column of *Fig. 5.5* shows the geometry of the system and the time evolution of the $\varrho(\vec{r};t)$ probability density. The particular snapshot times were chosen according to the features of $j_{support}^{cappedtube}(y;t)$ shown in *Fig. 5.6(g)*, (see Section 5.4). Complete time evolution can be seen on the Web (`http://www.mfa.kfki.hu/int/nano/online/longspread2004/`) by computer animation.

- By $t = 2.54$ fs the middle part of the tube is already "charged", the WP flows around the tube. At this particular instant $\varrho_{tube}(y;t)$ is maximal, see *Fig. 5.6(a)*.
- After this time the majority of the WP is scattered back into the tip and the part remaining on the tube spreads along it and gradually tunnels into the support surface. The large part of the WP scattered back into the tip produces interference patterns with the incoming wave. These interference patterns are still visible in the tip bulk region until $t = 8.47$ fs, after that the backscattered WP part is travelling out of the presentation box and is absorbed in the drain potential bordering this box.
- As seen on the series of snapshots for $t = 6.05$ fs, $t = 8.47$ fs, and $t = 17.84$ fs the NT–support tunneling channel is gradually opening along the tube axis as the WP is spreading along the tube. This channel is not any more seen on the subsequent iso-surface snapshots because the overall probability density decreases as a consequence of the gradual flowing out of the WP from the presentation box. As a result of this decrease, the density in the tube-support junction becomes smaller than the density corresponding to the particular iso-surface. As discussed below, however, the tunnel current is still flowing for these times but with a decreasing intensity and in a channel with increasing width in the axial direction. It has to be mentioned, that in the case of a real tunneling experiment there is a continuous supply of electrons.

The long, axial structures seen from $t = 6.05$ fs in the iso-surfaces are standing wave patterns along the circumference of the tube. These are caused by the interference of different radial eigenstates of the tube (see Section 5.3.1). Because the tunneling coupling of the tube wave function with the tip and the support is relatively weak, one can consider that the system has

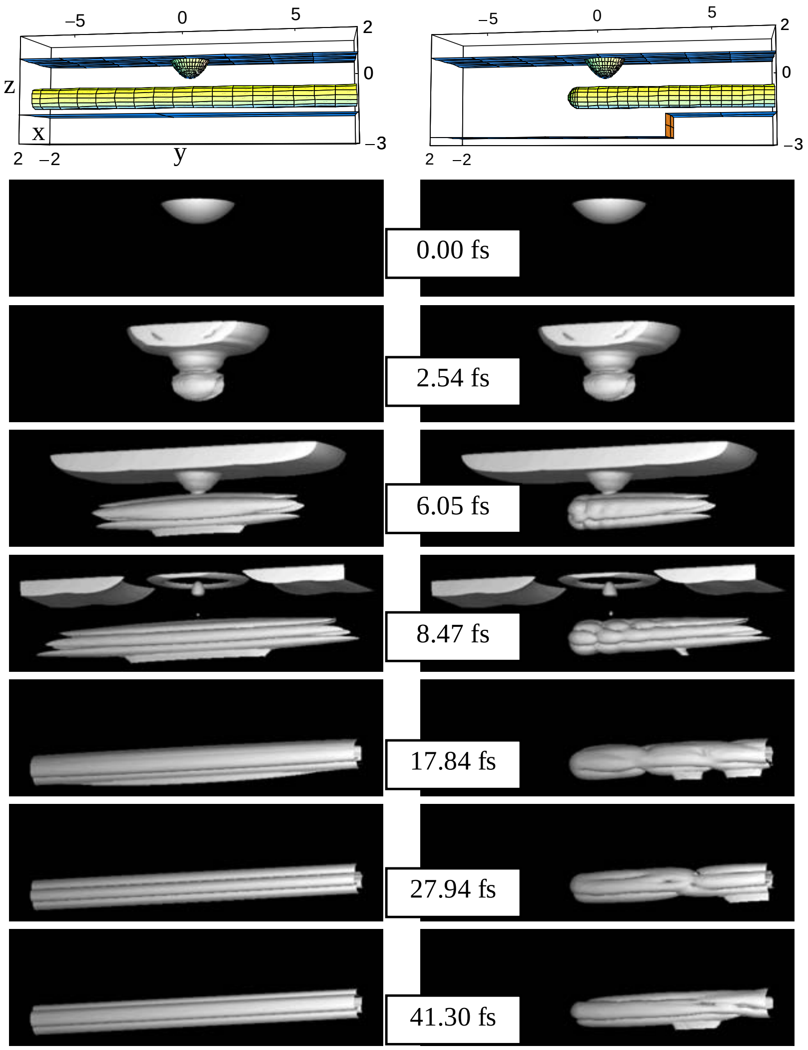

Figure 5.5: Time evolution of the probability density of the wave packet approaching the STM junction from the tip bulk and tunneling through the nanotube into the support. The left column is for the infinite tube on an atomically flat support and the right column is for the capped tube hanging above a step of the support surface. Geometries of the two systems are shown on the upper subimages. The cuboid shows the presentation box boundaries. All dimensions are in nm. The subsequent subimages show snapshots of an iso-density surface with density value of $\varrho(\vec{r};t) = \varrho_0 = 2.0245 \cdot 10^{-6}$ nm^{-3}. The iso-surfaces are clipped at the presentation box boundaries. From [129].

translational invariance along the y axis, hence the wave function of the tube can be approximated as (see Section 5.3.1)

$$\psi(\vec{r};t) \approx \psi_{freetube}(r,\varphi;t)\,\psi_{freetube}(y;t) \tag{5.2}$$

where y is the axial coordinate and r, φ are the radial coordinates in the cross sectional planes perpendicular to the tube axis. According to our recent calculations [131, 132], the energy of the first few radial eigenstates of a free standing jellium tube falls into the energy window of the incoming WP, hence $\psi(r,\varphi;t)$ is a superposition of these states. The time dependence of the phases of the superposition components yields the time dependent density waves around the tube seen in the iso-density surface plots.

Fig. 5.6(a) shows the time dependence of $\varrho(y;t)$, the probability density integrated over the cross section of the tube (cf. eq. (5.1)) as a spacetime density plot [133, 134] (a "quantum carpet"). White corresponds to zero density and black to $2.10 \cdot 10^{-3}$ nm^{-1} .

- For $t < 1.2$ fs there is only negligible probability on the tube because it takes a finite time for the WP to reach the tube region from its initial position in the tip bulk.
- When the WP reaches the tube, the central part (i.e. that below the tip) of the tube gets "charged" which is seen in *Fig. 5.6(a)* as a high intensity, narrow peak around $t = 2.54$ fs.
- After this time the WP is gradually spreading along the tube.

As seen in *Fig. 5.6(a)*, $\varrho(y;t)$ is a smooth function, because the oscillations along the tube circumference are integrated out. In the approximation of negligible coupling of the tube wave function with the tip and the support (cf. eq. (5.2)) $\varrho(y;t) \approx |\psi_{freetube}(y;t)|^2$. In this approximation the jellium potential seen by the WP does not depend on the y coordinate, hence the WP is spreading along the tube like in free space. The coupling of the tube wave function with the support, however, does cause a gradual tunneling of the WP into the support surface while it spreads along the tube.

As can be seen in *Fig. 5.6(a)*, the iso-density contours are linear for small t values. By calculating the tangent of the contour corresponding to the 3D density value $\varrho(\vec{r};t) = \varrho_0 = 2.0245 \cdot 10^{-6}$ nm^{-3}, i.e. those displayed in *Fig. 5.5* by the iso-surfaces, a spreading velocity of $v_{spread} = 1.04$ nm/fs is obtained which is close to the $v_F = 1.33$ nm/fs Fermi velocity calculated from $E_F = 5$ eV.

The $j_{support}(y;t)$ linear probability tunneling current density flowing into the support is shown in *Fig. 5.6(c)*. White corresponds to zero current and

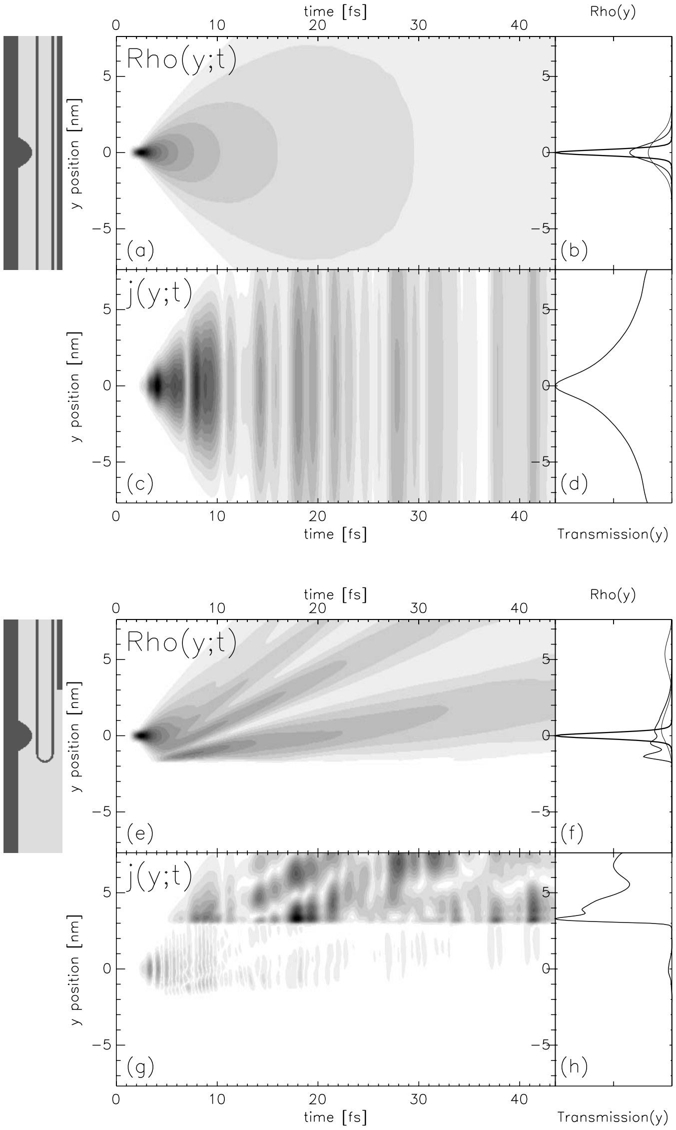

Figure 5.6: Analysis of the tunneling process as the function of time and the y position along the tube. (a-d) is for the infinite tube above an atomically flat support and (e-h) for the capped tube protruding a 1 nm high step. yz cross sections of the potential are shown on the left. (a) and (e) $\varrho(y;t)$ on the tube. (b) and (f) $\varrho(y;t)$ on the tube at $t = 2.54, 3.75, 4.96$ fs. (c) and (g) $\jmath(y;t)$ flowing into the support. (d) and (h) Transmission probability into the support. From [129].

black to $8.03 \cdot 10^{-6}$ nm^{-1} fs^{-1}. The onset of the tunnel current occurs around $t = 2.1$ fs, 0.9 fs later than that of $\varrho(y;t)$ because the WP has to flow around the circumference of the tube before it can tunnel into the support. The maximum of the tunnel current density (black dot) occurs at $t = 4.11$ fs.

The overall structure of $j_{support}(y;t)$ consists of an axial spreading and a temporal oscillation. The axial spreading of the current density is caused by the axial spreading of the WP along the tube. As seen in *Fig. 5.6(c)*, the $\varrho(y;t)$ and $j_{support}(y;t)$ functions spread with the same velocity and the axial shape of the linear current density is similar to the axial shape of the probability density along the tube. The temporal oscillation seen in $j_{support}(y;t)$ is, however, not present in $\varrho(y;t)$. This oscillation takes place because the tunneling current is determined by the density close to the "lowest" fiber of the tube (i.e. that closest to the support surface) and not by the overall density on the tube. Along a generator of the tube $\varrho(t)$ oscillates as a result of the interference between the azimuthal eigenstates discussed above.

Fig. 5.6(d) shows the y dependence of the $T_{support}(y) = \int_0^\infty j_{support}(y;t')\,dt'$ transmission function. (The integral of $j_{support}(y;t)$ over its other variable, y gives $I_{support}(t)$, which is discussed below.) $T_{support}(y)\,dy$ is the probability that the electron eventually tunnels into the dy wide slice of the support surface around y. As seen in *Fig. 5.6(d)* the largest tunneling probability is right below the tip and the tunneling probability is gradually decreasing along the tube axis, approximately like a Lorenzian. The total transmission into the support,

$$T_{support} = \int_{y_{min}}^{y_{max}} T_{support}(y)\,dy = \int_0^\infty T_{support}(t)\,dt \tag{5.3}$$

is $0.3271 \cdot 10^{-3}$ (see Table 5.2).

The half width at half maximum (HWHM) of the tube – support tunneling channel is 0.105 nm in the x direction and 2.37 nm in the y direction.

Fig. 5.7(a) is the comparison of the "probability charge" $P_{tube}(t)$ found on the tube at a given time with the $T_i(t)$ time-cumulated transmissions, i.e. those parts of the WP that went through the given measurement planes in the $[0,t]$ time interval, where i is the index of the measuring plane. The definition of these quantities is as follows

$$P_{tube}(t) = \int_{y_{min}}^{y_{max}} \varrho(y;t)\,dy \tag{5.4}$$

$$T_i(t) = \int_0^t I_i(t')\,dt'. \tag{5.5}$$

I have calculated the transmissions for four measuring planes, called "tip plane", "support plane", and "tube end planes (right or left)", which are the

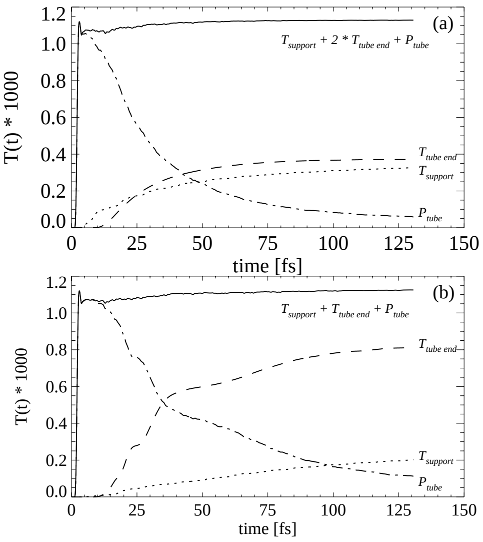

Figure 5.7: Time cumulated transmissions of the wave packet launched from the tip bulk into the support surface (dotted line) and through the tube cross section at the presentation box boundary (dashed line). The total probability of the wave packet at the tube is also shown as the function of time by a dash-dotted line. Net transmission from the tube plus the probability on the tube is shown by the continuous line. See the text for details. (a) Infinite tube above an atomically flat support. (b) Capped tube hanging above a step of the support. From [129].

Table 5.2: Wave packet transmissions (in 10^{-3}) through the different measuring planes defined in *Fig. 5.3* for the case of the simple tube above an atomically flat support and the capped tube protruding the step.

	Support	Tube right end	Total
Flat support	0.3271	0.3714	1.1287
Step	0.2017	0.8109	1.1252

planes below the tip apex (in the vacuum gap), below the support surface (inside the bulk), and perpendicular to the tube at the $y = y_{min}$ and $y = y_{max}$ ends of the presentation box, respectively. Thus $i\epsilon\{tip, support, tubeend\}$. As can be seen on the P_{tube} function of *Fig. 5.7(a)*, the tube is first quickly charged by the WP. The narrow peak around $t = 2.96$ fs shows that some of the WP is immediatelly reflected from the tube to the tip. The "probability charge" remaining on the tube is decreasing slowly in time. As shown by the full line in *Fig. 5.7(a)*, $T_{support}(t) + 2T_{tubeend}(t) + P_{tube}(t)$ has a constant, $1.1287{\cdot}10^{-3}$ value (see Table 5.2), which proves that the decrease of $P_{tube}(t)$ is caused by tunneling into the support surface and by direct flowout at the tube ends. As shown in Section 5.5, the tunnel resistance of the tip–NT interface is much higher than that of the NT–support interface, hence the contribution of tunneling back from the tube to the tip can be safely neglected here.

5.3.1 Stationary states of the jellium CNT

In this section I present analytical solutions for the stationary states of the jellium tube. This work [131, 132] was done together with Levente Tapasztó.

In order to calculate the analytical, stationary wave functions of a jellium CNT model, I solved the stationary Schrödinger equation for the one electron potential modeling a CNT with geometrical and material parameters chosen to be consistent with my WPD simulations. In the case of the freestanding NT, from symmetry considerations, it was feasible to write the Schrödinger equation in cylindrical coordinates, because the jellium potential of an infinite CNT depends only on the radial coordinate r:

$$V(r,\varphi,z) = V(r) = \frac{1}{2}\frac{m^2 - 1/4}{r^2} + \begin{cases} -9.81\,\text{eV} & r \in [r_{tube} - j, r_{tube} + j] \\ 0 & \text{othervise} \end{cases} \tag{5.6}$$

where m is the azimuthal quantum number (see below) and $j = 0.071$ nm is the jellium radius (see Section 3.2).

Because of translational symmetry along the axis of jellium CNT, the axial component of the wave function is a plane wave for infinite tube length:

$$\psi(r,\varphi,z) = \psi_{2D}(r,\varphi) \cdot e^{ik_z z} \tag{5.7}$$

Thus the energy of the axial motion can be separated from the total energy:

$$E(m,k_z) = E_{2D}(m) + E_{axial}(k_z) \tag{5.8}$$

where E_{2D} is the cross sectional component of the energy, i.e. that corresponding to the $\psi_{2D}(r,\varphi)$ wave function component. For the case of the free standing infinite CNT it is enough to consider only the cross sectional component of the wave function and the energy, i.e. $\psi_{2D}(r,\varphi)$ and E_{2D}.

Solving the Schrödinger equation for the real cylindrical geometry eliminates the widely used zone folding approximation [4]. Deviation from zone folding results is of particular importance in the case of small diameter tubes [131, 135].

$R_{n,m}(r)$, the radial solution can be written as a combination of first and second order Bessel and associated Bessel functions, n is the radial quantum number. For our range of parameters there is only one radial solution for each m, hence we omit the radial quantum number. The azimuthal solution is quantized due to the periodic boundary condition in 2π and is doubly degenerate for $m > 0$:

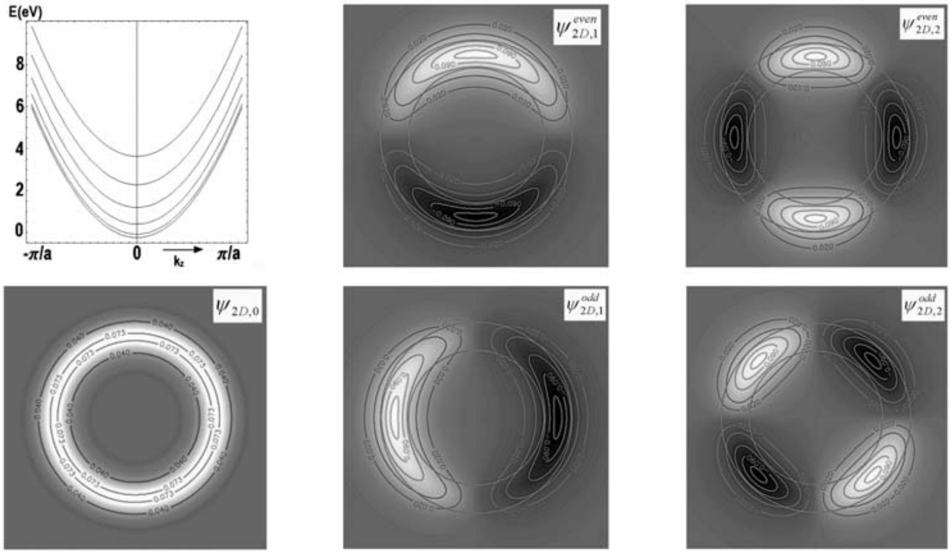

Figure 5.8: Gray scale cross sectional view of stationary wave functions of a jellium tube for different angular momentum quantum eigenstates $m = 0, 1, 2$ respectively. $E_0 = -5.05$ eV, $E_1 = -4.89$ eV, $E_2 = -4.41$ eV. The $m = 0$ ground state is non-degenerated, all the excited states are doubly degenerated. Black corresponds to negative and white to positive wave function values. Upper left subfigure shows the one dimensional band structure of the jellium tube for $m = 0, 1, ...5$. Energy is measured from E_F. From [131].

$$\psi_{2D}(r, \varphi) = R_m(r)\left[C_m \cos m\varphi + S_m \sin m\varphi\right] \tag{5.9}$$

Fig. 5.8 shows the ground state and the first two excited states. The ground-state is non degenerate, while all excited states are doubly degenerate. By choosing the orthonormal states $\cos m\varphi$ and $\sin m\varphi$ one of the states is an even, the other is an odd function of φ (where the $\varphi = 0$ direction points "up" towards the tip apex). The 1D band structure of the jellium CNT is shown on the upper right subfigure of *Fig. 5.8.* All bands are parabolic in this model, i.e. the band structure is similar to that of a doped semiconductor CNT.

5.4 Semi-infinite tube protruding from a step of the support

The right column of *Fig. 5.5* shows the geometry of this system and the time evolution of the $\varrho(\vec{r};t)$ probability density. As can be seen in the snapshot for $t = 2.54$ fs, the first stages of the time development for the infinite tube and for the capped tube above the step are very similar. One can also realize this by comparing the $\varrho(y;t)$ functions displayed in *Fig. 5.6(a)* and *(e)*. This is because for both systems the WP is transmitted first through the tip–NT interface then flows around the tube circumference. After this time, however, the time development of the two systems becomes different because the WP reaches those parts of the model potential different for the two models.

The most important characteristics of the iso-density surfaces shown in *Fig. 5.5* is the effect of the reflection from the tube end. As seen on the snapshot for $t = 6.05$ fs, the right part of the iso-surface (that corresponding to the infinite half of the tube) is similar to the iso-surface for the infinite tube. The left part, however, shows the onset of reflection of the WP from the tube end: there are axial standing wave patterns in the probability density, which are caused by the interference of the electron waves spreading towards and those reflected from the tube end. These probability density waves are also clearly seen in *Fig. 5.6(e)* and *(f)*, the interference maxima are propagating along the tube.

As seen in *Fig. 5.6(c)* and *(g)*, the $j_{support}(y;t)$ linear current densities are also very different for the two cases. The most obvious effect is caused by the partial lack of support for the tube hanging above the step. Because the tube section protruding from the step is hanging at a "height" of 1.335 nm above the lower terrace of the step, the tunneling probability from the tube to the support is much lower than for the case of the flat support where the tube–support distance is only 0.335 nm.

The probability current flowing into the lower terrace (*Fig. 5.6*(g)) is small in magnitude and one can notice a fast oscillation vs. time. This oscillation can be explained as follows. The incoming WP has a finite energy width of $\Delta E = 1.17$ eV. The tunneling effect, however, effectively amplifies [123] the higher momentum components. The fact that the probability current flowing into the lower terrace is originating mainly from this higher energy WP parts is the cause of the higher frequency of the temporal oscillation of the current above the lower terrace than that above the upper terrace. The overall magnitude of the current flowing into the lower terrace is small, as seen on the $T_{support}(y)$ total transmission function of *Fig. 5.6(h)*. This small current, however, becomes visible in *Fig. 5.6(g)* because of the square root gray scale used for the presentation.

Majority of the tunnel current flows into the upper terrace of the step (cf. *Fig. 5.6(h)*). The particular, complicated structure of $j_{support}(y;t)$ seen in *Fig. 5.6(g)* is influenced by: *i)* the propagation of the $\varrho(y;t)$ standing waves (caused by the reflection from the capped end) seen in *Fig. 5.6(e)* along the tube and *ii)* the interference of the angular momentum eigenstates (see Section 5.3) of the tube. The series of ridges seen in $j(y;t)$ are in registry with the maxima of the probability density waves seen in $\varrho(y;t)$.

The $T_i(t)$ transmission functions $(i\epsilon\{tip, support, tubeend\})$ of *Fig. 5.7(b)* are also more complicated than for the reference case, of *Fig. 5.7(a)*. $T_{tubeend}(t)$ is about doubled in magnitude because in the case of the capped tube the WP can leave the tube only at one end as compared to the not capped tube, where it can emerge at both ends. $T_{support}(t)$ is slowly, linearly increasing. This is because the WP, after tunneling from the tip to the tube and "charging" the tube section below the tip (see the $t = 2.54$ fs snapshot of the iso-surface in *Fig. 5.5*) can reach the upper terrace of the step only after longitudinal transport along the tube. Hence, $T_{support}(t)$ is slowly increasing as the WP is moving from the tube section above the lower terrace to that above the upper terrace. (Only this direction of the propagation is possible because of the closed end.) Notice the shoulders negative to each other in the $P_{tube}(t)$ and $T_{tubeend}(t)$ functions. These are because the longitudinal density waves in $\varrho(y;t)$ (*Fig. 5.6(e)*) travelling out from the presentation box cause peaks at the $I_{tubeend}(t)$ current.

The most interesting observation to make, however, when comparing *Fig. 5.7(a)* and *Fig. 5.7(b)* is the identical full curves for the two cases. As I will show in Section 5.6, this constant value corresponds to the total transmission of the system. The (nearly) identical value of the transmissions is further discussed in Section 5.5.

5.5 Quantum dot

By "quantum dot" I mean here a tube closed at both ends, and having no support surface. This hypothetical system makes it possible to investigate the behavior of the tip–tube tunnel junction alone, without the contribution of the tube–support junction, which has a much smaller tunnel resistance.

The time accumulated transmission measured at a plane under the apex of the tip, $T_{tip}(t)$ is shown in *Fig. 5.9* for the three different models. This quantity gives the total WP transmission from the tip apex calculated from $t = 0$ to the given moment. After the launching of the WP there is a thin peak in all the three transmission functions, with a large value of about

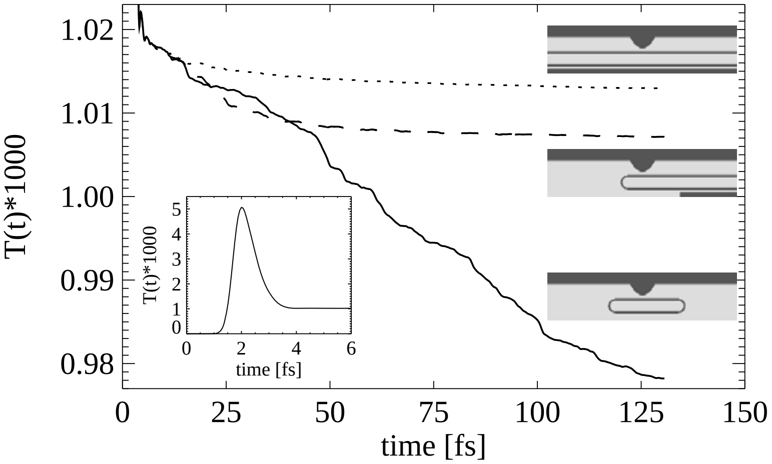

Figure 5.9: Time cumulated transmissions measured below the tip apex. Dotted, dashed, and full lines are for the infinite tube above atomically flat support, for the capped tube hanging above the step, and for the "quantum dot" tube, respectively. The YZ cross sections of the potential for the three model situations are shown by grayscale plots near the curves. The inset shows the initial, large intensity peak (same for all the three models within the line thickness). See the text for details. From [129].

$5 \cdot 10^{-3}$. The inset shows this peak in detail. The meaning of the peak is the WP coming out of the tip apex and then returning there. Plots of the $T_{tip}(t)$ functions for the three models are identical within line thickness for $t < 10$ fs. After this initial peak, the transmission function for the "simple" and "step" situations converges to a constant value which is the fraction of the WP that does not return to the tip. This WP part eventually partly tunnels into the support and partly flows out at the tube end(s), as shown in *Fig. 5.7*.

The $T_{tip}(t = \infty)$ asymptotic values, (cf. Table 5.2) for these two models have a nearly identical value, but as visualized by the enlarged vertical scale applied in *Fig. 5.9*, however, one can notice the small, 0.58% difference, the transmission for the tube above the step is somewhat lower.

This difference can be explained as follows. The magnitude of the tunneling current flowing back from the tube into the tip depends on the probability density of the tube below the tip apex. For the case of the tube hanging above the step, however, there is no (or much less) possibility to tunnel directly from the tube section under the tip into the support surface because of the large tube–support separation. The WP can leave the tube only after a longitudinal transport process. This means that ϱ remains somewhat larger than for the case of the tube above the flat support, which creates a slightly more probability for the electron to go back into the tip.

Note in *Fig. 5.9*, that $T_{tip}(t)$ for the quantum dot model does not converge to a constant value but it is monotonously decreasing. This is caused by the lack of the support surface and the lack of the open tube ends. In this model the WP part "entrapped" on the tube has no other choice than to tunnel back to the tip. It can do this, however, only slowly because the only "exit" is a narrow, tunneling channel. The gradual decrease of the "probability charge" of the QD is seen in the figure by the decreasing transmission function. This function would eventually converge to zero which means that the entire WP returns back to the tip. As seen in the figure, during the 130.6 fs simulation time, however, the transmission decreases only by 4.2 %. Assuming an exponential decay of the "probability charge" of the tube, $T_{tip}(t) = T_0 \, Exp(-t/\tau)$, the fitting for the full line of *Fig. 5.9* gives a value of $\tau = 2817$ fs.

5.6 Detailed analysis of the STM tunneling process

As we can conclude from the results of the preceding Sections, the WP tunneling proceeds according to the following steps.

- The WP first "charges" the NT. This process is composed of two subprocesses:
  - the WP arriving from the tip bulk approaches the tip apex region,
  - majority of the WP is reflected back into the tip bulk but a small part does tunnel into the tube.
- The WP spreads along the NT.
- The WP leaves the tube section in the presentation box through four exits: majority of the WP tunnels into the support surface; part of the WP flows along the tube and then leaves the presentation box through the left and right ends; a small fraction of the WP tunnels back into the tip.

While the WP is spreading along the tube, it is gradually tunneling into the support. From this it follows that if we increased the length of the presentation box, less and less fraction of the WP would flow out from the box at y_{min} and y_{max} (see *Fig. 5.3*). In a real STM experiment the length of the NTs typically exceeds 100 nm. For such a long presentation box, only a negligible fraction of the WP would flow out at the tube ends. This means that in a real experiment (which corresponds to a very long presentation box) those parts of the WP flowing out at the presentation box ends in my calculation would also tunnel into the support surface. Thus

$$P_{support}^{experiment} = P_{support}^{calculation} + nP_{tubeend}^{calculation}, \tag{5.10}$$

where n is the number of the open tube ends, $n = 2$ for the "plain tube" model, $n = 1$ for the "tube hanging above the step" model, $n = 0$ for the "quantum dot" model, and $n = 3$ for the "Y" model.

Moreover after a long enough time, all of the WP would leave the NT. This means that $P_{support}^{experiment} = P_{tip}^{experiment}$ which simply means that the current flowing out from the tip flows into the substrate under stationary conditions.

As I have shown in Section 5.5 the charging and the discharging of the NT occurs in two different time scales. The charging process is much faster, it occurs within 4 fs as seen at the inset of *Fig. 5.9.* The time scale of the discharging process, however, is 100 fs (see *Fig. 5.7*).

During the "charging" process, there is a resonant transfer of electrons from the tip into the tubular jellium, which behaves like a quantum well. The so-called buildup time that this charging process requires is approximately 3 fs. After this time, the transmission $T(t)$ below the tip starts to saturate (see the inset in *Fig. 5.9*). Theory of tunneling through 1D barriers predicts that this saturation should proceed through damped oscillations, with a characteristic frequency proportional to the deviation of the incident energy from the resonance, and a decay time equal to twice the lifetime of the resonant state [136]. The situation is more complex here, due to the 3D geometry of the potential, and because the WP covers a large energy window that encompasses several eigenstates of the jellium tube [131]. The plot of $T(t)$ in the inset of *Fig. 5.9* shows a single oscillation, marked by the peak at about 2 fs. Then it saturates, except for the quantum dot where all the buildup charge slowly returns to the tip.

During the decay of the probability charge of the tube not only the geometry of the tip-support barrier is important (there is no such barrier for the dot), but also the fact that the electrons in the NT have no permanent momentum perpendicular to the barrier. As the animation on the web site shows (`http://www.mfa.kfki.hu/int/nano/online/longspread2004/`), the probability density oscillates around the tube, while spreading along it. The WP tunnels to the support by packets, each time there is an accumulation of charge at the bottom of the tube. The characteristic oscillation period is around 5 fs, as can be inferred from the plots of $j(y;t)$ in *Fig. 5.6*. The characteristic time for the decay of the probability charge on the tube is around 25 fs (plot of P_{tube} in *Fig. 5.7*), much shorter than the decay time for the dot (2817 fs as derived in Section 5.5) because the barrier with the tip is extremely localized in space.

Once the WP is on the tube it can tunnel into the support much easier than back into the tip, hence the magnitude of the tunnel current is mostly determined by the characteristics of the tip–NT tunnel junction. This is somewhat similar to joining two resistances [73] in series, the net resistance $R = R_1 + R_2$ is mainly determined by R_1 if $R_1 >> R_2$.

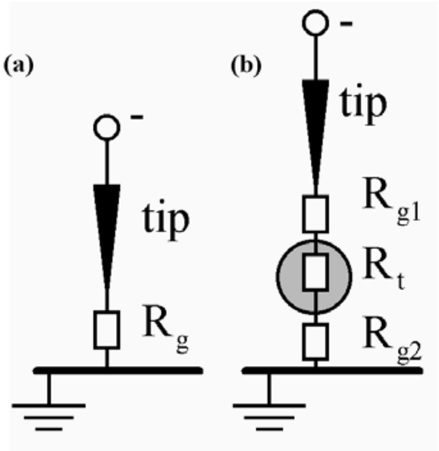

Figure 5.10: Equivalent circuit representation of STM tunneling. (a) Tunneling directly into the support, R_g is the gap resistance. (b) Tunneling through the nanotube, R_{g1} and R_{g2} are the resistances of the two gaps. R is the resistance of the nanotube. From [73].

This is the explanation why the total tunneling probability is nearly the same for the ”plain tube” and for the ”tube hanging above the step” models, although for the first case the tube section directly below the tip is supported but for the second case it is not supported. The details of the WP transport process are different for the two cases, when the tube section below the tip is supported, most of the WP directly tunnels into the support, see *Fig. 5.6(c)*, but when the tube section below the tip is not supported, the WP can tunnel into the support only after a ballistic transport [89], see *Fig. 5.6(g)* — still the total transmission probability is nearly the same for the two cases.

Ballistic conduction was found in conducting AFM experiments [89] in length sections over 5 μm in SWNTs which proves that the electrons preserve phase coherence over such a long length scale. The independence of the total tunneling probability on the presence of the support surface under the tube section below the tip is in fact verified by STM experiments on SWNTs crossing a step on the graphite surface [25], crossing over another NT [137], or hanging over grains of platinum surface [137].

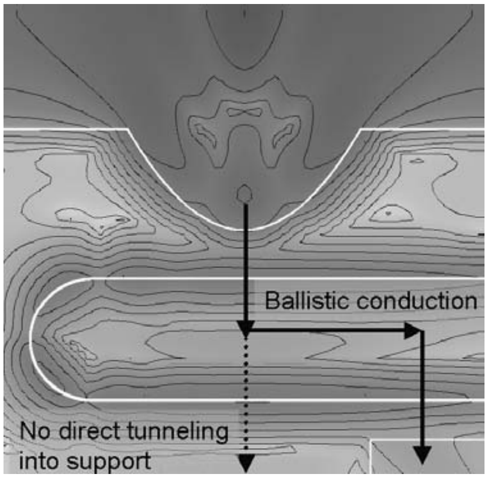

Figure 5.11: STM current flow when the tip is over the SWNT part hanging over the step. Probability density in the plane perpendicular to the support and including the tube axis is shown on a logarithmic gray scale. The thick white lines show the geometrical surface of the tip, nanotube, and support. From [130].

In both experimental situations a section of NT is lifted from the support surface because of its stiffness. According to the topographic STM images and elasticity theory calculations presented in these papers, the SWNT is not supported over a length of 10 - 20 nm.

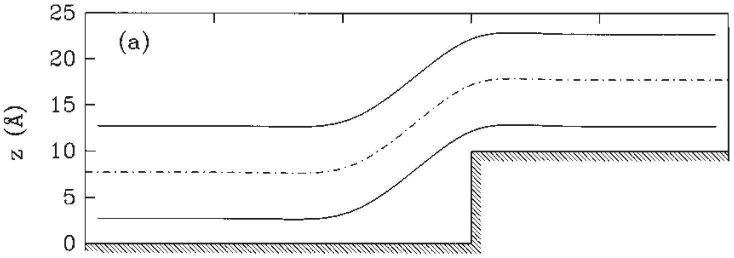

Figure 5.12: Bending of a nanotube crossing an 1 nm step on graphite substrate computed from linear elasticity. The x and z scales differ from each other and, so, the apparent tube diameter varies with the slope of its axis. Ref. [25].

The calculations in [25] indicate that the deformation of the NT is taking place from roughly 20 nm before to 10 nm after the step. After the step edge, there is a slight overshoot of the NT, where it rises above its normal distance from the plateau surface. Though there is no support surface directly below the tube section protruding from the step, still there is no step seen in the topographic line cuts above the edge of the support (see *Fig. 5.13*) which shows that there is no abrupt change in the tunnel current when the tip moves from above the supported NT part to above the unsupported part.

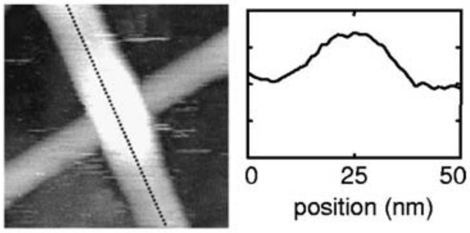

Figure 5.13: Topographic STM image of a crossing of SWNTs. $I_t = 20$ pA, $U_t = -1$ V. The height profile along the dotted line is plotted below the image. The gold substrate is taken as reference height. Ref. [137].

Of course the jellium method does not account for the effect of the different local band structure at different places of the tube and this can cause different tunnel current at different places.

For the capped tube hanging above the step the backscattering [85] of the electron waves from the cap causes axial oscillations in the probability density. Periodic oscillations of the differential conductance along the tube with $\lambda = 2k_F$ periodicity were indeed measured in STS experiments [138] on short SWNTs and calculated by tight-binding [139] and *ab-initio* [140] methods.

For MWNTs the conduction mechanism is different, however. *Fig. 5.14* shows a 3D STM image measured in our Laboratory [130] of a short and thick MWNT being adsorbed on a step edge in such a way that part of the tube is protruding from the step edge. This tube is produced by the arc method, the diameter is 10 nm and the tube protrudes over the lower terrace of the step to 200 nm. This is a similar situation as in our calculation for the capped SWNT but the dimensions are much larger and the tube is a MWNT.

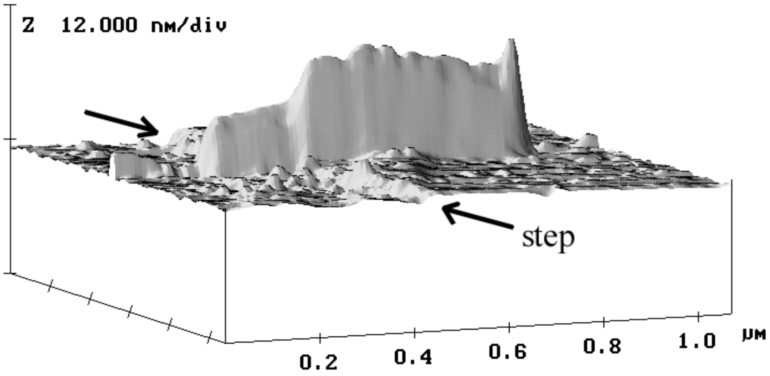

Figure 5.14: Constant current 3D STM image of a MWNT crossing a step on the HOPG surface. Note the transition region at the step edge and the gradual decrease of the apparent height of the tube section above the lower terrace. From [130].

The tube part above the lower terrace is suspended above the HOPG surface at a distance of 1.3 nm. As shown by molecular mechanics calculations [87], such multiwall structures behave like rigid objects. As a consequence, the short tube does not bend to make contact with the substrate on the lower terrace of the step. If bending to contact would occur, one should measure the same height value on the lower terrace as on the upper one which was contrary to the experimental observation, *Fig. 5.14*. The apparent height of the tube part above the higher terrace is constant (some noise is present) because of the translational symmetry along the tube. Right at the step edge there is a transition region in the apparent height, the width of this region corresponds to the length over which the charge spreading takes place along the tube. When the distance of the STM tip as measured from the step edge is larger than the lateral WP spreading length, the electrons can reach the support of the tube only after transport has occured along the tube. The decrease of the apparent height along the tube section above the lower terrace suggests a dependence like ohmic law, $I = U/R$, where R increases with distance from the step [141]. As a consequence, a more pronounced drop is found in the apparent height of the tube than the geometric height of the step in that part where the tube is not supported.

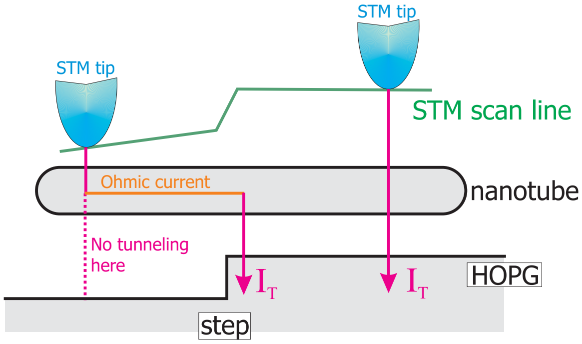

Figure 5.15: (color) Schematic picture of STM current flow when the tip is over the MWNT part over the lower- and the upper terrace of the step. Size proportions are distorted to facilitate presentation. See the text for details.

5.6.1 The tunneling time

The tunneling time (TT) issue is almost as old as quantum mechanics itself [142, 143]. From then it remained almost ignored until the 50-60-th, when the more general problem of defining the quantum collision duration began to be investigated [144, 145, 146]. Development in technology, especially the advent of high speed electronic devices based on tunneling processes revived an interest in the TT analysis. A lot of theoretical studies was performed during the 80's [147, 148].

Measuring the TT on particles is not an easy task, because of the small value of the TT and of the many body effects. This explains why the first measurements of TTs were done on photons [149, 150, 151], utilizing the formal analogy of the Schrödinger and Helmholtz equations. Electronic tunneling times were measured only recently [152, 153].

The TT is the answer to the following question: "How long time did a particle with a given energy spend in the classically forbidden region, as it tunneled through the barrier?" The question is posed after it has become clear that the particle has, indeed, tunneled through rather than been reflected from the barrier. In principle the TT can be easily calculated by following the peak (more precisely the center of mass) of a WP with a narrow spread of energy ΔE in a simulated scattering experiment (see *Fig. 5.16*). At the initial state the WP is well separated from the barrier (*Fig. 5.16*(a)) – its center of mass is a well defined quantity, x_I on the Figure. After the scattering event (*Fig. 5.16*(b)), at the final state (*Fig. 5.16*(c)), the initial WP is split into two WPs, one reflected (back to the region around x_I) and one transmitted, around x_T. These WPs are again well separated from the barrier.

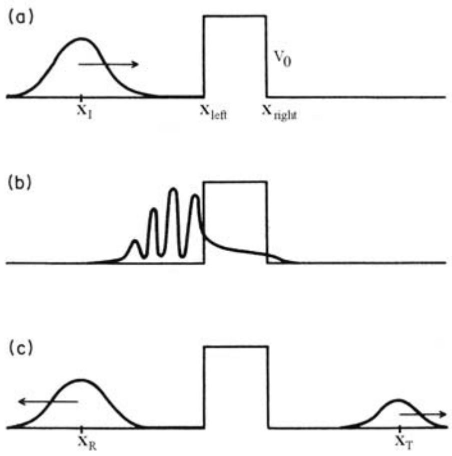

Figure 5.16: Schematic picture of WP scattering on a 1D rectangular potential. Heavy line shows the probability density $\varrho(x)$ and the arrows show the direction of the WP group velocity. After [154]. (a) Initial WP well separated from the barrier. (b) The WP begins to penetrate the barrier, incoming and reflected components cause interferences in the probability density. (c) The final state, reflected and transmitted WPs leave the barrier region.

The $t_T(x_I, x_T, k)$ quantity defined above is called the *asymptotic phase time* [145, 155]. The analytical calculation for the $\Delta E \to 0$ gives:

$$t_T(x_I, x_T, k) = \frac{x_T - x_I}{v_g} + \frac{1}{v_g}\frac{d\alpha}{dk} \tag{5.11}$$

where $v_g = \hbar^{-1}\partial E/\partial k = \hbar k/m$ is the group velocity of the *incoming WP* and $\alpha = \arg T(k)$, the complex phase of the transmission amplitude. The second term in eq. 5.11 shows that the speed of the transmitted WP is slightly shifted with respect to the initial one, $\hbar k/m$. If the barrier $V(x)$ is more transparent for higher energies, the barrier preferably transmits the faster parts of the initial packet, and preferably reflects the slower ones. As a result, the average speed of the transmitted packet is shifted upwards.

Because in the derivation of the asymptotic phase time both the initial and the transmitted WP has to be well separated from the barrier region (in order to prevent interference with the barrier), the asymptotic phase time measures a time interval during most of which the particle did not tunnel. It is possible, however, to substitute formally $x_I = x_{left}$, $x_T = x_{right}$ into eq. 5.11 where x_{left} and x_{right} are the left and right boundaries of the tunnel barrier. This quantity, $t_T(x_{left}, x_{right}, k)$ is called the *extrapolated transmission phase time* [155]. For an *opaque* rectangular barrier of height V_0, i.e. a barrier for which $T \ll 1$,

$$t_T^{extrapolated}(k) = t_T(x_{left}, x_{right}, k) \simeq \frac{2m}{\hbar\kappa k}\,, \tag{5.12}$$

where $\kappa = \sqrt{k_0^2 - k^2}$ and k_0 is derived from $V_0 = \hbar^2 k^2/2m$. As shown in *Fig. 5.17*, $t_T^{extrapolated}$ is large when the energy E of the incoming WP is small (because v_g is small) and also when $E \to V_0$ (because κ is small). For the jellium parameters used throughout this work, $V_0 = 9.81$ eV and $E = E_F = 5$ eV, (see Section 3.2) $t_T^{extrapolated} = 0.13$ fs. It is an important property of the extrapolated transmission phase time that it is independent of the barrier thickness $x_{right} - x_{left}$. This phenomenon, the so called *Hartman effect* has been indeed verified by extensive numerical simulations of 1D WP scattering [156] and evanescent microwave experiments [149].

Apart from the phase time there exists several other TT definitions. We can arrange the majority of the approaches into several groups [157] which are based on

1. time dependent WP development. The phase time discussed above belongs also to this group.
2. Averaging over a set of kinematic paths, distribution of which is supposed to describe the particle motion inside the barrier.
3. Introducing a new degree of freedom, constituting a physical clock for the measurement of the TT.

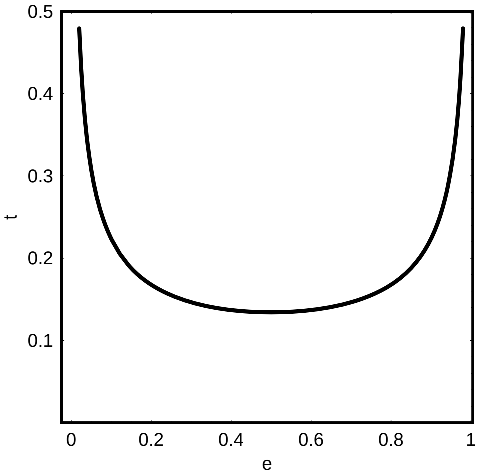

Figure 5.17: Extrapolated transmission phase time (in fs) versus the normalized energy $e = E/V_0$ for $V_0 = 9.81$ eV.

There is no clear consensus about the existence of a simple expression for the TT and the exact nature of that expression. The different formulas proposed give different values, the TT can even be complex [158] in some of the approaches. Less precise questions may, from a practical point of view, have definite answers. If one does not care about numerical factors of order unity, all proposals give values [154] of the same order of magnitude. The *tunneling time scale* is 10^{-15} s for electrons and 10^{-9} s for photons in typical tunneling situations. These values are indeed found in experiments with photons [150] and with electrons [152].

For our WPD calculation those approaches following the WP motion can be applied most consistently and easily. The simple picture behind the asymptotic phase time, however, breaks down for more complicated barriers, because the TT distribution is not any more a narrow function with one peak as in the simple situation shown in *Fig. 5.16.* A typical case is a double barrier, shown in *Fig. 5.18.* This resonant tunneling situation is composed of a fast buildup phase and a slow decay phase. First a quasi localized state is built up in the barrier region. As this state decays, it "emits" a series of reflected and transmitted WPs, shown shematically in *Fig. 5.18.* In the statistical interpretation of the quantum mechanics this means that if we perform the same scattering experiment several times, using the same initial condition, a batch of particles will arrive at time t_1, another batch at time t_2, etc. The 3D situation is even more complicated, because the tunneled-through particles can have different directions.

As seen in *Fig. 5.5* and in *Fig. 5.6*, in the 3D jellium model of the STM tip – NT – support tunnel junction the probability flows from the NT into the support surface in distinct impulses, packets. This is a signature of resonant tunneling.

Figure 5.18: Sketch of a 1D resonant tunneling situation. Probability density is shown by a thick line. The quasi localized state in the double barrier region is decaying in distinct impulses.

Though we can not calculate a precise value for the TT, we can still estimate the TT scale, as explained above. This can be identified with the time scale of the discharging process introduced in Section 5.6. As seen in *Fig. 5.7*, this discharge time scale is $t_{discharge} = 100$ fs. This value is much larger than the 0.13 fs given by eq. 5.12. This 1000 ratio is caused by the resonant tunneling character of the STM tip – NT – support tunnel junction, the TT for a resonant tunneling situation [155] is indeed much longer than that for a non resonant case. For a numerical estimate we can utilize the relation [155] between the dwell time (see Section 3.3.3), the reflection time, and the TT:

$$t_{dwell} = Rt_R + Tt_T \,, \tag{5.13}$$

where R and T are the reflection and transmission probabilities, respectively. We can use the $T \simeq 10^{-3}$ value calculated in Section 5.3, from this $R = 1 - T \simeq 1$. The t_R reflection time can be estimated from the width of the buildup peak in *Fig. 5.9* of Section 5.5: $t_R \simeq 1$ fs. Putting these numbers together we receive a value of $t_{dwell} = 1.1$ fs for the dwell time which has indeed the same order of magnitude as t_{dwell} values calculated in Section 4.1.3.

5.7 Y-junction

In this Section I placed a SWNT Y-junction into the STM model.

SWNT "T" and "Y" junctions were first proposed theoretically [44, 45] (see *Fig. 5.19(a)*). Our group was the first to observe SWNT Y-junctions by STM [14]. The Y shaped NTs were produced by thermal decomposition of fullerene in the presence of transition metals. Techniques for high yield and reproducible production of Y-junctions were developed [159, 15] later.

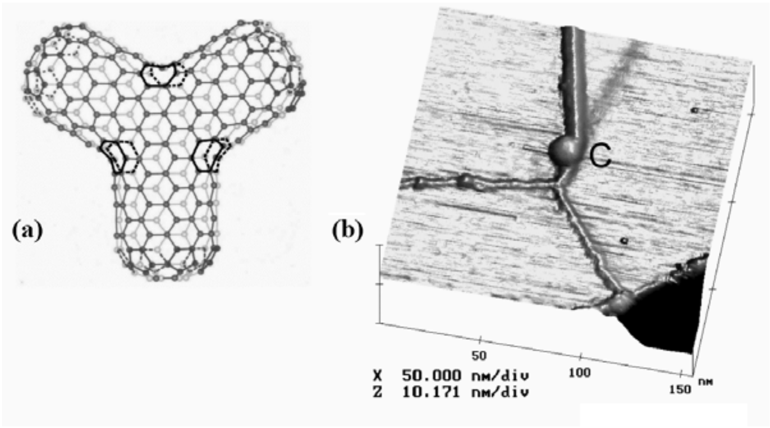

Figure 5.19: SWNT Y-junction. (a) Structural model. Nonhexagonal rings are highlited. Ref. [45] (b) Topographic STM image. Image courtesy of Z. Osváth, MTA MFA, Ref. [160].

To explore the formation of STM image of Y-junctions I placed a jellium model of an SWNT Y-junction [161] into my STM model. The Y-junction is modeled by joining symmetrically three 1 nm diameter semi-infinite cylinders. Two tip positions were analyzed. In *Fig. 5.20(left)* the STM tip is above the center and in *Fig. 5.20(right)* the tip is displaced by 1.2 nm along one of the branches.

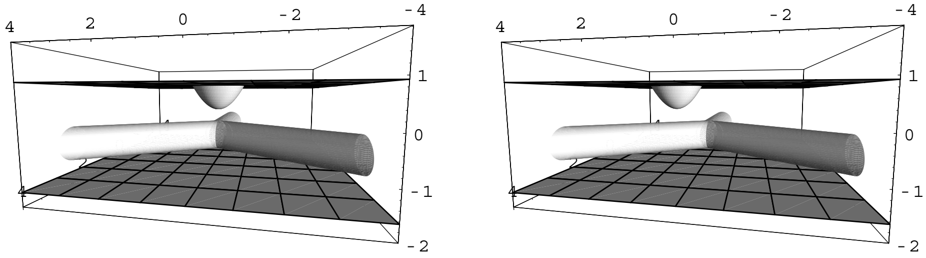

Figure 5.20: Jellium model of SWNT Y-junction in STM configuration. (left) Tip is above the center. (right) Tip is displaced by 1.2 nm. All dimensions are in nm. From [161].

Fig. 5.21 shows the time evolution of the probability density for the symmetric tip position.

- In the panel $t = 0.0$ fs of *Fig. 5.21* the initial WP is shown. The sphere surface is clipped at the upper boundary of the presentation box.

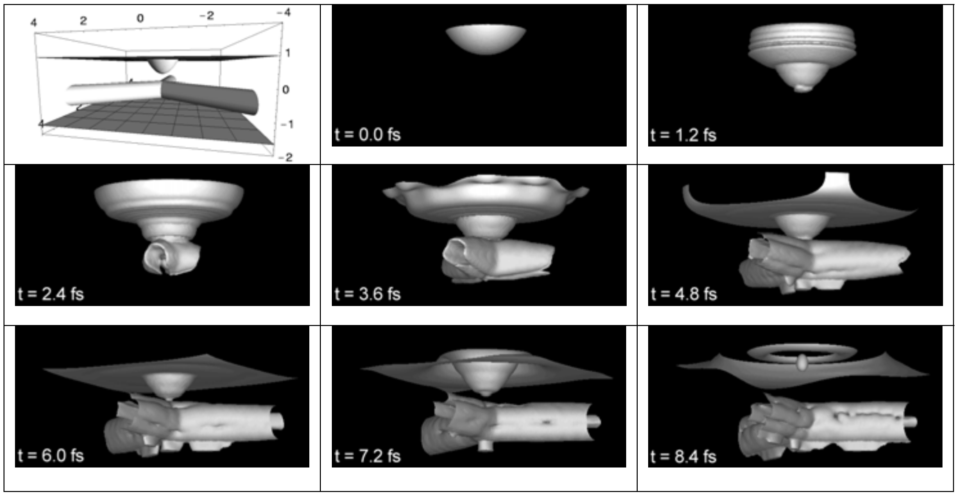

Figure 5.21: Time evolution of the probability density of the wave packet approaching the STM junction from the tip bulk and tunneling through the Y-junction into the support. The upper left image is the model system used in the calculation. The labeled box is the presentation box. All dimensions are in nm. The subsequent images show snapshots of a constant probability density surface. This surface is clipped at the presentation box boundaries. From [161].

- At $t = 1.2$ fs the WP has already penetrated into the tip apex region. The part reflected back into the tip bulk forms interference patterns with the incoming wave. A fraction of the WP just begins to enter into the tip–Y interface.

- At $t = 2.4$ fs the WP flows around the star shaped junction of the three tubes and simultaneously tunnels through it. The incoming and outgoing waves form interference patterns in the tip apex region.

- When the two WP parts (one moving on each sides of the tubes) meet at the lowest point, standing wave patterns begin to form along the circumference of the tubes (at $t = 3.6$ fs).

- Subsequently the WP tunnels through the CNT-support junction and enters into the substrate (at $t = 4.8$ fs). In the meantime the probability density is gradually spreading along the tube axis.

- Note that the shape of the Y-junction – support tunnel channel develops in time along a complex pattern. By around $t = 7.0$ fs most of the

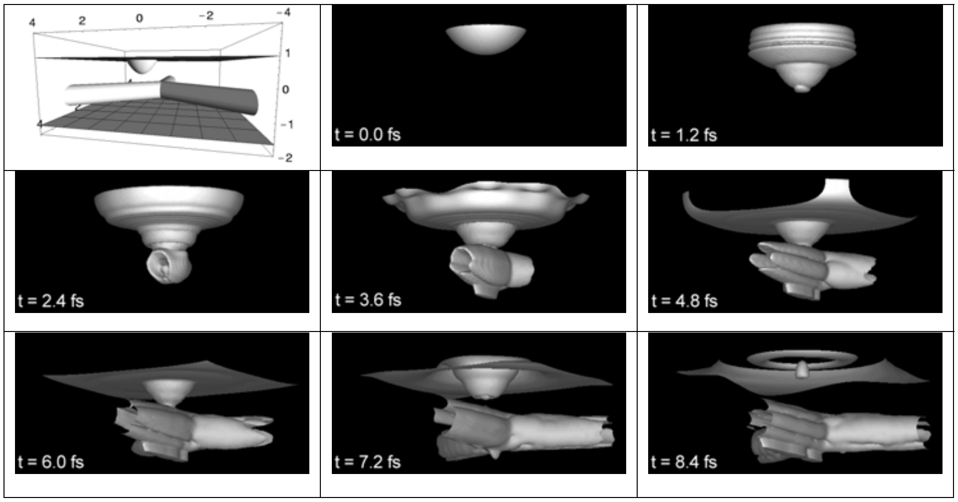

Figure 5.22: Time evolution of the probability density of the wave packet for the case of a tip displaced 1.2 nm from the center along one of the branches. The upper left image is the model system. From [161].

incoming WP is already reflected back into the tip bulk. Hence the structures seen in the tip region at the frames $t = 7.2$ fs and $t = 8.4$ fs show the WP parts tunneling back from the Y-junction to the tip.

In *Fig. 5.22* the tip is displaced from the joining point along one of the branches. Hence the first part of the time development ($t = 0.0$ fs, $t = 1.2$ fs, and $t = 2.4$ fs) shows the same features as for the case of a single CNT (see Section 5.3).

However, when the part of the WP spreading along the tube in the direction of the center reaches the joining point it begins to split along the other two tubes (at $t = 3.6$ fs).

Fig. 5.23 shows a snapshot of the z integrated tube probability density, $\varrho_{tube}(x, y)$ and the probability current density flowing into the support surface, $j_{support}(x, y)$ for a NT Y-junction at $t = 6.71$ fs, where

$$\varrho_{tube}(x, y) = \int \varrho(x, y, z; t = 6.71\,\text{fs})\, \Theta_{tube}(x, y, z)\, dz, \tag{5.14}$$

$$\Theta_{tube}(x, y, z) = \begin{cases} 1, & \text{if } (x, y, z) \text{ is between the tube jellium surfaces;} \\ 0, & \text{otherwise .} \end{cases} \tag{5.15}$$

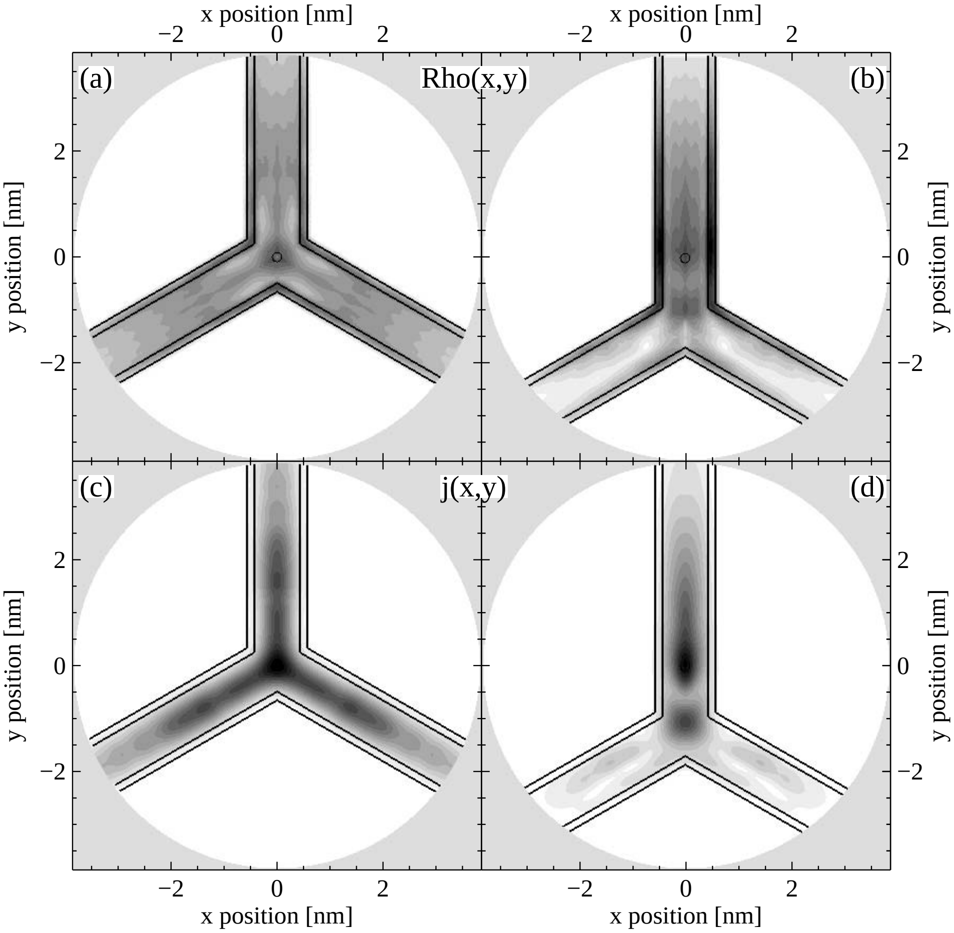

Figure 5.23: Snapshot of the tunneling process through a nanotube Y-junction at $t = 6.71$ fs. (a) and (b) Z integrated tube probability densities for the $d = 0$ nm and $d = 1.2$ nm tip displacements. (c) and (d) Probability current densities flowing into the support surface for the $d = 0$ nm and $d = 1.2$ nm tip displacements. Axial position of the tip is shown by small black circle on each subfigure. Contour shades are drawn on a square root scale. White corresponds to zero and black to maximum density (current), for (a) and (b) [(c) and (d)]. From [129].

The (x, y) projection enhances the probability density in the NT walls, analogous to transmission electron microscopy (TEM) imaging of NTs.

As seen in *Fig. 5.23(a)*, for the symmetric tip position, the three 4 nm long arms (NT sections symmetrically joined at the junction) shown in the presentation window are symmetrically charged. The symmetrical probability charge on the tube causes also a symmetrical tunnel current, as shown in *Fig. 5.23(c)*.

When the tip is displaced by $d = 1.2$ nm along one arm, most of the probability density is accumulated on this arm, cf. *Fig. 5.23(b)*, but still a considerable density is found on the other two arms. The tunnel current (see *Fig. 5.23(d)*), on the other hand, mainly flows into the support surface from the arm below the tip. Note that in both *Fig. 5.23(b)* and *Fig. 5.23(d)* the probability density and the probability current do not decrease monotonically from the point below the tip apex (shown by small circle on the figure) in the direction of the center of the Y-junction but it has oscillations along the arm. These spatial oscillations are caused by interference of the WP spreading from the point below the tip apex in the direction of the junction center and those reflected from the center region.

I have also calculated the time accumulated probability of the WP tunneling out of the tip apex for both the symmetric tip position and for the 1.2 nm tip displacement. As I showed in Section 5.6 based on results of Section 5.5, this quantity gives the total tunneling probability of the whole STM model junction. I found that the tunneling probability for the off-the-junction tip position is the same as for the infinite tube above the flat support (Section 5.3). For the case of the symmetric tip position, the tunneling probability is larger by 14%. This difference in the tunneling probabilities is caused by the different geometries of the tip–tube junction for the above-the-junction and off-the-junction cases. In the off-the-junction case the tip is above an arm, which is a cylinder of 1 nm diameter but in the above-the-junction case the tip is above the trigonal joining point of the three tubes, which is a locally flat surface. The diameter of the tunneling channel is larger when the STM tip is above a flat surface as compared with a curved surface and this explains the enhanced tunneling probability.

As shown in *Fig. 5.23*, however, when the tip is above the arm, displaced 1.2 nm from the junction, the WP penetrates into the junction region and the other two arms with considerable probability. This means that the influence of the local electronic structure of the junction region have to be present in the tunnel current measured above the arm. As shown in *Fig. 5.24*, this conclusion is verified by STS experiments [162] performed in small diameter SWNT Y-junctions, the signature of the junction is still observed in the STS curves when the tip is displaced several nm from the junction.

The same effect is seen in atomic resolution STS maps of semiconductor NT junctions [163]. The two different NTs have different Van Hove singularity positions in the STS curves but according to the experiments and calculations [163] the Van Hove singularity on each side penetrate and decay into the opposite side across the junction over a distance of 2 nm.

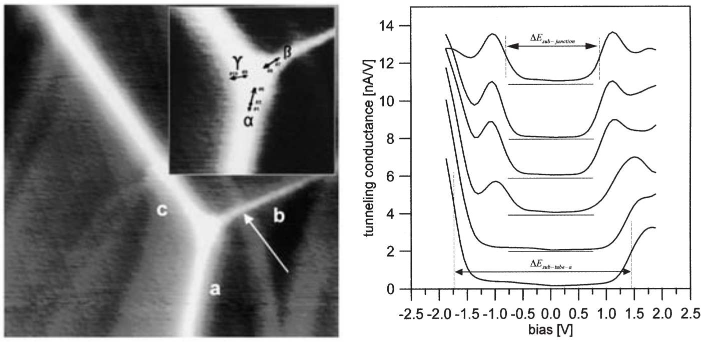

Figure 5.24: *(left)* 230 nm x 230 nm STM image of a carbon nanotube Y-branching. The arrow indicates a crossing of two nanotubes. The direction of STS map measurements are shown in the detail in the inset by arrows. *(right)* dI/dV recorded along the line α as approaching the junction. Ref. [162].

5.8 Summary

Throughout this chapter, I have investigated in detail the tunneling process in the STM model containing carbon nanosystems. WPD calculations were done using a 3D jellium model.

- For a 1 nm diameter NT on an atomically flat support and a 0.4 nm tip-NT separation only 0.1% of the WP is tunneling into the NT. The "probability charge" is first accumulated in the tube section below the tip apex. Next the WP begins to spread along the NT while it is tunneling into the support surface. Interference of the angular momentum eigenstates excited by the incoming WP creates time dependent azimuthal interference patterns to appear in the probability density along the circumference of the tube. Because the tunneling current is determined by the probability density along the lowest fiber of the tube, the time dependence of the azimuthal probability density waves causes oscillations in time of the probability current flowing into the support. These oscillations on the femtosecond scale are probably too fast to be detected electronically but may give measurable effects in a light scattering experiment on the tunnel junction.
- For a hemispherically capped 1 nm diameter SWNT protruding to a length of 3 nm above a 1 nm hight step of the substrate I positioned the STM tip along the tube 1.8 nm "out" from the step edge, i.e. above those part of the NT hanging above the lover terrace of the step. In

this case the WP can not tunnel directly from the tube into the support, it has first to flow axially along the tube until it reaches the step edge. It is found that the total tunneling probability is still the same for this system as for the infinite tube on flat support. From this we can conclude that the WP flows ballistically along the tube. Reflection of the WP from the closed end causes longitudinal probability density wave patterns to appear along the tube. These interference patterns are travelling towards the open end and the distance between two consecutive density maxima is increasing in time (see the snapshots on the right column of *Fig. 5.5*). The cause of this increase is the free electron like dispersion relation along the tube axis: those components of the WP with smaller de Broglie wavelength move with larger velocity (see Appendix B), hence these components leave the presentation window faster.

In case of a similar situation with a 10 nm diameter MWNT protruding to a length of 200 nm above a 1.3 nm high step found experimentally, the situation is different. In this case we found a gradual decrease of the apparent height over the lower terrace which is an indication of ohmic current flow along the tube axis.

- By launching a WP into a NT closed at both ends placed on a non conducting substrate I was able to isolate the effects of the tip – tube interface from the tube – support tunnel junction. It was found that the buildup of the probability charge on the tube is a fast process but the probability charge can decay only slowly through the tip – tube junction hence the overall tunneling probability of a tip – tube – support jellium model system is mostly determined by the characteristics of the tip – tube tunnel junction.

- For a NT Y-junction the tunneling probability is the same as for the straight tube when the tip is displaced 1.2 nm along one arm but it is 14 % higher when the tip is placed above the trigonal symmetry point. In the off-the-junction case the WP, however, still samples the junction region because of its spreading during tunneling.

Chapter 6

Conclusions

6.1 General conclusions

Exploring the applications of carbon nanostructures in a reliable way requires a sample characterization as precise as possible. To that end, very few techniques to characterize an isolated nanostructure at the atomic scale are available. STM is one of the main techniques to investigate carbon nanostructures and devices fabricated from them. It is a unique advantage of this method that STM is able to study both the atomic and electronic structure of the same nanostructure with sub-nanometer resolution.

The interpretation of the STM images of carbon nanostructures involves complications that are normally absent in the study of planar crystalline surfaces. The complications typically appear from a number of quantum effects responsible for distortions in the microscope image of a nano-object.

To analyze these quantum effects in detail I developed a WPD STM simulation software package. With the help of this computer code I studied the geometrical factors responsible for distortions seen in experimental STM images.

By simulating the STM feedback loop I could verify the simple geometric approximation of calculating the apparent broadening of the NT due to the curvature of the tip (tip convolution). This broadening was also shown to depend on the electronic structure of the support. The two wrapping indices of an SWNT can be deduced in principle from the STM image by measuring the diameter and the chiral angle. This kind of characterization, however, is not easy. The STM image is often distorted by the curvature of the lattice, which entails a systematic error in the measurement of the angles. Deriving the diameter from STM information is also challenging, because of the tip convolution effect and of the changes of the tip–tube distance. Today, the most reliable way to evaluate the diameter by an STM consists in measuring the positions of the van Hove singularities in STS measurements and calculating the diameter from the plateau width ΔE_{11}.

Mechanical pressure exerted by the STM tip causes point contacts to develop in the tip–NT and NT–support tunnel junctions. According to my calculations these point contacts cause an asymmetry to appear in the STS spectrum.

Exploring the way the electron tunnels through the STM tip – NTs – support tunnel junction is not an easy task because of the complex geometry of the system. I studied the time dependent probability density and probability current density for several NT configurations in the STM model. These calculations were done using a full 3D jellium model.

I was able to isolate the effects of the tip–tube and tube–support tunnel junctions. It was shown that the overall tunneling probability is mostly determined by the characteristics of the tip–tube tunnel junction. This explains why the support can be neglected in STM image calculations in most of the cases.

Next I examined a tube hanging over a step of the support surface. For a 1 nm diameter tube protruding to 3 nm I calculated the tunneling probability from the tip through the tube into the support for two tip positions: when the tip was above those part over the lower terrace and above those part over the upper terrace. The tunneling probability was the same for the two cases. This was a surprising result for me at first sight because from the intuitive guess one would expect a smaller transmission probability of the whole system when there is no support below the tube into which the WP could tunnel. But this result shows that the conduction is ballistic along the tube (as it must be in the jellium model) and as it is found in experiments on SWNTs. Also it can be understood by considering that the overall transmission is mostly determined by the tip–tube interface. For larger diameter and longer MWNTS, however, we found an ohmic conduction along the tube in our STM measurements.

I also examined the tunneling through a NT Y-junction. The tunneling probability at the symmetric tip position is only slightly increased from its value over an arm but in the off-the-junction case the WP still samples the junction region for an 1.2 nm tip displacement.

These results show the importance of computer simulation in the analysis of experimental STM data.

6.2 Future work

Sphere of applicability of the WPD method in the field of STM image simulations can be greatly increased by removing some of the approximations used throughout this work.

- Material parameters of the tip, NTs, and support was assumed to be identical in my calculations. If we included material parameters into the model, we would handle, e.g. the differences between semiconducting and metallic NTs.
- Capacity of computers makes it possible even today to include the atomic structure into the WPD calculation. This can be done by using a one electron pseudopotential [164] on a fine enough spatial mesh. I published first results of such a calculation in the Kirchberg 2004 conference [165] but more work is necessary to study this model thoroughly.
- The dynamical response of the electron system can be taken into account by using a time dependent potential.
- Larger computers would it make possible to calculate for more complex nanostructures, e.g. for coiled NTs.

Appendix A

The capacitance matrix method

Given a set of electrodes (conducting bodies) $A, B, C, \ldots$ with given electrostatic potential values $U_A, U_B, U_C, \ldots$ or given charges $Q_A, Q_B, Q_C, \ldots$ we would like to calculate the electrostatic potential distribution $U(\vec{r})$ in the vacuum among them. This could easily be done if we knew the charge density distribution $\sigma_X(\eta, \xi)$ on the surface of each of the electrodes $X \epsilon \{A, B, C, \ldots\}$, where η and ξ are the parametric coordinates (inner coordinates) on the surface of the electrodes. Knowing the potentials (or charges) of the electrodes the $\sigma_X(\eta, \xi)$ can be calculated using the capacitance matrix method [97].

The array of the electrostatic potentials $\underline{U} = \{U_A, U_B, U_C, \ldots\}$ is a homogeneous linear function of the array of the charges $\underline{Q} = \{Q_A, Q_B, Q_C, \ldots\}$. Thus we can write $\underline{Q} = \underline{\underline{C}}\,\underline{U}$, i.e. for example for three electrodes (see. *Fig. A.1*):

$$\begin{pmatrix} Q_A \\ Q_B \\ Q_C \end{pmatrix} = \begin{pmatrix} C_{AA} & C_{AB} & C_{AC} \\ C_{BA} & C_{BB} & C_{BC} \\ C_{CA} & C_{CB} & C_{CC} \end{pmatrix} \begin{pmatrix} U_A \\ U_B \\ U_C \end{pmatrix} \tag{A.1}$$

$\underline{\underline{C}}$ is called the capacitance matrix [166].

If we quantize the surface charge distributions $\sigma_X(\eta, \xi)$ using a fine enough mesh (see *Fig. A.1*), the capacitance matrix has to include the partial capacitances for all pairs of the finite elements:

$$\begin{pmatrix} q_{a1} \\ \vdots \\ q_{b1} \\ \vdots \\ q_{c1} \end{pmatrix} = \begin{pmatrix} c_{a1,a1} & \cdots & c_{a1,b1} & \cdots & c_{a1,c1} \\ \vdots & \ddots & \vdots & \ddots & \vdots \\ c_{b1,a1} & \cdots & c_{b1,b1} & \cdots & c_{b1,c1} \\ \vdots & \ddots & \vdots & \ddots & \vdots \\ c_{c1,a1} & \cdots & c_{c1,b1} & \cdots & c_{c1,c1} \end{pmatrix} \begin{pmatrix} u_{a1} \\ \vdots \\ u_{b1} \\ \vdots \\ u_{c1} \end{pmatrix} \tag{A.2}$$

I call $\underline{\underline{c}}$ the partial capacitance matrix.

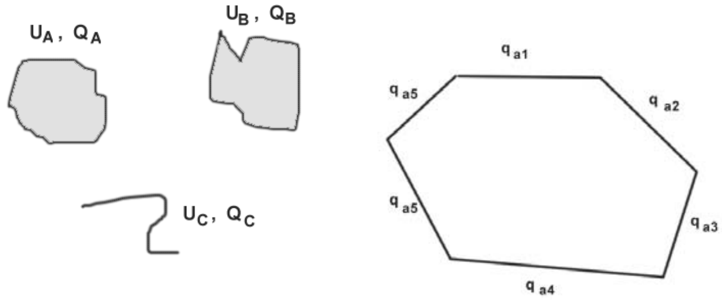

Figure A.1: *(left)* Three electrodes of arbitrary shape and position. *(right)* Finite difference mesh on the surface of an electrode.

Take now the inverse of the partial capacitance matrix $\underline{\underline{d}} = \underline{\underline{c}}^{-1}$:

$$\begin{pmatrix} u_{a1} \\ \vdots \\ u_{b1} \\ \vdots \\ u_{c1} \end{pmatrix} = \begin{pmatrix} d_{a1,a1} & \cdots & d_{a1,b1} & \cdots & d_{a1,c1} \\ \vdots & \ddots & \vdots & \ddots & \vdots \\ d_{b1,a1} & \cdots & d_{b1,b1} & \cdots & d_{b1,c1} \\ \vdots & \ddots & \vdots & \ddots & \vdots \\ d_{c1,a1} & \cdots & d_{c1,b1} & \cdots & d_{c1,c1} \end{pmatrix} \begin{pmatrix} q_{a1} \\ \vdots \\ q_{b1} \\ \vdots \\ q_{c1} \end{pmatrix} \tag{A.3}$$

Elements of the matrix $\underline{\underline{d}}$ can be calculated using the following simple procedure. Put one of the q_j-s to 1 and all other q_i-s to 0, i.e. give one of the finite elements a unit charge and give zero charge to all other finite elements: $q_{ij} = \delta_{ij}$. Now we can calculate the electrostatic potential due to the finite element j at the place of all other finite elements:

$$u_i = U(\vec{r}_i; q_{ij} = \delta_{ij}) = \frac{1}{|\vec{r}_i - \vec{r}_j|} \, . \tag{A.4}$$

From eq. A.3 it follows that the vector $\{u_i\}$ gives column j of $\underline{\underline{d}}$:

$$d_{ij} = \begin{cases} u_i, & i \neq j \\ 0, & i = j \end{cases} \tag{A.5}$$

If we repeat this procedure for all j then we receive all columns of $\underline{\underline{d}}$. Then we can calculate the partial capacitance matrix from $\underline{\underline{c}} = \underline{\underline{d}}^{-1}$.

With the help of the partial capacitance matrix we can determine the charge distribution for any given potential distribution from eq. A.2. If the electrode potentials $U_A, U_B, U_C, \ldots$ are given, then we have to put the potential values for all of the finite elements on that electrode to the given electrode potential:

$$u_{a1} = u_{a2} = \ldots \quad = \quad U_A \tag{A.6}$$

$$u_{b1} = u_{b2} = \ldots \quad = \quad U_B \tag{A.7}$$

$$u_{c1} = u_{c2} = \ldots \quad = \quad U_C \tag{A.8}$$

$$\ldots \tag{A.9}$$

By summing then the charges for all of the finite elements of the given electrode we can determine the charges of the electrodes $Q_A, Q_B, Q_C, \ldots$. From this it follows that the elements of the capacitance matrix $\underline{\underline{C}}$ are given by summing the blocks of the partial capacitance matrix $\underline{\underline{c}}$:

$$C_{XY} = \sum_{i,j} c_{xi,yj} \; , \tag{A.10}$$

i.e. the capacitance between the conducting bodies X and Y is the sum of the partial capacitances $c_{xi,yj}$ between the finite elements i on the surface of X and the finite elements j on the surface of Y for all i and j.

If for one electrode not its potential U_X but its charge Q_X is given (e.g. $Q_X = 0$ for an isolated electrode) then we can determine the corresponding U_X from the system of linear equations A.1 and then determine the potential distribution as described above.

Appendix B

Properties of wave packets

This Appendix gives an overwiev of the most important formulae [167, 101, 168] and properties of wave packets.

A WP represents a quantum system that is localized in its position coordinate. From the Schrödinger equation we obtain equations of motion for the $\langle \vec{r} \rangle$, $\left\langle \vec{k} \right\rangle$ expectation values of the position and momentum.

$$\frac{\partial \langle \vec{r} \rangle}{t} = \left\langle \vec{k} \right\rangle \tag{B.1}$$

$$\frac{\partial \left\langle \vec{k} \right\rangle}{t} = -\langle \nabla V(\vec{r}) \rangle \tag{B.2}$$

Solutions of these equations give the trajectory of the WP. Note that in general

$$\langle \nabla V(\vec{r}) \rangle \neq \nabla_{\langle \vec{r} \rangle} V(\vec{r}) \tag{B.3}$$

i.e. the quantum mechanical trajectory may differ from the classical one for which equality holds in eq. B.3.

The width of the WP in coordinate and momentum space is:

$$\Delta r_i = \sqrt{\langle {r_i}^2 \rangle - \langle r_i \rangle^2} \tag{B.4}$$

$$\Delta k_i = \sqrt{\left\langle {k_i}^2 \right\rangle - \langle k_i \rangle^2} \tag{B.5}$$

where $i \epsilon \{x, y, z\}$. According to the Heisenberg inequality $\Delta r_i \cdot \Delta k_i \geq 1/2$ for all WPs. The equality holds for the Gaussian WP defined as:

$$\psi_{Gauss}(\vec{r}; a, \vec{r}_0, \vec{k}_0) = \left(\frac{2}{\pi a^2} \right)^{\frac{3}{4}} \cdot \exp\left(i \vec{k}_0 \cdot \vec{r} \right) \cdot \exp\left(- \frac{|\vec{r} - \vec{r}_0|^2}{a^2} \right) \tag{B.6}$$

The width of the Gaussian is $\Delta r_i = a/2$. In the general case the width can be different in each direction, i.e. different a_x, a_y, a_z values can be used in eq. B.6.

The momentum space wave function, $\varphi(\vec{k}) = \mathcal{F}[\psi(\vec{r})](\vec{k})$ is also a Gaussian with $\Delta k_i = 1/a$.

In free space $V = 0$ the momentum distribution does not change (see eq. B.2), the momentum wave function is only multiplied by a phase factor:

$$\varphi(\vec{k};t) = \varphi_0(\vec{k}) \exp\left(-i\frac{|\vec{k}|^2}{2}t\right) . \tag{B.7}$$

Hence the coordinate wave function is the convolution of the initial wave function with the free time propagator:

$$\begin{aligned} \psi(\vec{r};t) &= P_{Free}(\vec{r};t) * \psi_0(\vec{r}) && \text{(B.8)} \\ P_{Free}(\vec{r};t) &= \frac{1}{\sqrt{2\pi t}} \exp\left(-i\frac{\pi}{4}\right) \exp\left(i\frac{|\vec{r}|^2}{2t}\right) && \text{(B.9)} \end{aligned}$$

Fig. B.1 shows the time development of the real part of a Gaussian WP in free space. Center of the WP moves with a constant velocity while the packet is spreading along the x axis. Note however, that the spatial distribution of the momentum is also changing during the time development: the function is oscillating more rapidly at the front of the WP and more slowly at the rear. This is because the higher momentum components (those oscillating faster) move with a larger velocity.

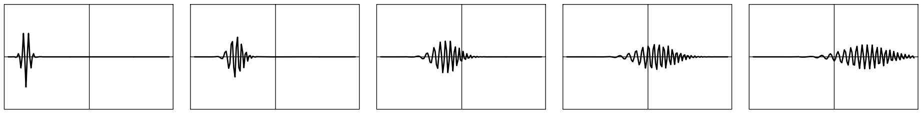

Figure B.1: Time evolution of the real part of a Gaussian wave packet in free space. From [168].

Appendix C

Computational issues

The wave packet dynamical software package I developed contains a direct implementation of the split time FFT method, as described in Section 3.3.1.

The $\psi(\vec{r};t)$ wave function is discretized in space and time. The program first calculates the initial wave function $\psi(\vec{r},t=0)=\psi_0(\vec{r})$ then applies a numerical algorithm representing the time evolution operator (see eq. 3.6) to calculate the ψ for the next time increment:

$$\psi_{n+1}(\vec{r}) = \mathbf{U}_{\delta t}\psi_n(\vec{r}) \tag{C.1}$$

where $\psi_n(\vec{r}) = \psi(\vec{r}, t = n\delta t)$.

The time advance algorithm for a time step δt is composed of three consecutive operations:

1. $\Psi_n^{(1)} = FFT^{-1}\left[P_{kinetic}(\delta t/2)\, FFT\left(\Psi_n\right)\right]$

   where $P_{kinetic}(\delta t/2) = \exp\left(i|\vec{k}|^2\delta t/4\right)$ is the kinetic energy propagator for time $\delta t/2$

2. $\Psi_n^{(2)} = P_{potential}(\delta t)\Psi_n^{(1)}$

   where $P_{potential}(\delta t) = \exp\left(-iV(\vec{r})\delta t\right)$ is the potential energy propagator for time δt

3. $\Psi_{n+1} = FFT^{-1}\left[P_{kinetic}(\delta t/2)\, FFT\left(\Psi_n^{(2)}\right)\right]$

If we are not interested in the value of Ψ_n for every time step then we can combine the 3. operation of step n with the 1. operation of step $n+1$ into a single operation of a kinetic energy propagator for a full time step δt. Since most of the computing time is spent in calculating the FFT-s, this trick decreases the total computing time to nearly half.

The $\psi_n(\vec{r})$ wave function is discretized on a 2D or 3D mesh,

$$\begin{aligned} \Psi^{2D}_{n,(i,j)} &= \psi(i\delta x, j\delta z; n\delta t) && \text{(C.2)} \\ \Psi^{3D}_{n,(i,j,k)} &= \psi(i\delta x, j\delta y, k\delta z; n\delta t) && \text{(C.3)} \end{aligned}$$

$\delta x, y, z$ has to be fine enough to sample the smallest de Broglie wave length found in the WP and also to sample the potential $V(\vec{r})$ with enough detail. For $E_k = E_F = 5$ eV kinetic energy $\lambda_F = 0.55$ nm According to my numerical experiments a spatial grid of 0.03 nm gives a precision of more that 10^{-6} in the current density. For the 3D calculation I increased the grid size to 0.06 nm, which gave a factor of 8 gain in memory and $8 \ln 8$ in time on the price of a factor 10 reduction in the accuracy.

$\delta x, y, z$ and δt can not be chosen independently because the kinetic energy propagator contains a pure imaginary quantity in the exponent and this exponent has to be $< 2\pi$ to prevent unphysical aliasing effects. The largest reciprocal lattice vector $k^{max}_{x,y,z} = 2\pi/\delta x, y, z$, hence the condition for δt is:

$$\delta t < \frac{4}{\pi} \frac{(\delta x, y, z)^2}{D} \tag{C.4}$$

where D is the number of dimension, $D = 2$ or $D = 3$ in this work. According to this requirement a time step of $\delta t^{2D} = 0.2$ au $= 4.8$ as and $\delta t^{3D} = 0.5$ au $= 12.1$ as was applied for the 2D and the 3D case, respectively.

The j probability current densities were calculated by a 5 point finite difference formula. For enough accuracy the ψ wave functions have to be calculated on double precision (16 digits precision).

For the 3D calculation of Chapter 5.3 the size of the calculation box was $11.52 \cdot 23.04 \cdot 11.52$ nm. With the 0.06 nm step size the number of mesh points is $192 \cdot 384 \cdot 192 = 14,155,776$. Using `COMPLEX*16` data type the storage requirement for one wave function is 216 Mbyte.

Most of the computing time is spent by calculating the Fourier transforms. CPU time of the Fast Fourier Transform (FFT) algorithm is scaling with $n \log n$, hence the split operator FFT method can handle large problems. The multidimensional FFT algorithm can be parallelized very efficiently. The ideal computer architecture to calculate FFTs is the shared memory architecture.

The WPD simulation package is written in FORTRAN, because of several reasons. FORTRAN compilers are available for all computer system, these are mostly good optimizing and parallelizing compilers, FORTRAN programs are very well portable, and FORTRAN can handle complex numbers efficiently and easily. Numerical experiments and visualization work were done mainly in the PV-WAVE and Mathematica systems.

Bibliography

[1] G. E. Moore. Cramming more components onto integrated circuits. *Electronics*, 38(8), April 1965.

[2] S. Iijima. Helical microtubules of graphitic carbon. *Nature*, 354:56–58, 1991.

[3] J. Appenzeller, R. Martel, V. Derycke, M. Radosavljević, S. Wind, D. Neumayer, and Ph. Avouris. Carbon nanotubes as potential building blocks for future nanoelectronics. *Microelectron. Eng.*, 64(1):391–397, 2002.

[4] M. S. Dresselhaus, G. Dresselhaus, and P. C. Eklund. *Science of Fullerenes and Carbon Nanostructures.* Academic Press, San Diego, 1996.

[5] S. J. Tans, A. R. M. Verschueren, and C. Dekker. Room-temperature transistor based on a single carbon nanotube. *Nature*, 393:49–52, 1998.

[6] R. V. Seidel, A. P. Graham, J. Kretz, B. Rajasekharan, G. S. Duesberg, M. Liebau, E. Unger, F. Kreupl, and W. Hoenlein. Sub-20 nm short channel carbon nanotube transistors. *Nano Letters*, 5:147–150, 2005.

[7] A. Bachtold, P. Hadley, T. Nakanishi, and C. Dekker. Logic circuits with carbon nanotube transistors. *Science*, 294:1317–1320, 2001.

[8] Ph. Lambin, G. I. Márk, and L. P. Biró. Computation of STM images of carbon nanotubes. *Int. J. Quant. Chem.*, 95:493–503, 2003.

[9] A. Rubio, D. Sánchez-Portal, E. Artacho, P. Ordejón, and J. M. Soler. Electronic states in a finite carbon nanotube: a one-dimensional qauantum box. *Phys. Rev. Lett.*, 82:3520–3523, 1999.

[10] J. W. G. Wildöer, L. C. Venema, A. G. Rinzler, R. E. Smalley, and C. Dekker. Electronic structure of atomically resolved carbon nanotubes. *Nature*, 391:59–62, 1998.

[11] T. W. Odom, J. L. Huang, Ph. Kim, and C. M. Lieber. Atomic structure and electronic properties of single-walled carbon nanotubes. *Nature*, 391:62–64, 1998.

[12] R. Martel, T. Schmidt, H. R. Shea, T. Hertel, and Ph. Avouris. Single- and multi-wall carbon nanotube field-effect transistors. *Appl. Phys. Lett.*, 73:2447–2449, 1998.

[13] A. N. Andriotis, M. Menon, D. Srivastava, and L. Chernozatonskii. Ballistic switching and rectification in single wall carbon nanotube Y junctions. *Appl. Phys. Lett.*, 79(2):266–268, 2001.

[14] P. Nagy, R. Ehlich, L. P. Biró, and J. Gyulai. Y-branching of single walled carbon nanotubes. *Appl. Phys. A.*, 70:481–483, 2000.

[15] B. C. Satishkumar, P. John Thomas, A. Govindaraj, and C. N. R. Rao. Y-junction carbon nanotubes. *Appl. Phys. Lett.*, 77:2530–2532, 2000.

[16] C. Papadopoulos, A. Rakitin, J. Li, A. S. Vedeneev, and J. M. Xu. Electronic transport in Y-junction carbon nanotubes. *Phys. Rev. Lett.*, 85:3476–3479, 2000.

[17] A. N. Andriotis, M. Menon, D. Srivastava, and L. Chernozatonskii. Transport properties of single-wall carbon nanotube Y junctions. *Phys. Rev. B*, 65:165416–1–13, 2002.

[18] V. Meunier, Th. Zacharia, and J.-Ch. Charlier. Intrinsic electron transport properties of carbon nanotube Y-junctions. *Appl. Phys. Lett.*, 81:5234–5236, 2002.

[19] L. P. Biró and Ph. Lambin. Scanning tunneling microscopy of carbon nanotubes. In H. S. Nalwa, editor, *Encyclopedia of Nanoscience and Nanotechnology*, pages 1–12, Fairfield, NJ, 2003. American Scientific Publishers.

[20] G. Binnig, H. Rohrer, Ch. Gerber, and E. Weibel. Tunneling through a controllable vacuum gap. *Appl. Phys. Lett.*, 40(2):178–180, 1982.

[21] G. Binnig, H. Rohrer, Ch. Gerber, and E. Weibel. Surface studies by scanning tunneling microscopy. *Phys. Rev. Lett.*, 49:57–61, 1982.

[22] N. Garcia, C. Ocal, and F. Flores. Model theory for scanning tunneling microscopy: Application to Au(110)(1 2). *Phys. Rev. Lett.*, 50:2002–2005, 1983.

[23] J. Tersoff and D. R. Hamann. Theory of the scanning tunneling microscope. *Phys. Rev. B*, 31:805–813, 1985.

[24] T. W. Odom, J. L. Huang, and C. M. Lieber. STM studies of single-walled carbon nanotubes. *J. Phys.: Condens. Matter*, 14:R145–R167, 2002.

[25] L. P. Biró, S. D. Lazarescu, Ph. Lambin, P. A. Thiry, A. Fonseca, J. B.Nagy, and A. A. Lucas. Scanning tunneling microscope investigation of carbon nanotubes produced by catalytic decomposition of acetylene. *Phys. Rev. B*, 56:12490–12498, 1997.

[26] N. Agrait, J.G. Rodrigo, and S. Vieira. On the transition from tunneling regime to point-contact: Graphite. *Ultramicroscopy*, 42-44:177–183, 1992.

[27] R. M. Feenstra, J. A. Stroscio, , and A. P. Fein. Tunneling spectroscopy of the Si(111)2x1 surface. *Surf. Sci.*, 181:295–306, 1987.

[28] V. Ivanov, J. B.Nagy, Ph. Lambin, A. Lucas, X. B. Zhang, X. F. Zhang, D. Bernaerts, G. Van Tendeloo, S. Amellinckx, and J. Van. Laduyt. The study of carbon nanotubules produced by catalytic method. *Chem. Phys. Lett.*, 233:329–335, 1994.

[29] Ph. Lambin. Electronic transport through nanotubes and nanotube junctions. In Ph. Lambin and V. Popov, editors, *Carbon nanotubes: from basic research to nanotechnology*, volume in press of *NATO ASI Series*, Dordrecht, 2005. Kluwer.

[30] J. Kürti, V. Zólyomi, M. Kertész, and G. Sun. The geometry and the radial breathing mode of carbon nanotubes: beyond the ideal behaviour. *New J. Phys.*, 5:125.1–125.21, 2003.

[31] J. W. Mintmire, B. I. Dunlap, and C. T. White. Are fullerene tubules metallic? *Phys. Rev. Lett.*, 68:631–634, 1992.

[32] J. W. Mintmire and C. T. White. Universal density of states for carbon nanotubes. *Phys. Rev. Lett.*, 81:2506–2509, 1998.

[33] N. Hamada, S. Sawada, and A. Oshiyama. New one-dimensional conductors: graphitic microtubules. *Phys. Rev. Lett.*, 68:1579–1581, 1992.

[34] R. Saito, M. Fujita, G. Dresselhaus, and M. S. Dresselhaus. Electronic structure of graphene tubules based on C_{60}. *Phys. Rev. B*, 46:1804–1811, 1992.

[35] C. L. Kane and E. J. Mele. Size, shape, and low energy electronic structure of carbon nanotubes. *Phys. Rev. Lett.*, 78:1932–1934, 1997.

[36] M. Ouyang, J.-L. Huang, Ch. L. Cheung, and Ch. M. Lieber. Energy gaps in "metallic" single-walled carbon nanotubes. *Science*, 292:702–705, 2001.

[37] T. W. Ebbesen and P. M. Ajayan. Large-scale synthesis of carbon nanotubes. *Nature*, 358:220–222, 1992.

[38] J. C. Charlier and J. P. Michenaud. Energetics of multilayered carbon tubules. *Phys. Rev. Lett.*, 70:1858–1861, 1993.

[39] A. Thess, R. Lee, P. Nikolaev, H. Dai, P. Petit, J. Robert, C. Xu, Y. H. Lee, S. G. Kim, A. G. Rinzler, D. T. Colbert, G. E. Scuseria, D. Tománek, E. Fischer J, and R. E. Smalley. Crystalline ropes of metallic carbon nanotubes. *Science*, 273:483–487, 1996.

[40] J. C. Charlier, T. W. Ebbesen, and Ph. Lambin. Structural and electronic properties of pentagon-heptagon pair defects in carbon nanotubes. *Phys. Rev. B*, 53:11108–11113, 1996.

[41] B. I. Dunlap. Connecting carbon tubules. *Phys. Rev. B*, 46:1933–1936, 1992.

[42] S. Ihara, S. Itoh, and J. Kitakami. Toroidal forms of graphitic carbon. *Phys. Rev. B*, 47:12908–12911, 1993.

[43] S. Ihara, S. Itoh, and J. Kitakami. Helically coiled cage forms of graphitic carbon. *Phys. Rev. B*, 48:5643–5647, 1993.

[44] L. A. Chernozatonskii. Carbon nanotube connectors and planar jungle gyms. *Phys. Lett. A*, 172:173–176, 1992.

[45] G. E. Scuseira. Negative curvature and hyperfullerenes. *Chem. Phys. Lett.*, 195:534–536, 1992.

[46] I. Zsoldos, Gy. Kakuk, J. Janik, and L. Pék. Set of carbon nanotube junctions. *Diam. Rel. Mat.*, 14:763–765, 2005.

[47] H. Terrones, M. Terrones, E. Hernandez, N. Grobert, J. C. Charlier, and P. M. Ajayan. New metallic allotropes of planar and tubular carbon. *Phys. Rev. Lett.*, 84:1716–1719, 2000.

[48] I. László and A. Rassat. Toroidal and spherial fullerene like molecules with only pentagonal and heptagonal faces. *Int. J. Quant. Chem.*, 84:136–139, 2001.

[49] L. P. Biró, S. D. Lazarescu, P. A. Thiry, A. Fonseca, J. B.Nagy, A. A. Lucas, and Ph. Lambin. Scanning tunneling microscopy observation of tightly wound, single-wall coiled carbon nanotubes. *Europhys. Lett.*, 50:494–500, 2000.

[50] L. P. Biró, G. I. Márk, A. A. Koós, J. B.Nagy, and Ph. Lambin. Coiled carbon nanotube structures with supraunitary nonhexagonal to hexagonal ring ratio. *Phys. Rev. B*, 66:165405–1–6, 2002.

[51] Ph. Lambin, G. I. Márk, and L. P. Biró. Structural and electronic properties of coiled and curled carbon nanotubes having a large number of pentagon-heptagon pairs. *Phys. Rev. B*, 67:205413–1–9, 2003.

[52] A. Szabó, A. Fonseca, J. B.Nagy, A. Volodin, C. Van Haesendonck, L. P. Biró, and J. F. Colomer. Synthesis, properties and applications of helical carbon nanotubes. In H. Kuzmany, J. Fink, M. Mehring, and S. Roth, editors, *Electronic Properties of Synthetic Nanostructures*, volume 723 of *AIP Conference Proceedings*, pages 40–44, Melville, New York, 2005. American Institute of Physics.

[53] A. Szabó, A. Fonseca, J. B.Nagy, Ph. Lambin, and L. P. Biró. Structural origin of coiling in coiled carbon nanotubes. *Carbon*, 43:1628–1633, 2005.

[54] J. Chen, M. A. Hamon, H. Hu, Y. Chen, A. M. Rao, P. C. Eklund, and R. C. Haddon. Solution properties of single-walled carbon nanotubes. *Science*, 282:95–98, 1998.

[55] K. T. Lau and D. Hui. Effectiveness of using carbon nanotubes as nanoreinforcements for advanced composite structures. *Carbon*, 40:1605–1606, 2002.

[56] W. Kratschmer, L. D. Lamb, K. Fostiropoulos, and D. R. Huffman. Solid C_{60}: a new form of carbon. *Nature*, 347:354–356, 1990.

[57] L. P. Biró, Z. E. Horváth, L. Szalmás, K. Kertész, F. Wéber, G. Juhász, G. Radnóczi, and J. Gyulai. Continuous carbon nanotube production in underwater ac electric arc. *Chem. Phys. Lett.*, 372:399–402, 2003.

[58] H. W. Zhu, X. S. Li, B. Jiang, C. L. Xu, Y. F. Zhu, D. H. Wu, and X. H. Chen. Formation of carbon nanotubes in water by the electric-arc technique. *Chem. Phys. Lett.*, 366:664–669, 2002.

[59] H. W. Kroto, J. R. Heath, S. C. O'Brien, R. F. Curl, and R. E. Smalley. C_{60}: Buckminsterfullerene. *Nature*, 318:162–163, 1985.

[60] M. José-Yacamán, M. Miki-Yoshida, L. Rendń, and J. G. Santiesteban. Catalytic growth of carbon microtubules with fullerene structure. *Appl. Phys. Lett.*, 62:202–204, 1993.

[61] T. Baird, J. R. Frayer, and B. Grant. Structure of fibruous carbon. *Nature*, 233:329–330, 1971.

[62] H. M. Cheng, F. Li, G. Su, H. Y. Pan, L. L. He, X. Sun X, and M. S. Dresselhaus. Large-scale and low-cost synthesis of single-walled carbon nanotubes by the catalytic pyrolysis of hydrocarbons. *Appl. Phys. Lett.*, 72:3282–3284, 1998.

[63] L. Tapasztó, K. Kertész, Z. Vértesy, Z. E. Horváth, A. A. Koós, Z. Osváth, Zs. Sárközi, Al. Darabont, and L. P. Biró. Diameter and morphology dependence on experimental conditions of carbon nanotube arrays grown by spray pyrolysis. *Carbon*, 43:970–977, 2005.

[64] P. Nikolaev, M. J. Bronikowski, R. K. Bradley, F. Rohmund, D. T. Colbert, K. A. Smith, and R. E. Smalley. Gas-phase catalytic growth of single-walled carbon nanotubes from carbon monoxide. *Chem. Phys. Lett.*, 313:91–97, 1999.

[65] K. A. Dean and B. R. Chalamala. The environmental stability of field emission from single-walled carbon nanotubes. *Appl. Phys. Lett.*, 75:3017–3019, 1999.

[66] S. T. Purcell, P. Vincent, C. Journet, and V. T. Binh. Hot nanotubes: stable heating of individual multiwall carbon nanotubes to 2000k induced by the field-emission current. *Phys. Rev. Lett.*, 88:105502–1–4, 2002.

[67] E. Wong, P. Sheehan, and C. Lieber. Nanobeam mechanics: Elasticity, strength, and toughness of nanorods and nanotubes. *Science*, 277:1971–1975, 1997.

[68] T. Halicioglu. Stress calculations for carbon nanotubes. *Thin Solid Films*, 312:11–14, 1998.

[69] G. Van Lier, C. Van Alsenoy, V. Van Doren, and P. Geerlings. Ab initio study of the elastic properties of single-walled carbon nanotubes and graphene. *Chem. Phys. Lett.*, 326:181–185, 2000.

[70] L. P. Biró and G. I. Márk. STM investigation of carbon nanotubes. In L. P. Biró, C. A. Bernardo, G. G. Tibbetts, and Ph. Lambin, editors, *Carbon filaments and nanotubes: common origins, differing applications?*, volume 372 of *NATO Science Series E*, pages 219–232, Dordrecht, 2001. Kluwer.

[71] M. Ge and K. Sattler. Vapor condensation generation and STM analysis of fullerene tubes. *Science*, 260:515–518, 1993.

[72] C. H. Olk and J. P. Heremans. Scanning tunneling spectroscopy of carbon nanotubes. *J. Mater. Res.*, 9:259–262, 1994.

[73] L. P. Biró, J. Gyulai, Ph. Lambin, J. B.Nagy, S. Lazarescu, G. I. Márk, A. Fonseca, P. R. Surján, Zs. Szekeres, P. A. Thiry, and A. A. Lucas. Scanning tunneling microscopy (STM) imaging of carbon nanotubes. *Carbon*, 36:689–696, 1998.

[74] G. I. Márk, L. P. Biró, J. Gyulai, P. A. Thiry, A. A. Lucas, and Ph. Lambin. Simulation of scanning tunneling spectroscopy of supported carbon nanotubes. *Phys. Rev. B*, 62:2797–2805, 2000.

[75] V. Meunier and Ph. Lambin. Tight-binding computation of the STM image of carbon nanotubes. *Phys. Rev. Lett.*, 81:5588–5591, 1998.

[76] K. Kobayashi and M. Tsukada. Simulation of scanning tunneling microscope image based on electronic states of surface/tip system. *J. Vac. Sci. Technol. A*, 8:170–173, 1990.

[77] R. Haydock, V. Heine, and M. J. Kelly. Electronic structure based on the local atomic environment for tight-binding bands. II. *J. Phys. C Solid St. Phys.*, 8:2591–2605, 1975.

[78] J. Inoue, A. Okada, and Y. Ohta. A block recursion method with complex wave vectors. *J. Phys.: Condens. Matter*, 5:L465–L468, 1995.

[79] G. I. Márk, L. P. Biró, and Ph. Lambin. Modeling and interpretation of STM images of carbon nanotubes. In E. Buzaneva and P. Scharff, editors, *Frontiers in Molecular-Scale Science and Technology of Fullerene, Nanotube, Nanosilicon, Biopolymer (DNA, Protein) Multifunctional Nanosystems*, volume 57 of *NATO Science Series II: Mathematics, Physics and Chemistry*, pages 43–58, Dordrecht, 2001. Kluwer.

[80] J. C. Charlier, J. P. Michenaud, and Ph. Lambin. Tight-binding density of electronic states of pregraphitic carbon. *Phys. Rev. B*, 46:4540–4543, 1992.

[81] D. Tománek and S. G. Louie. First principles calculations of highly asymmetric structure in scanning tunneling microscopy images of graphite. *Phys. Rev. B*, 37:8327–8336, 1988.

[82] L. C. Venema, J. W. G. Wildöer, C. Dekker, A. G. Rinzler, and R. E. Smalley. STM atomic resolution images of single-wall carbon nanotubes. *Appl. Phys. A*, 66:S153–S155, 1998.

[83] C. L. Kane and E. J. Mele. Broken symmetries in scanning tunneling images of carbon nanotubes. *Phys. Rev. B*, 59:R12759–R12762, 1999.

[84] A. Hassanien, M. Tokumoto, Y. Kumazawa, H. Kataura, Y. Maniwa, S. Suzuki, and Y. Achiba. Atomic structure and electronic properties of single-wall carbon nanotubes probed by scanning tunneling microscope at room temperature. *Appl. Phys. Lett.*, 73:3839–3841, 1998.

[85] W. Clauss, D. J. Bergeron, M. Freitag, C. L. Kane, E. J. Mele, and A. T. Johnson. Electron backscattering on single-wall carbon nanotubes observed by scanning tunneling microscopy. *Europhys. Lett.*, 47:601–607, 1999.

[86] B. Shan and K. Cho. Ab initio study of Schottky barriers at metal-nanotube contacts. *Phys. Rev. B*, 70:233405–1–4, 2004.

[87] T. Hertel, R. E. Walkup, and Ph. Avouris. Deformation of carbon nanotubes by surface van der Waals forces. *Phys. Rev. B*, 58:13870–13873, 1998.

[88] L. Orosz and E. Balázs. Calculation of a quasi-self-consistent barrier for metal-vacuum-metal junctions. *Surf. Sci.*, 177:444–450, 1986.

[89] P. J. de Pablo, C. Gómez-Navarro, M. T. Martinez, A. M. Benito, W. K. Maser, J. Colchero, J. Gómez-Herrero, and A. M. Baró. Performing current versus voltage measurements of single-walled carbon nanotubes using scanning force microscopy. *Appl. Phys. Lett.*, 80:1462–1464, 2002.

[90] P. Sautet, J. Dunphy, D. F. Ogletree, and M. Salmeron. The role of electronic interferences in determining the appearence of STM images; application to the S(2x2)/Re(0001) system. *Surf. Sci.*, 295:347–352, 1993.

[91] A. A. Lucas, H. Morawitz, G. R. Henry, J.-P. Vigneron, Ph. Lambin, P. H. Cutler, and T. E. Feuchtwang. Scattering-theoretic approach to elastic one-electron tunneling through localized barriers: Application to scanning tunneling microscopy. *Phys. Rev. B*, 37:10708–10720, 1988.

[92] J. C. Boettger. All-electron full-potential calculation of the electronic band structure, elastic constants, and equation of state for graphite. *Phys. Rev. B*, 55:11202–11211, 1997.

[93] Landolt-Börnstein. *Eigenschaften der Materie in ihren Aggregatzustanden, 6. Teil: Elektrische Eigenschaften I*, page 914. Springer, 1959.

[94] D. Östling, D. Tománek, and A. Rosén. Electronic structure of single-wall, multiwall, and filled carbon nanotubes. *Phys. Rev. B*, 55:13980–13988, 1997.

[95] M. F. Lin and D. S. Chuu. Impurity screening in carbon nanotubes. *Phys. Rev. B*, 56:4996–5002, 1997.

[96] Ch. Girard, M. Devel, X. Bouju, and P.A. Gravil. Computation of electrostatic fields around carbon tubules biased by an STM junction. In C. Joachim and S. Roth, editors, *Atomic and molecular wires*, volume 341 of *NATO Science Series E*, pages 179–192, Dordrecht, 1997. Kluwer.

[97] S. J. Beard and R. W. Hockney. POT4A – a program for the direct solution of poisson's equation in complex geometries. *Comp. Phys. Comm.*, 36:25–57, 1985.

[98] W. H. Southwell. Gradient-index antireflection coatings. *Opt. Lett.*, 8:584–586, 1983.

[99] B. Poirier and Jr. T. Carrington. Semiclassically optimized complex absorbing potentials of polynomial form. I. Pure imaginary case. *J. Chem. Phys.*, 118(1):17–28, 2003.

[100] E. Schroedinger. Quantisierung als Eigenwertproblem (Zweitere Mitteilung). *Ann. Phys.*, 79:489–527, 1926.

[101] B. M. Garraway and K.-A. Suominen. Wave-packet dynamics: new physics and chemistry in femto-time. *Rep. Prog. Phys.*, 58:365–419, 1995.

[102] G. Varga. Computer simulation by the quantum mechanical time-dependent wavepacket method, especially for atom/molecule-solid-surface interaction. *J. Phys: Condens. Matt.*, 14:6081–6107, 2002.

[103] J. Cerdá, M. A. Van Hove, P. Sautet, and M. Salmeron. Efficient method for the simulation of STM images. I. Generalized Green-function formalism. *Phys. Rev. B*, 56:15885–15899, 1997.

[104] A. E. Kaplan, I. Marzoli, W. E. Lamb, and W. P. Schleich. Multimode interference: highly regular pattern formation in quantum wave-packet evolution. *Phys. Rev. A*, 61:32101–1–6, 2000.

[105] J. A. Fleck, J. R. Morris, and M. D. Feit. Time-dependent propagation of high energy laser beams through the atmosphere. *Appl. Phys.*, 10:129–160, 1976.

[106] M. D. Feit, J. A. Fleck, and A. Steiger. Solution of the Schrödinger equation by a spectral method. *J. Comput. Phys.*, 47:412–433, 1982.

[107] G. Iannaccone. General relation between density of states and dwell times in mesoscopic systems. *Phys. Rev. B*, 51:4727–4729, 1995.

[108] M. Büttiker. Larmor precession and the traversal time for tunneling. *Phys. Rev. B*, 27:6178–6188, 1983.

[109] C. R. Leavens and G. C. Aers. Dwell time and phase times for transmission and reflection. *Phys. Rev. B*, 39:1202–1206, 1989.

[110] M. J. Gallagher, D. Chen, B. P. Jacobsen, D. Sarid, L. D. Lamb, F. A. Tinker, J. Jiao, D. R. Huffman, S. Seraphin, and D. Zhou. Characterization of carbon nanotubes by scanning probe microscopy. *Surf. Sci.*, 281:L335–L340, 1993.

[111] M. Ge and K. Sattler. STM of single-shell nanotubes of carbon. *Appl. Phys. Lett.*, 65:2284–2286, 1994.

[112] Z. El Kaakour C. Odin, J. P. Aimé and T. Bouhacina. Tip's finite size effects on atomic force microscopy in the contact mode: simple geometrical considerations for rapid estimation of apex radius and tip angle based on the study of polystyrene latex balls. *Surf. Sci.*, 317:321–340, 1994.

[113] P. Nagy, G. I. Márk, and E. Balázs. Determination of SPM tip shape using polystyrene latex balls. In D. Benoit, H. Werner, J. Wernisch,

L. Van't Dack, and J. F. Bresse, editors, *Microbeam and Nanobeam Analysis*, volume S13 of *Mikrochimica Acta, Suppl.*, pages 425–433, New York, 1996. Springer.

[114] L. C. Venema, V. Meunier, Ph. Lambin, and C. Dekker. Atomic structure of carbon nanotubes from scanning tunneling microscopy. *Phys. Rev. B*, 61:2991–2996, 2000.

[115] Ph. Kim, T. W. Odom, J. Huang, and C. M. Lieber. STM study of single-walled carbon nanotubes. *Carbon*, 38:1741–1744, 2000.

[116] G. I. Márk, L. P. Biró, and J. Gyulai. Simulation of STM images of 3D surfaces and comparison with experimental data: carbon nanotubes. *Phys. Rev. B*, 58:12645–12648, 1998.

[117] G. I. Márk, L. P. Biró, and J. Gyulai. Computer simulation of the STM imaging of nanometric 3D objects on support: carbon nanotubes. In H. Kuzmany, J. Fink, M. Mehring, and S. Roth, editors, *Electronic Properties of Novel Materials – Progress in Molecular Nanostructures*, volume 442 of *AIP Conference Proceedings*, pages 164–167, Woodbury, New York, 1998. American Institute of Physics.

[118] A. Fonseca, K. Hernádi, J. B.Nagy, D. Bernaerts, and A. A. Lucas. Optimization of catalytic production and purification of buckytubes. *J. Mol. Catal.*, 107:159–168, 1996.

[119] K. Hernádi, A. Fonseca, J. B. Nagy, D. Bernaerts, A. Fudala, and A. A. Lucas. Catalytic synthesis of carbon nanotubes using zeolite support. *Zeolites*, 17:416–423, 1996.

[120] A. Bachtold, M. Henny, C. Terrier, C. Strunk, and C. Schönenberger. Contacting carbon-nanotubes selectively with low-ohmic contacts for four-probe electric measurements. *Appl. Phys. Lett.*, 73:274–276, 1998.

[121] Th. Laloyaux, A. A. Lucas, J.-P. Vigneron, Ph. Lambin, and H. Morawitz. Lateral resolution of the scanning tunneling microscope. *J. Microsc.*, 152:53–63, 1988.

[122] Th. Laloyaux, I. Derycke, J.-P. Vigneron, Ph. Lambin, and A. A. Lucas. Simulation of current in the scanning tunneling microscope. *Phys. Rev. B*, 47:7508–7518, 1993.

[123] G. I. Márk. 'Good functions' in tunneling calculations. In D. Mugnai, A. Ranfagni, and L. S. Schulman, editors, *Tunneling and its Implications*, Proceedings of the Adriatico Research Conference, pages 443–444, Singapore, 1997. World Scientific.

[124] D. L. Carroll, P. Redlich, P. M. Ajayan, J. C. Charlier, X. Blase, A. De Vita, and R. Car. Electronic structure and localized states at carbon nanotube tips. *Phys. Rev. Lett.*, 78:2811–2814, 1997.

[125] L. P. Biró, P. A. Thiry, Ph. Lambin, C. Journet, P. Bernier, and A. A. Lucas. Influence of tunneling voltage on the imaging of carbon nanotube rafts by scanning tunneling microscopy. *Appl. Phys. Lett.*, 73:3680–3682, 1998.

[126] H. Mizes, S.-I. Park, and W. A. Harrison. Multiple tip interpretation of anomalous scanning tunneling microscopy images of layered materials. *Phys. Rev. B*, 36:4491–4494, 1987.

[127] L. P. Biró, G. I. Márk, and E. Balázs. STM 'tip changes' – a possible tool for tip characterization. In G. C. Hadjipanayis and R. W. Siegel, editors, *Nanophase materials: synthesis – properties – applications*, volume 260 of *NATO Science Series E*, pages 205–208, Dordrecht, 1994. Kluwer.

[128] J. Tersoff. Contact resistance of carbon nanotubes. *Appl. Phys. Lett.*, 74:2122–2124, 1999.

[129] G. I. Márk, L. P. Biró, and Ph. Lambin. Calculation of axial charge spreading in carbon nanotubes and nanotube Y-junctions during STM measurement. *Phys. Rev. B*, 70:115423–1–11, 2004.

[130] G. I. Márk, A. Koós, Z. Osváth, L.P. Biró, A. M. Benito, W. K. Maser, P. A. Thiry, and Ph. Lambin. Calculation of the charge spreading along a carbon nanotube in STM. *Diamond and Related Materials*, 11:961–964, 2002.

[131] L. Tapasztó, G. I. Márk, J. Gyulai, Ph. Lambin, Z. Kónya, and L. P. Biró. Geometrical effects of wave functions of carbon nanosystems. In H. Kuzmany, J. Fink, M. Mehring, and S. Roth, editors, *Electronic Properties of Novel Materials – Molecular Nanostructures*, volume 685 of *AIP Conference Proceedings*, pages 439–442, Melville, New York, 2003. American Institute of Physics.

[132] L. Tapasztó, G. I. Márk, A. A. Koós, Ph. Lambin, and L. P. Biró. *submitted*, 2005.

[133] F. Grossmann, J.-M. Rost, and W. Schleich. Spacetime structures in simple quantum systems. *J. Phys. A*, 30:277, 1997.

[134] M. J. W. Hall, M. S. Reineker, and W. P. Schleich. Unravelling quantum carpets: a travelling-wave approach. *J. Phys. A*, 32:8275, 1999.

[135] J. Kürti, V. Zólyomi, M. Kertész, G. Sun, R. H. Baughman, and H. Kuzmany. Individualities and average behavior in the physical properties of small diameter single-walled carbon nanotubes. *Carbon*, 42:971–978, 2004.

[136] J. Villavicencio and R. Romo. Dynamical analysis of the buildup process near resonance. *Appl. Phys. Lett.*, 77:379–381, 2000.

[137] J. W. Janssen, S. G. Lemay, L. P. Kouwenhoven, and C. Dekker. Scanning tunneling spectroscopy on crossed carbon nanotubes. *Phys. Rev. B*, 65:115423–1–5, 2002.

[138] L. C. Venema, J. W. G. Wildöer, J. W. Janssen, S. J. Tans, Hinne L. J. Temminck Tuinstra, L. P. Kouwenhoven, and C. Dekker. Imaging electron wave functions of quantized energy levels in carbon nanotubes. *Science*, 283:52–55, 1999.

[139] V. Meunier, P. Senet, and Ph. Lambin. Scanning tunneling spectroscopy signature of finite-size and connected nanotubes: A tight-binding study. *Phys. Rev. B*, 60:7792–7795, 1999.

[140] R. A. Jishi, J. Bragin, and L. Lou. Electronic structure of short and long carbon nanotubes from first principles. *Phys. Rev. B*, 59:9862–9865, 1999.

[141] H. Dai, E. W. Wong, and C. M. Lieber. Probing electrical transport in nanomaterials: conductivity of individual carbon nanotubes. *Science*, 272:523–526, 1996.

[142] E. U. Condon and P. M. Morse. Quantum mechanics of collision processes I. scattering of particles in a definite force field. *Rev. Mod. Phys.*, 3:43–88, 1931.

[143] L. A. MacColl. Note on the transmission and reflection of wave packets by potential barriers. *Phys. Rev.*, 40:621–626, 1932.

[144] D. Bohm. *Quantum theory.* Prentice-Hall, New York, 1952.

[145] E. Wigner. Lower limit for the energy derivative of the scattering phase shift. *Phys. Rev.*, 98:145–147, 1955.

[146] R. Fong. Time delay for wave packets in nonrelativistic scattering theory with inelastic channels present. *Phys. Rev.*, 140:B762–B766, 1965.

[147] E. H. Hauge and A. Støvneng. Tunneling times: a critical review. *Rev. Mod. Phys.*, 61:917–936, 1989.

[148] C. R. Leavens and G. Aers. In R. Behm, N. Garcia, and H. Rohrer, editors, *Scanning tunneling microscopy and related methods*, page 59, Dordrecht, 1990. Kluwer.

[149] A. Enders and G. Nimtz. Evanescent mode propagation and quantum tunneling. *Phys. Rev. E*, 48:632–634, 1992.

[150] A. M. Steinberg, P. G. Kwiat, and R. Y. Chiao. Measurement of the single-photon tunneling time. *Phys. Rev. Lett.*, 71:708–711, 1993.

[151] Ch. Spielmann, R. Szipöcs, A. Stingl, and F. Krausz. Tunneling of optical pulses through photonic band gaps. *Phys. Rev. Lett.*, 73:2308–2311, 1994.

[152] S. K. Sekatskii and V. S. Letokhov. Electron tunneling time measurement by field-emission microscopy. *Phys. Rev. B*, 64:233311–233314, 2001.

[153] D. Dragoman and M. Dragoman. Single-chip device for tunneling time measurements. *J. Appl. Phys.*, 93:6133–6136, 2003.

[154] E. H. Hauge. Can one speak about tunneling times in polite society? In D. Mugnai, A. Ranfagni, and L. S. Schulman, editors, *Tunneling and its Implications*, Proceedings of the Adriatico Research Conference, pages 1–17, Singapore, 1997. World Scientific.

[155] E. H. Hauge, J. P. Falck, and T. A. Fjeldly. Transmission and reflection times for scattering of wave packets off tunneling barriers. *Phys. Rev. B*, 36:4203–4214, 1987.

[156] T. E. Hartman. Tunneling of a wave packet. *J. Appl. Phys.*, 33:3427–3433, 1962.

[157] R. Landauer and Th. Martin. Barrier interaction time in tunneling. *Rev. Mod. Phys.*, 66:217–228, 1994.

[158] Z. S. Wang, L. C. Kwek, C. H. Lai, and C. H. Oh. Quantum tunneling time. *Phys. Rev. A*, 69:052108–052112, 2004.

[159] J. Li, Ch. Papadopoulos, and J. Xu. Nanoelectronics: growing Y-junction carbon nanotubes. *Nature*, 402:253–254, 1999.

[160] Z. Osváth, A. A. Koós, Z. E. Horváth, J. Gyulai, A. M. Benito, M. T. Martinez, W. K. Maser, and L. P. Biró. Arc-grown Y-branched carbon nanotubes observed by scanning tunneling microscopy (STM). *Chem. Phys. Lett.*, 365:338–342, 2002.

[161] G. I. Márk, L. P. Biró, J. Gyulai, Z. Kónya, and Ph. Lambin. Full three-dimensional wave-packet dynamical calculations of STM images of nanotube Y-junctions. In H. Kuzmany, J. Fink, M. Mehring, and S. Roth, editors, *Electronic Properties of Novel Materials – Molecular Nanostructures*, volume 633 of *AIP Conference Proceedings*, pages 381–384, Melville, New York, 2002. American Institute of Physics.

[162] Z. Klusek, S. Datta, P. Byszewski, P. Kowalczyk, and W. Kozlowski. Scanning tunneling microscopy and spectroscopy of Y-junction in carbon nanotubes. *Surf. Sci*, 507:577–581, 2003.

[163] H. Kim, J. Lee, S.-J. Kahng, Y.-W. Son, S. B. Lee, C.-K. Lee, J. Ihm, and Y. Kuk. Direct observation of localized defect states in semiconductor nanotube junctions. *Phys. Rev. Lett.*, 90:216107–1–4, 2003.

[164] A. Mayer. Band structure and transport properties of carbon nanotubes using a local pseudopotential and a transfer-matrix technique. *Carbon*, 42:2057–2066, 2004.

[165] G. I. Márk, L. P. Biró, L. Tapasztó, A. Mayer, and Ph. Lambin. Atomic pseudopotential model for wave packet tunneling through a carbon nanotube. In H. Kuzmany, J. Fink, M. Mehring, and S. Roth, editors, *Electronic Properties of Synthetic Nanostructures*, volume 623 of *AIP Conference Proceedings*, pages 389–392, Melville, New York, 2004. American Institute of Physics.

[166] A. Sommerfeld. *Electrodynamics*, page 70. Academic Press, New York, 1996.

[167] C. Cohen-Tannoudji, B. Diu, and F. Laloë. *Mecanique quantique.* Hermann, Paris, 1973.

[168] G. I. Márk. Analysis of the spreading Gaussian wave packet. *Eur. J. Phys.*, 18:247–250, 1997.